# Design and Fabrication of Nano/Micro Structures with an Integrated Nanomanipulation System

**FOK, Lo Ming**

A Thesis Submitted in Partial Fulfilment
of the Requirements for the Degree of
Doctor of Philosophy
in
Automation and Computer-Aided Engineering

May 2009

UMI Number: 3392250

All rights reserved

INFORMATION TO ALL USERS
The quality of this reproduction is dependent upon the quality of the copy submitted.

In the unlikely event that the author did not send a complete manuscript
and there are missing pages, these will be noted. Also, if material had to be removed,
a note will indicate the deletion.

UMI 3392250
Copyright 2010 by ProQuest LLC.
All rights reserved. This edition of the work is protected against
unauthorized copying under Title 17, United States Code.

ProQuest LLC
789 East Eisenhower Parkway
P.O. Box 1346
Ann Arbor, MI 48106-1346

Thesis/Assessment Committee

Prof. LIU Yunhui (Supervisor)

Prof. LI Wenjung (Co-supervisor)

Prof. WANG Yu, Michael (Chairman)

Prof. LIAO Weihsin (Member)

# Abstract

Nanotechnology has been defined as a description of activities at the atomic level that have applications in the real world. Advances in the field of nanotechnology have expanded the breadth of potential applications tremendously in recent years, which also leads to rapid growth of several research and development areas throughout the world. Recent development in microelectronics, nano-optics and generic chips shows the trend driving towards miniaturization. Gaining access to the nano world also enable us to make further advances in obtaining precise measurement of material properties and exploring fundamental physical laws at the atomic level.

Due to the advances in nanotechnology and its growing of potential applications, it is evident that the development of practical technologies for the manipulation of nanostructures is essential. The focus of this dissertation is to develop an integrated nanomanipulation system that would be able to image, manipulate as well as fabricate micro/nano-scaled structures in a controlled manner. The system consists of four main components: an Atomic Force Microscope (AFM) for obtaining topographic information of sample surfaces, a haptic device controlled by a server which generates the force environment, a molecular dynamics simulation for determinations of the effects of force application on nano particles, and a visualization program for display of the results. An extended platform with high precision and accuracy is included for broadening the workspace. The interface would be implemented for direct interaction with nano molecules. The users are then allowed to see, touch and manipulate such particles. By the principle of contact mechanics, the tip-sample interaction forces and intermolecular forces between the tip and surface can be modeled; calculated forces are used to predict the results of each operation. The proposed nanomanipulation model facilitates further improvement to accommodate other physical phenomena that

characterize the mechanics of nanomanipulation.

The aim for developing such an integrated system is for prototyping of optics components with micro/nano structures, especially for diffractive optics elements (DOE) and optical lightguide. Diffractive optics is a transmissive diffraction grating with a series of closely ruled lines on a piece of transmissive substrate. A collimated beam of monochromatic light incident on a grating will result in the defined light diffraction pattern. The lightguide is being commonly adopted in backlight system, the spatially varying extraction pattern will couple flux out of the light guide to produce a spatially uniform luminance distribution. Determining the ruled lines for diffraction grating and extraction pattern for lightguide is greatly facilitated through the use of optimization. With the imposition of nonlinear constraints, optimization is achieved by incorporating the approximating function into an optimization algorithm. The micro/nano patterns on DOE and optical lightguide are feasible to be fabricated by the integrated nanomanipulation system with the AFM probe tip as a cutting tool. The characteristics of the AFM probe tip are also taken into account when designing the optical elements.

The developed system has been validated by different experiments, including raster scanning, nanoindentation and nanomanipulation testing. New application of nanomanipulation in photonics has been explored. With the proposed nanostructure fabrication techniques, several optical components can be fabricated in a more efficient and cost-effective way.

# 論文摘要

納米科技是用來研究不同結構在原子層面中的活動，在現實世界中已有多方面應用。近年來，納米科技領域的不斷擴展帶來了廣泛的應用潛力，在世界各地引起了若干研究和發展領域的快速增長。而微電子、納米光學及精密芯片的最新發展方向也漸趨微型化。進入納米世界也促使材料特性的測量更準確，同時亦有助於探索原子層面上的基本物理定律。

由於納米技術的進步及不斷增長的實際應用，操控納米結構技術的發展有著顯著的需求。此論文的重點在於研發一套用作納米操控的整合系統，既可作掃瞄影像，亦可操縱或製造微米／納米結構。系統由四個主要部份組成：包括用來檢測樣品表面結構的原子力顯微鏡、由伺服器控制來產生回饋力的操控儀、判定納米粒子反應之分子動力模擬，以及顯示結果之互動環境。為了擴大工作空間，系統亦配合了一套高精度及高準確度的擴展平台。系統界面可提供與納米分子之直接互動。操作員可以檢視、觸摸及操控納米分子。探針與樣品表面之原子相互動力可透過分子動力學來計算，並用作預測實驗的結果。擬議的納米模型亦有助於進一步改善納米操控中的物理特性。

研發此納米操控整合系統的主要目的是在於製作包含微米／納米結構的光學組件，特別是衍射光學元件和導光部件。衍射光學是一種透射式的衍射光柵，於透明的物料上加上一系列的光柵。當準直的單色光束投射到光柵上，便會衍射光預設的光譜排列。而導光部件普遍應用於背光模組上，不同排例陣式的納米結構可用來引導光線並產生均勻的亮度分佈。優化系統對於設計衍射光學的光柵及導光板中微結構之排列有很大的幫助。融合了非線性的約束條件，系統優化便透過逼近函數的優化演算法得以實現。衍射光學元件及導光板上的微米／

納米結構可利用研發出來的整合系統來製造，而原子力顯微鏡的探針便是加工的工具。原子力顯微鏡之探針特性，在設計光學元件時亦同時被考慮。

項目中所研發的系統已透過不同的實驗進行驗證，其中包括光柵掃瞄、納米壓痕及納米刻蝕。同時，亦發掘了此技術於光電範疇上的創新應用。透過擬議的納米結構製造技術，光學元件的製造可以更有效率及更具成本效益。

# Acknowledgement

I especially want to express my sincere gratitude to my supervisor, Professor LIU Yunhui, for his guidance during my research and study at the Chinese University. He was always willing to help us with our research and the research life became rewarding for me.

I was delighted to interact with Professor LI Wenjung by having him as my co-supervisor. His insights to nanotechnology is second to none. Without his guidance and inspiration, this thesis could not be completed successfully.

Professor NING Xi, Professor WANG Yu, and Professor LIAO Weihsin deserve a special thanks as the committee members. Thanks for making their precious comments and suggestions. Their valuable instructions helped me to improve the thesis in many ways.

I further express my gratitude to all schoolmates in the Networked Sensors and Robotics Laboratory for their support in may aspects of my research. I would like to thank the Department of Mechanical and Automation Engineering for providing support.

My deepest appreciation goes for my family for their love and support throughout my life, which enabled me to overcome the frustrations. I would like to share my joy and happiness with them. This thesis is dedicated to all of them.

# Table of Contents


**Abstract** i
**Acknowledgment** v
**Table of Contents** vi
**List of Figures** viii
**1 Introduction** 1
1.1 State of Art in Nanomanipulation 1
1.2 Motivations and Objectives 3
1.3 Contribution of the Thesis 4
1.4 Thesis Outline 7
**2 Atomic Force Microscopy** 9
2.1 Atomic Force Microscope 9
2.2 AFM Imaging Techniques 11
2.3 AFM Operating Modes 14
2.3.1 Continuous Contact Mode 14
2.3.2 Tapping Mode 16
2.4 Artifacts in Raster Scanning 19
2.5 AFM Probe Tip 20
**3 An Integrated Nanomanipulation System with Haptic Device** 25
3.1 Introduction 25
3.2 Design of Haptic Device 27
3.2.1 Belt Pulley System 28
3.2.2 Motion Tracking Mechanism 30
3.3 Integration of Manipulation System 33
3.3.1 Vision Control System 34
3.3.2 Coarse Positioning System 36
3.3.3 System Interface 38
3.4 Design of Graphical User Interface 39
**4 Interatomic Force Modeling** 41
4.1 Introduction 41
4.2 Interatomic Force Modeling 41
4.2.1 Hertz Model 42
4.2.2 Work of Adhesion 45
4.2.3 Deriagain, Muller, Toropy (DMT) Model 46
4.2.4 Johnson, Kendall and Roberts (JKR) Theory 47
4.2.5 Maugis Mechanics 47
4.3 Lennard-Jones Potential 48
4.4 Comparison of DMT, JKR and Maugis Models 49
**5 Validation of the Nanomanipulation System** 51
5.1 Raster Scanning 51
5.2 Nanoindentation 53
5.3 Nanomanipulation 56
**6 Nano-mechanical Test of Nanowires** 58
6.1 Introduction 58
6.2 Calculation of Tip-Sample Adhesion 60
6.2.1 Spring Constant in z-direction 61
6.2.2 Spring Constant in x-direction 63
6.3 Bending Experiment 65

6.3.1 Fabrication of CNT-embedded Structures 65
6.3.2 AFM Bending 67
6.3.3 Discussion on Experimental Results\ 71
**7 Application of AFM Nanomanipulation in Photonics 75**
7.1 Introduction 75
7.2 AFM Techniques and Cutting Tool Selection 78
7.3 Principle of CAE Optical Design 79
7.3.1 Design Optimization 80
7.3.1.1 Model Parameterization 80
7.3.1.2 Merit Function 81
7.3.1.3 Constraints 83
7.3.1.4 Optimization Algorithm 84
7.3.2 Design Modeling 85
**8 Diffractive Optics Elements 89**
8.1 Introduction 89
8.2 Design Considerations 91
8.2.1 Grating Efficiency 91
8.2.2 Stray Light Characteristics 92
8.3 Optical Design of a Beam Splitter 93
8.4 Plano Surface Machining by Single Point Diamond Turning 99
8.5 Results and Discussions 100
**9 An Optical Lightguide for the Backlight Unit 105**
9.1 Basics of a Backlight System 105
9.2 Design Optimization 107
9.3 Results and Discussions 112
**10 Conclusion 115**
10.1 Summary of Research Work 115
10.2 Future Work and Considerations 117
**References 121**
**List of Publications 123**

# List of Figures


| | | |
|---|---|---|
| Fig. 2.1 | Schematic of an Atomic Force Microscope | 9 |
| Fig. 2.2 | A typical force curve | 10 |
| Fig. 2.3 | Damped harmonic oscillator model | 17 |
| Fig. 2.4 | Rectangular cantilever | 21 |
| Fig. 2.5 | V-shaped cantilever | 21 |
| Fig. 2.6 | Vertical deflection at the z-direction | 22 |
| Fig. 2.7 | Section of a bending beam and cross section of a beam | 23 |
| Fig. 3.1 | Design of haptic device | 28 |
| Fig. 3.2 | Internal architecture of the haptic device | 28 |
| Fig. 3.3 | Belt pulley system | 29 |
| Fig. 3.4 | Inner part of a computer mouse | 30 |
| Fig. 3.5 | Motion detection in x and y direction | 30 |
| Fig. 3.6 | Optical encoding dish with slits around the edge | 31 |
| Fig. 3.7 | LED source and infrared sensor | 31 |
| Fig. 3.8 | Schematic drawing of the encoding system | 32 |
| Fig. 3.9 | Working principle of the encoding system | 32 |
| Fig. 3.10 | Atomic Force Microscope | 33 |
| Fig. 3.11 | Optical microscope for image capture | 34 |
| Fig. 3.12 | Real-time image of the tip position | 35 |
| Fig. 3.13 | Motion control system | 37 |
| Fig. 3.14 | Data transfer during manipulation | 38 |
| Fig. 3.15 | User interface under navigation mode | 39 |
| Fig. 3.16 | User interface under manipulation mode | 40 |
| Fig. 4.1 | Two spheres in contact at a point | 42 |
| Fig. 4.2 | Contact between two elastic spheres | 44 |
| Fig. 4.3 | The work of adhesion | 45 |
| Fig. 4.4 | Relationship between contact radius and indentation depth | 50 |
| Fig. 5.1 | Topography of a polymer layer in large scale | 52 |
| Fig. 5.2 | Topography of a polymer layer in small scale | 52 |
| Fig. 5.3 | Section analysis of a polymer surface | 53 |
| Fig. 5.4 | Indentations on a polymer surface | 55 |
| Fig. 5.5 | Section analysis of a polymer surface under nanoindentation | 55 |
| Fig. 5.6 | Array of scratches performed on a polymer thin film | 56 |
| Fig. 5.7 | Cross section analysis of scratches | 56 |
| Fig. 6.1 | Schematic diagram of a cantilever and a sample | 60 |
| Fig. 6.2 | Illustration of a V-shaped cantilever | 60 |
| Fig. 6.3 | Scanning electron microscope (SEM) image showing (a) the top view of CNT-embedded MEMS polymer bridge structure and (b) tilted at 70° | 66 |
| Fig. 6.4 | AFM force-distance curve | 69 |
| Fig. 6.5 | Schematic diagram of the bending test | 70 |
| Fig. 6.6 | Specific regions under the nanoindentation test | 70 |
| Fig. 6.7 | AFM contact force data on bending the CNT-embedded structure with continuous pushing | 71 |
| Fig. 7.1 | Merit function value as a function of iteration number | 82 |
| Fig. 7.2 | Optimization flowchart | 85 |
| Fig. 7.3 | A complex geometrical LED model | 86 |
| Fig. 7.4 | An integrating sphere | 87 |
| Fig. 7.5 | Goniophotometer | 88 |
| Fig. 7.8 | Spatial distribution pattern | 88 |
| Fig. 8.1 | Diffracted light rays through a transmission grating | 90 |
| Fig. 8.2 | Transmission rate measure by a Photospectrometer | 94 |
| Fig. 8.3 | DOE with V-shaped gratings | 94 |
| Fig. 8.4 | Light rays diffracted by the gratings | 95 |
| Fig. 8.5 | Light propagation through optics without gratings | 96 |
| Fig. 8.6 | Light propagation through optics with gratings | 96 |
| Fig. 8.7 | Dimensions of V-shaped grating | 97 |
| Fig. 8.8 | Luminous intensity distribution | 97 |

| | | |
|---|---|---|
| Fig. 8.9 | Illuminous raster chart | 98 |
| Fig. 8.10 | Single Point Diamond Turning Machine | 100 |
| Fig. 8.11 | Surface finish data obtained from Talysurf® measurement | 101 |
| Fig. 8.12 | Scanning data obtained from AFM | 101 |
| Fig. 8.13 | Grating fabrication by AFM nanolithography | 102 |
| Fig. 8.14 | 2D cross-section analysis of a grating | 103 |
| Fig. 8.15 | Laser spot without diffraction grating | 104 |
| Fig. 8.16 | Beam shaping effect by the diffraction grating | 104 |
| Fig. 9.1 | LED backlight unit | 106 |
| Fig. 9.2 | Mesh feedback optimization | 109 |
| Fig. 9.3 | Light scattering pattern | 111 |
| Fig. 9.4 | Luminance distribution after optimization | 112 |
| Fig. 9.5 | V-grooves fabricated by AFM nanolithography | 113 |
| Fig. 9.6 | Topography data obtained from Talysurf® measurement | 113 |
| Fig. 9.7 | Surface finish data obtained from Talysurf® measurement | 114 |
| Fig. 9.8 | Cross-section analysis of a light guide | 114 |
| Fig. 9.9 | Functional prototype with LEDs and light guide | 114 |
| Fig. 10.1 | Lightguide with micro-pyramid structures | 118 |
| Fig. 10.2 | Light distribution for lightguide without microstructures | 119 |
| Fig. 10.3 | Light distribution for lightguide with microstructures | 120 |

# Chapter 1

# Introduction

Over the past decade, the design and utilization of micro-scale devices has continuously increased and becoming an everyday component of modern society. Miniaturization process of mechanical components becomes one of the most prominent research areas all over the world. These micro devices are made up of micro-electro-mechanical system (MEMS), and MEMS technology can often reduce the cost of manufacturing miniature components. Through the reduction of physical size and mass, MEMS technology can also enhance the performance.

However, there are many problems arise through the miniaturization process such as manufacturing limitations and scaling effects. The incapability of various materials and processing technologies of those components require the development of specific system, processes and fabrication methods. The system designed for nanomanipulation must be flexible, automated and accurate since the operator has no direct access to the components and direct handling is not possible. In addition, the system must be repetitive and reliable for providing high quality output.

## 1.1 State of Art in Nanomanipulation

The Scanning Probe Microscope (SPM) provides a direct window into the nanoscale world, and is one of the primary tools that are making possible the current

development of nanotechnology. The first kind of SPM was the Scanning Tunneling Microscope (STM), invented by Binnig and Rohrer at the IBM Laboratory [1]. It provided the ability to image individual atom and small molecule. For example, Eigler's group has used a scanning-tunneling-microscope (STM) – based instrument to arrange single atoms on surfaces into patterns [2], this allowed them to observe the quantum nature of electrons. An STM-based instrument was also implemented to push or move individual molecules by Lyo [3]. The main drawback for STM is the need for conductive samples, which rules out many of its potential applications.

The next instrument being developed was the Atomic Force Microscope, which was being demonstrated a proven imaging technique that has recently gained attention in nano research. The AFM is a system which is designed for investigation of roughness, particle size, or nano-scale surface features [4] – [5]. It can also be used for mechanical characterization of thin film systems using the indentation tests. The AFM can profile sample in three-dimensional space with vertical resolution down to 0.1 nm. As the scanning does not rely on the pressure of tunneling current, a wide range of materials can be used for investigation including semiconductors and non-conducting surfaces. Studies in this research area are continuing grow up. Schaefer and Requicha used a modified AFM to push nanometer-sized particles over surfaces [6] – [8]. A nano-robotic system developed Ning's group can manipulate the nano-particles and

carbon nanotubes in a teleoperated mode. [9]. Lieber's team used the AFM to test nanobeam mechanics by bending them and to characterize the sliding of molybdenum oxide nanocrystals on single-crystal molybdenum disulfide surfaces [10].

In comparison, STM is having a better sensitivity than AFM since it operates in the region where the tunneling current varies exponentially with small tip-sample separation distance instead of the cantilever stiffness. The main difficulty is that only electrically conductive materials can be used for STM manipulation but AFM can deal with any kind of materials. In addition, STM manipulation needs to be conducted in vacuum in order to avoid solid surface changes due to adsorption and desorption of atoms and molecules. The unwanted impurities on the surface will pose as barriers to the manipulation via dragging method. Another potential problem is surface in-homogeneity, which causes variations of electrical conductivity in different regions. Hence, the attractive strength between the tip and sample will be affected. On the other hand, AFM can function in both ambient and vacuum environments.

## 1.2 Motivations and Objectives

The previously mentioned nanomanipulation projects prove the vision and concept but can be improved upon in their fabrication, design and cost. Due the limitations in their construction, it is not possible to define a guided direction of motion and constrain compliance along specific directions. In addition, it will be difficult to

automate the manipulation process. Indeed, there are still many research areas in the field of nanomanipulation. The applications are still mainly focusing on MEMS and biological during recent years, novel application in photonics and optics engineering is not yet well developed.

Since the manipulation involves complex interactions between the probe tip and sample, modeling of the nanomanipulation is crucial in understanding the physics behind the process. The existing force models usually impose a very restrictive condition to the process.

The main objective of this research is to develop a reliable tele-operated nanomanipulation system for efficient fabrication of miniaturized components. Since the accuracy requirements of the operations are demanding, precision of the system must be designed in micro/nanometer range for automated assembly of nanostructures. In order to perform the nanomanipulation in a controlled manner, the force modeling is also important. Different force models will be studied and evaluated so as to identify the most suitable one for simulation and calculation of the contact forces. With a reliable nanomanipulation system, it is possible to explore various novel applications of nanomanipulation techniques.

## 1.3 Contribution of the Thesis

This project aimed at developing an integrated nanomanipulation system with tools

for prototyping and research applications. In this thesis, focus will be on techniques in nanomanipulation and nanoindentation, investigating and characterizing nanotubes, as well as design and prototyping of optical components.

At the initial stage, the nanomanipulation system was available commercially. Our research group had previously gained experience in the operation of the AFM for measurement of several mechanical properties. Since AFM was originally designed for measurement purpose, the workspace was constrained in a definite area. By changing the design of the actuation system, a coarse positioning system was being appended so as to enlarge the workspace and make it more realistic for prototyping. Afterward, a vision control system was being developed for semi-auto localization. User may locate the target position at the captured image of the sample surface, and the AFM probe tip would be able to move directly to the target position. In order to enhance the nanomanipulation process, a haptic device with force feedback was being designed. With the aid of a force feedback device, a haptic interface was provided for the users with the sensation of the tip-sample interaction. In addition with the stereoscopic graphical user interface, users were allowed to perform the nanomanipulation in the virtual nanoworld. The graphical user interface was developed from the topography data fed from the AFM, which displayed both the surface topography and the position of the AFM tip on the sample surface. Data

transmission between the AFM, vision control system and force feedback devices was controlled by the system interface. Different signals passed through the system interface and the user input from the force feedback device was being converted into system commands for the AFM controller. At the same time, the topography data obtained from scanning was also sent through the system interface and the force feedback to the user could be calculated accordingly.

Since AFM scanning is time consuming, it was impossible to perform scanning during the manipulation process. Estimation of the applied force and indentation depth became crucial and it would help in facilitating the nanomanipulation process. Several molecular mechanics models were being studied and a throughout comparison between them brought us a comprehensive approach on modeling of the interatomic forces between the tip and sample.

The developed nanomanipulation system was then being evaluated throughout several experiments, including raster scanning, nanoindentation and nanomanipulation. Experimental results demonstrated that the reliability and stability of the system was accepted. It was also utilized for a bending test of a micro structure embedded with carbon nanotubes. The AFM tip was used to apply a nominal force to measure the resulting deflection of the CNT structure. Mechanical properties could then be determined by the deflection of the AFM tip.

The AFM lithography technique was found to be practical for fabricating high quality microstructure optics. Nanostructures could be obtained from direct machining without any tooling fabrication. High precision of alignment was also an advantage for patterning. Its application in photonics was being investigated, especially in the fields of diffractive optics and optical lightguide. Diffractive optics was capable to mange the light by diffraction, it mainly consisted of a series of parallel grooves formed on a substrate. The distance between adjacent grooves and the geometry of the grooves were major considerations for the efficiency of the diffractive optics. The extremely high precision required of a diffraction grating implied that the fabrication method must be controlled intimately. The same principle was also applicable for a lightguide of a backlight system, where uniform spatial luminance was required. The spatially uniform luminance distribution was obtained from a spatially varying micro pattern. Form accuracy of the geometry and precision alignment of microstructures were factors affecting the efficient of the backlight system. Nanomanipulation became a cost-effective manufacturing method for making the functional prototype.

## 1.4 Thesis Outline

In Chapter 2, an overview of AFM imaging techniques will be provided, including imaging techniques and operating modes. Chapter 3 will present the design of the integrated nanomanipulation system with haptic device. Modeling of interatomic

forces will be discussed in Chapter 4 with a comparison among the selected models. Chapter 5 will summarize the results for the validation of the developed nanomanipulation system, including experiments on raster scanning, nanoindentation and nanomanipulation. In Chapter 6, a nano-mechanical test of nanowires will be presented, including the fabrication of the CNT-embedded structures, setup of the bending test and discussions on the experimental results. Chapter 7 will focus on discussion on AFM nanomanipulation in photonics and concepts of optics design. Two examples will be discussed in Chapter 8 and 9, which are a diffractive optics elements utilized for beam shaping and an optical light guide for a backlight unit. Finally, the thesis will end with a conclusion in Chapter 10.

# Chapter 2

# Atomic Force Microscopy

## 2.1 Atomic Force Microscope

The AFM was invented by Binning, Quate and Gerger in 1986 [11]. The AFM can be used to study the structure and physical properties of the sample surface. The nature of AFM imaging, which employs a small probe interacting with the sample, the elastic cantilever can record the attractive and repulsive forces acting between them. During operation, the tip is gently in contact with the material and slowly scanned across the surface. The lateral and vertical movements of the tip or sample are controlled by piezoelectric actuators and a feedback loop that produce voltage differences proportional to the movement.

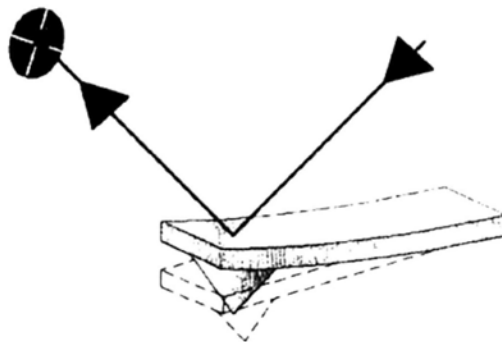

Fig. 2.1 Schematic of an Atomic Force Microscope

The interatomic forces between the atoms on the surface of the material and those on the tip cause the cantilever to deflect. The magnitude of the deflection depends on the separation between the surface atoms and the tip atoms and also the atomic forces between them, such as van der Waals force and adhesion force. The deflection can be recorded by a laser beam focused on the top surface of the cantilever and reflected onto photodetectors. The detection is made so sensitive that the forces being detected can be as small as a few picoNewton. The photodetector signals are used to map the

surface topography of samples with resolutions down to the atomic and nano scales (Fig. 2.1).

In AFM, the photodetector monitors deflections of the cantilever caused by forces acting between the probe tip and surface. A laser beam is focused on the back of the cantilever and measuring the displacement of the reflected beam on a multiple segment photodiode. The corresponding signals are acquired and processed by a feedback electronic. The feedback system is used to control the cantilever deflection and to direct consequently the movements of the piezoelectric actuators. Usually, the sample is mounted onto a piezoelectric translator that moves the sample in the x, y and z directions underneath the probe tip.

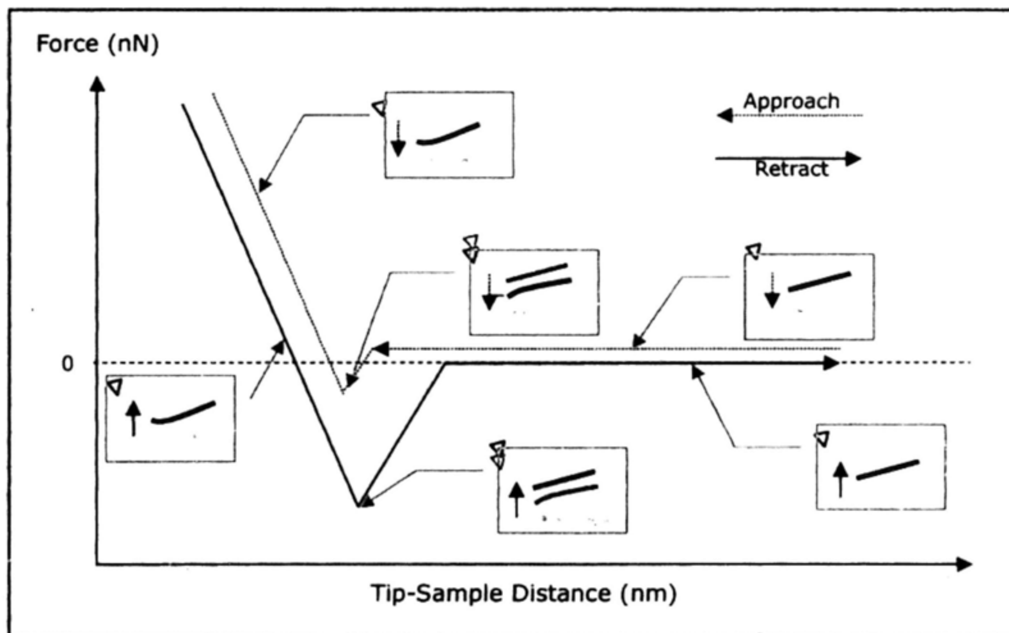


Fig. 2.2 A typical force curve

When the tip translates laterally relative to the sample surface, one measures the sample topography. The forces between the tip and surface deflect the cantilever. The force acting on the cantilever is the product of the cantilever spring constant $k$ and the cantilever deflection $z_c$, which yields the force curve (Fig. 2.2). In the approaching

region, when tip and sample are still far away from each other, the cantilever is at the equilibrium position and the deflection force is zero. On further approach, the cantilever will be deflected by the surface forces. At a certain distance, one can observe an abrupt jump of the tip onto the sample surface that corresponds to the snap-in point in the force curve. This occurs if the gradient of the attractive forces becomes bigger than the sum of the elastic constant and the gradient of the repulsive forces. When the distance is further decreased, the tip is pressed against the sample until the threshold value defined by the user is reached. At this point, the direction of the sample motion is reversed and the tip is withdrawn from the sample. At a certain distance, the tip snap-out from the sample and the cantilever returns to its equilibrium position. The force corresponding to the snap-out is equal to the adhesion force between the tip and sample and the slop of the curve provides in formation on the sample stiffness.

## 2.2 AFM Imaging Techniques

A large number of AFM variants have been developed based on the detection of forces between the probe tip and a sample. A variety of tip-surface interactions can be measured by an AFM, depending on the separation between tip and sample. At a short distance, the tip predominantly experiences interatomic forces: the very short range (~ 0.1 nm) Born repulsive forces and the longer range (up to 10 nm) van der Waals Forces. Further away from the surface, where the van der Waals forces decay rapidly and become negligible (100 – 500 nm above the surface), long-range electric, magnetic and capillary forces are still significantly and can be probed.

At a distance of a few nanometers, van der Waals forces are sufficiently strong to move macroscopic objects, such as AFM cantilevers. Van der Waals forces are usually attractive and rapidly increase as atoms/molecules approach one another. The interactions consist of three components: polarization, induction and dispersion forces. For two identical interacting gas molecules, the van der Waals potential ($U_{vdw}$) can be expressed as the sum of these three components as [13]:

$$U_{vdw} = -\left(\frac{1}{4\pi\varepsilon_0}\right)^2 \left(\frac{\mu}{3kT} + 2\mu^2\alpha + \frac{3}{4}\alpha^2 h\omega\right)\left(\frac{1}{z^6}\right) \approx -\frac{C_1}{z^6} \tag{2.1}$$

where $\varepsilon_0$ is the permittivity of vacuum, $T$ is the temperature, $\mu$ is the permanent dipole moment and $\alpha$ is the polarizability of molecules. $h\omega$ is the ground state energy of electrons, $z$ is the distance between the interacting molecules, and $C_1$ is a constant, known as the London coefficient. Dispersion forces (London forces) generally dominate over orientation and induction forces. Since dispersion forces originate from the instantaneous fluctuations of electrons around the nuclei, they act between all materials.

If the probe further approaches the sample and the electronic wave functions of the outermost probe atoms and sample atoms start to overlap, strong repulsive forces arise. These forces, also called Born repulsive forces, are characterized by having very short range and increasing very sharply as two molecules come together. The repulsive potential is most often expressed as:

$$U_{rep} = \frac{C_2}{z^{12}} \qquad (2.2)$$

The total intermolecular pair potential is obtained by summing the attractive and repulsive potentials. The expression is the well-known Lennard-Jones potential:

$$U = \frac{C_2}{z^{12}} - \frac{C_1}{z^6} \qquad (2.3)$$

where $C_1$ and $C_2$ are the corresponding coefficients for the attractive and repulsive interactions.

Describing the AFM tip and sample interactions, the attractive and repulsive potential pairs have to be summed for all interacting atoms with consideration of the local geometry, material properties, and the non-additive characteristics of the van der Waals interactions. In practice, an experimental force vs. distance curve is applied, that can be registered by the AFM while approaching the tip towards the sample.

The van der Waals potential between two macroscopic bodies, such as a sphere (like the AFM probe tip) and a plane (the sample surface), can be approximated as:

$$U_{vdw} = -\left(\frac{AR}{6z}\right) \qquad (2.4)$$

and the van der Waals force as:

$$F_{vdw} = -\frac{dU_{vdw}}{dz} = -\frac{AR}{6z^2} \qquad (2.5)$$

where $R$ is the radius of the sphere and $A$ is the Hamaker constant ($A \approx \pi^2 C_1 \rho_1 \rho_2$), that characterizes the properties of the interacting materials. $C_1$ is

the London coefficient and $\rho_1$ and $\rho_2$ are the densities of the interacting bodies.

A model concerning repulsive forces between macroscopic objects was formulated by Hertz, the indentation force acting when a sphere is pressed into a flat surface can be given as [14]:

$$F_{ind} = \sqrt{K^2 R d^3} \tag{2.6}$$

where $K$ is the effective elastic modulus ( $\propto$ Young's moduli and Poisson coefficients of the tip and the sample); $d$ is the indentation depth. However, since Hertzian mechanics assumes that there is no adhesion or surface force, it is not the best model for describing a typical AFM experiment [15]. Therefore, there are some alternative continuum mechanical models that include surface forces are being introduced. These models will be further discussed in Chapter 4.

## 2.3 AFM Operating Modes

### 2.3.1 Continuous Contact Mode

The underlying principle of AFM is that the interactions between the sample and the end of the probe tip, which is mounted on a cantilever, result in a response of the cantilever, notably a deflection. In continuous contact mode, also known as repulsive mode, an AFM tip makes soft "physical contact" with the sample. The sharp probe tip, is attached to the end of a V-shaped spring cantilever with a low spring constant, typically between 0.06 N/m and 0.6 N/m. As the scanner gently traces the tip across

the sample, the contact force causes the cantilever to deflect to accommodate changes in topography. In the standard constant force mode, a feedback system maintains the cantilever deflection at a constant level (which corresponds to a constant force according to Hooke's law). The setpoint, which is defined by the user, defines the force that will be exerted on the surface by the tip (which can be as low as 0.1 nN). A common way to measure the cantilever deflection is by utilizing a laser beam which is deflected off the back of the cantilever, into a photodetector. The laser beam which bounces off the cantilever functions as an optical lever arm, amplifying the deflection. As the sample is scanned under the tip, the x, y and z position of the sample surface with respect to the tip is determined by a piezoelectric tube scanner. The movement of the sample in the z-direction, that is need to keep the deflection at its constant setpoint level, is registered during x-y scanning, and a three dimensional map is constructed which is closely related to the topography of the surface.

Contact mode suffers from several drawbacks. The constant downward force of the tip onto the surface is not always low enough to avoid damage. In ambient operation, there is often a lack of force control in the desired range, it is because surfaces are always covered by 10 – 30 mono-layers of adsorbed water vapor, hydrocarbons and / or other contaminants. When the tip comes in close proximity to the surface, the capillary action pulls the tip down towards the surface. This leads to increased normal

and lateral forces when scanning in the continuous contact mode.

## 2.3.2 Tapping Mode

Tapping mode operation successfully overcomes many drawbacks of the contact mode. In tapping mode, to diminish lateral and normal forces exerted by the tip on the sample, the tip is brought only intermittently into contact with the surface during scanning. The basic idea is that the cantilever is brought into oscillation, and changes in oscillation amplitude or phase are detected as the vibrating tip sweeps across and interacts with the surface.

Tapping mode operation can be simulated as a driven, damped harmonic oscillator with an additional term to describe the interaction between the tip and the sample. The motion is expressed in terms of the displacement of the tip $d(t)$, and the position of the root of the cantilever $z(t)$, as depicted in Fig. 2.3. The cantilever is treated as a massless spring of spring constant $k_c$ and eigenfrequency $f_c$ that is loaded by a tip of effective point mass $m$. The equation of motion can be given as [16]:

$$m\ddot{d}(t) = k_c\left(z(t) - d(t)\right) + \frac{m\omega_c}{Q}\left(\dot{z}(t) - \dot{d}(t)\right) + F_{ts}\left(d, \dot{d}\right) \tag{2.7}$$

where $\omega = 2\pi f_c$. The term $F_{ts}\left(d, \dot{d}\right)$ contains the unique physics of the intermittent contact mode and represents the interaction between the tip and the sample $Q$ is the quality factor of the cantilever. ($Q$ is defined as the ratio of the peak height of the root-mean-square amplitude curve at resonance to the peak full-width at half

maximum).

The cantilever is driven through $z(t)$ as:

$$z(t) = z_0 + \delta \cdot \sin(\omega t) \qquad (2.8)$$

where $\delta$ is the drive amplitude and $\omega = 2\pi f$ with the drive frequency $f$. $z_0$ is the mean distance between the base of the cantilever and the sample surface, and it is used to regulate the setpoint amplitude. After short transient, the oscillation of the tip can be expressed as:

$$d(t) = d_0 + \delta_t \cdot \sin(\omega t + \alpha) \qquad (2.9)$$

where $d_0$ is the mean distance between the tip and the sample surface, $\delta_t$ is the amplitude and $\alpha$ is the phase.

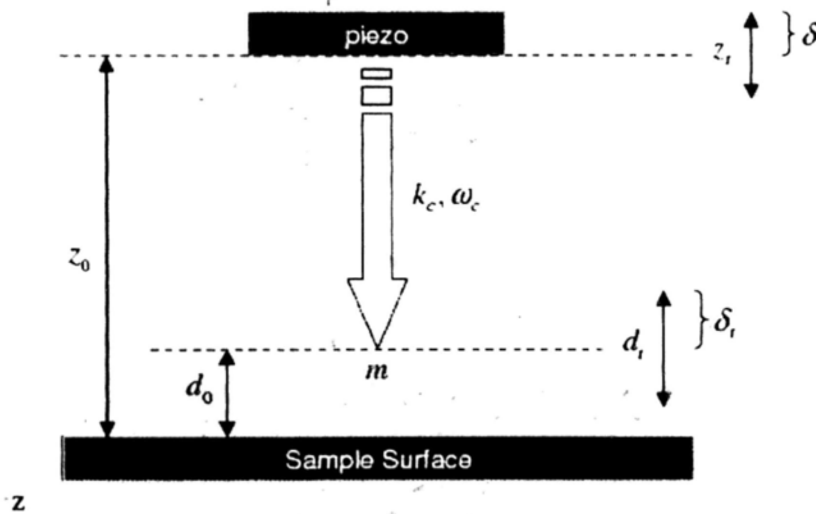


Figure 2.3 Damped harmonic oscillator model

In tapping mode, the tip is mounted on a rigid cantilever ($k_c$ = 20 – 50 N/m) that is oscillated vertically at a relatively high amplitude ($\delta$ = 10 – 100 nm) by using a

piezoelectric actuator. The oscillation frequency is set close to the mechanical resonance frequency of the cantilever ($f_c \approx$ 200 – 400 kHz). Typical operation parameters provide the cantilever enough energy to avoid being trapped by attractive forces. The movement of the tip goes through non-contact ad contact tip-sample conditions and the two regimes are separated by the interatomic distance ($a_0$). For distances larger than $a_0$, the attractive tip-sample interaction ($F_{ts}$) can be calculated through the van der Waals force between a sphere and a flat surface according to Eq. 2.5. At a distance smaller than $a_0$, repulsive forces come into play and the description of $F_{ts}$ in this regime is not that simple and it could be described by several continuum contact mechanical models.

During tapping mode imaging, the vibration characteristics (the frequency, amplitude and phase) of the oscillating tip are measured. In principle, a feedback regulation can be based on the detection of any of these parameters, all of them are sensitive to changes of the tip-sample interactions according to eq. 2.1. While the sample is scanned under the vibrating tip, a feedback loop adjusts the tip-sample separation to maintain a constant cantilever amplitude at a setpoint level determined by the user. A topographical image of the surface is created by recording the feedback signal, which regulates the vertical movements of the sample during scanning, and plotting it as a function of the horizontal position, determined by the $x$ and $y$ positions of the

piezoelectric actuator.

## 2.4 Artifacts in Raster Scanning

AFM techniques is subjected to a number of artifacts that may appear in the images obtained, it is important to keep in mind several concerns in order to obtain accurate data from AFM imaging. The imaging process is always a convolution of the probe geometry and the shape of the features being imaged. Probe selection is important for avoiding artifacts from probe. If the probe is much smaller than the features being imaged, then the artifacts generated by the probe could be minimized and the dimensional measurements derived from the images will be more accurate. The sharpness of probe should also be considered if the probe needs to go into a feature that is below the surface. Otherwise, the size of the feature will appear too small as the probe is unable to reach the bottom of the features. The profile is then established by the geometry of the probe instead of the geometry of the sample.

The piezoelectric actuators made of ceramics are electromechanical transducers, which are capable for motions in very small distances. However, when a linear voltage ramp is applied to piezoelectric ceramics, they will move in a nonlinear motion. Further, the piezoelectric ceramics exhibit hysteretic effects caused by self-heating. Artifacts can also be introduced by the geometry of scanner and the positioning of the scanner relative to the sample. In such way, the AFM must be

calibrated in the X, Y and Z axis in advance. The motion of the scanners must be linear so that the distances measured from the images are accurate. A common method for correcting the problems is to add calibration sensors, which can be used to correct the linearity and the calibration in real-time.

Image processing is required for analyzing the AFM images, there are some common artifacts that are introduced by the image processing error. Usually a low pass filter is used to "smooth" data before it displays, such filter can cause steps in images to appear distorted. On the other hand, matrix filter is also effective at "smoothing" images and removing noise from the image. However, the filtering process often reduces the resolution of the image. One should pay attention when selecting a suitable filter for image processing.

## 2.5 AFM Probe Tip

There are two common shapes of AFM cantilever, one is a beam in the form of a rectangular parallepiped having length $l$, thickness $t$ ($t << l$) and width $w$ ($w << l$) as shown in Fig. 2.4.

Another form is two beams connected at an angle having a tip at its free end, which is the V-shaped cantilever (Fig. 2.5).

When a force acting on a rectangular cantilever, the cantilever tip will deflect along both $x$ and $y$ axes. For normal force $F_z$ is then composed of the longitudinal $F_x$

and transverse $F_y$ lateral forces.

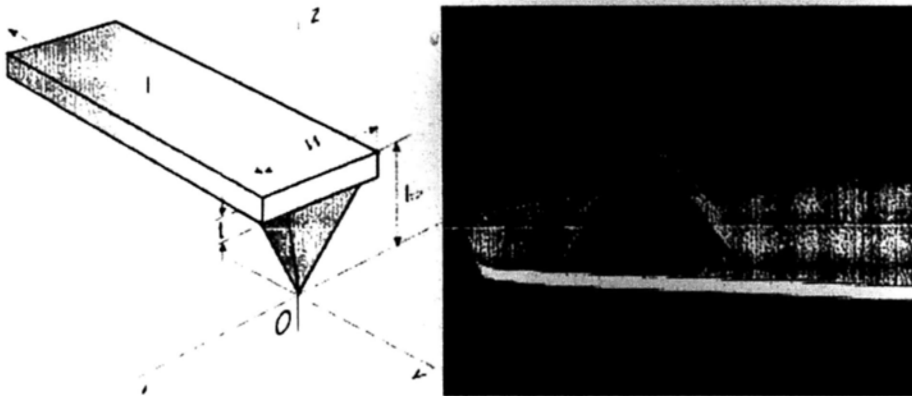

Fig. 2.4 Rectangular cantilever

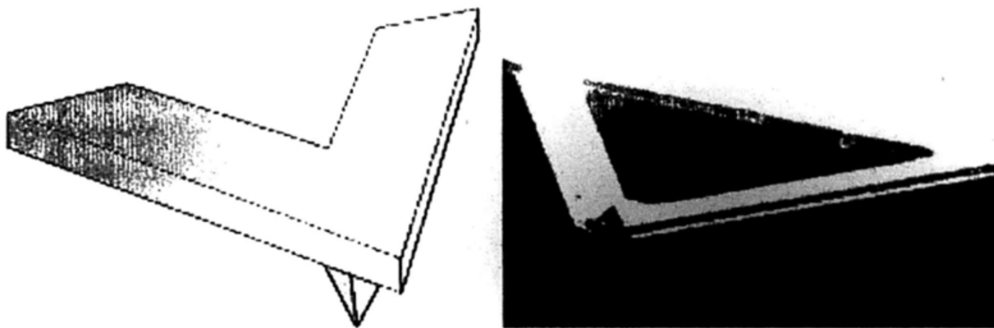

Fig. 2.5 V-shaped cantilever

In order to determine the applied force, one should know the cantilever deformation in various directions. Consider that the tip deflection, $\Delta$ having components of $\Delta_x$, $\Delta_y$, and $\Delta_z$, is linearly dependent to the applied force $F$ according to the Hooke's Law [12]

$$\Delta = C^{-1}F \tag{2.5}$$

where $C$ is the inverse stiffness tensor describing the elastic properties of the cantilever. It can be solved by

$$\begin{pmatrix} \Delta_x \\ \Delta_y \\ \Delta_z \end{pmatrix} = \begin{pmatrix} C_{xx} & C_{xy} & C_{xz} \\ C_{yx} & C_{yy} & C_{yz} \\ C_{zx} & C_{zy} & C_{zz} \end{pmatrix} \begin{pmatrix} F_x \\ F_y \\ F_z \end{pmatrix} \tag{2.6}$$

Since the photosensors detect not the tip deflection but the inclination of the cantilever top surface near its free end. Two angles are measure: deflection of the normal from vertical in the $yz$ plane (angle $\alpha$) and in the orthogonal from the $xz$ plane (angle $\beta$).

$$\begin{pmatrix} \alpha \\ \beta \end{pmatrix} = \begin{pmatrix} b_{\alpha x} & b_{\alpha y} & b_{\alpha z} \\ b_{\beta x} & b_{\beta y} & b_{\beta z} \end{pmatrix} \begin{pmatrix} F_x \\ F_y \\ F_z \end{pmatrix} \tag{2.7}$$

The magnitude and direction of the deformation cause by the vertical force $F_z$ can be determined by

$$\begin{aligned} \Delta_x &= C_{xz} F_z \\ \Delta_y &= C_{yz} F_z \\ \Delta_z &= C_{zz} F_z \end{aligned} \tag{2.8}$$

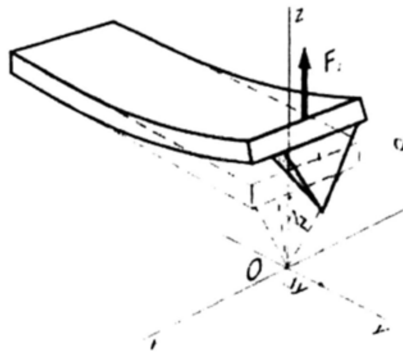


Fig. 2.6 Vertical deflection at the z-direction

When bending a beam having a length of $L$, the material at the outer edge is stretched in tension while the inner edge is being compressed. And there is a neutral plane of zero stress between the two surfaces.

When bending at the centroid of the beam, the material extension $\Delta L$ in the longitudinal direction is proportional to the distance $z$ from the neural plane as shown in Fig. 2.7.

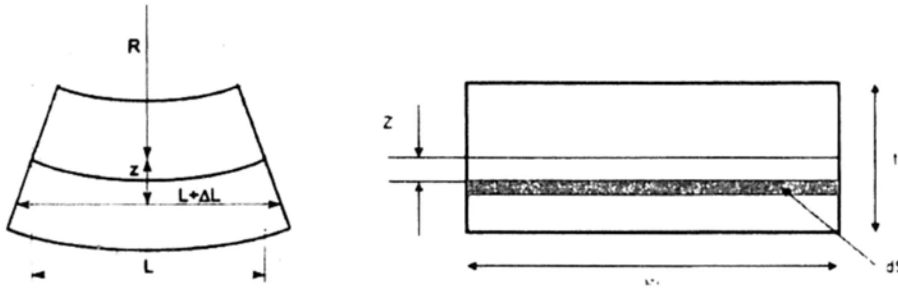


Fig. 2.7 Section of a bending beam and cross section of a beam

$$\frac{\Delta L}{L} = \frac{z}{R} \tag{2.9}$$

According to the Hooke's Low, the force acting on a unit area $dS$ is

$$dF = Ez\frac{dS}{R} \tag{2.10}$$

where $E$ is the Young's Modulus and $R$ is the beam curvature radius. For any cross-section, the forces acting over and below the neutral surface produce the bending moment $M_z$, which is the moment of forces with respect to the neutral axis:

$$M_z = \int_z zdF = \frac{E}{R}J_z \tag{2.11}$$

The quantity $J_z$ is the axial moment of inertia of the beam section. For a beam with rectangular cross-section, it is expressed as:

$$J_z = \int_z z^2 dS = \frac{wt^3}{12} \tag{2.12}$$

By denoting the deflection of the beam at a distance $y$ from then fixed end in the $z$

direction as $u(y)$. The bending moment can be expressed as

$$M_z(y) = EJ_z \frac{d^2u}{dy^2} \tag{2.13}$$

# Chapter 3

# An Integrated Nanomanipulation System with Haptic Device

## 3.1 Introduction

Nanomanipulation with is potentially useful for fabrication of prototype devices, modification of structures and construction of templates for other nanofabrication process. There are several techniques that can be employed for fabrication of microstructures such as photolithography [36], microcontact imprint [37], and scanning electrochemical microlithography [38, 39], but these methods posses significant limitation for patterning structures of nanometer scale. Since the capability to direct pattern polymeric materials at nano-scale creates a number of opportunities, nanomanipulation has been demonstrated in several systems such as electron beam exposure system [40], and scanning probe microscope [41] - [43]. Polymer and thin film have been patterned using Scanning Tunneling Microscope (STM) operated in vacuum, as well as using AFM under room conditions. For lithography, the AFM has a distinct advantage over the STM because AFM is used for insulting as well as conducting materials. And patterning by the AFM tip is a non-damaging process with higher precision of alignment and narrower width of lithography than those obtained by the use of photon, electron and scanning probe lithography. In addition, AFM is

relatively inexpensive when comparing to other means of nanomanipulation. This technique is compares favorably with others in cost, repeatability, accuracy and resolution.

Nanomanipulation with AFM usually proceeds in three steps: image the sample to locate the target position, then move to the position and change the operating parameters so as to increase the applied force to the particle, re-image to validate the results finally.

In contact mode, the AFM probe is in contact with the surface and various forces were used when two objects are brought within nanometers of each other. By indenting the tip onto the sample, patterning on a length scale below 10 nm is realized such as modification of polymer and direct patterning. Varying the magnitude of the applied load can perform either deep scratching or frictionless sliding. There are two ways to vary the applied force, which are either by setting the displacement of piezoelectric actuators on define distance along z-axis or tuning the trigger threshold value.

However, AFM-based manipulation is usually not instinctive to users and requires a high degree of training. With the aid of a force feedback device, direct positioning of the AFM tip with nanometer precision becomes possible. This section is mainly focused on discussing a teleoperated system with stereoscopic virtual graphical display and haptic force feedback. The graphical user interface was developed from

the topography data fed from the AFM, which displayed the surface topography and the position of the AFM tip on the sample. The topography data is scaled to perform the appropriate response on the force feedback device and users feel a force proportional to the height of the sample point interacting with the AFM tip. With the aid of the stereoscopic graphical display, users are allowed to perform the nanomanipulation in the virtual nanoworld. The force feedback device implemented in the system was with high sensitivity performance, which serves as a haptic interface that provides users with the sensation of tip-sample interactions. They are allowed to control the whole system by the haptic joystick and switch between navigation and manipulation mode. Scanning by using the AFM is a time consuming process and it was impossible to perform scanning during the manipulation process. In order to estimate the results for the operation, interaction forces between the tip and the sample were being modeled for the simulation. The results will be discussed in Section 4.

## 3.2 Design of Haptic Device

There are two critical parts in the design of the haptic device (Fig. 3.1), which are the joystick for providing force feedback to user and the track ball for 3-DOF motion control. The overall size of the device is $10cm \times 10cm \times 5cm$. There are 3 motor and gear system for generating the feedback force as well as to detect the force applied by

the operator as shown in Fig. 3.2.

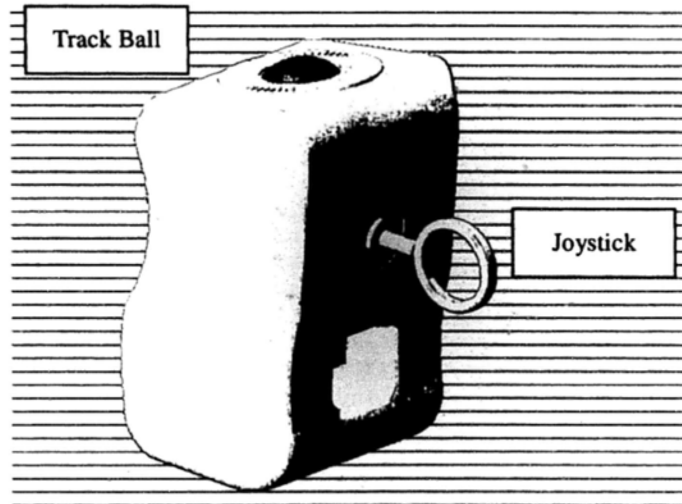


Fig. 3.1 Design of haptic device

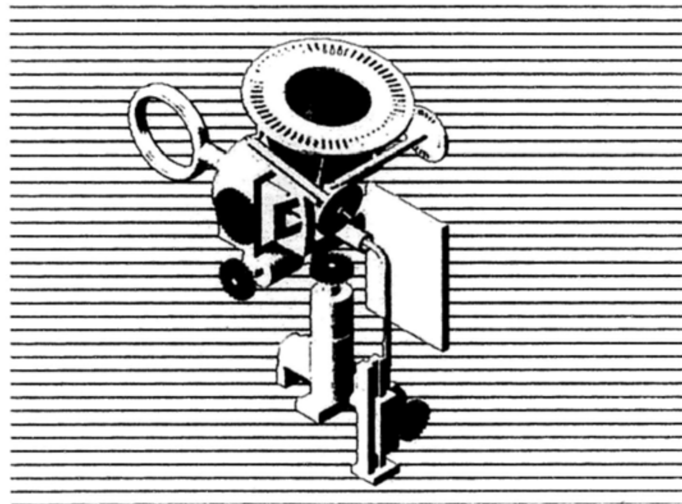

Fig. 3.2 Internal architecture of the haptic device

## 3.2.1 Belt Pulley System

In order to provide force feedback to user, 3 motors are used for generating the power. There are 2 belt pulley systems (Fig. 3.3) in the design for transmission of power between motors and the end-effecter. The belt length and center distance are

calculated.

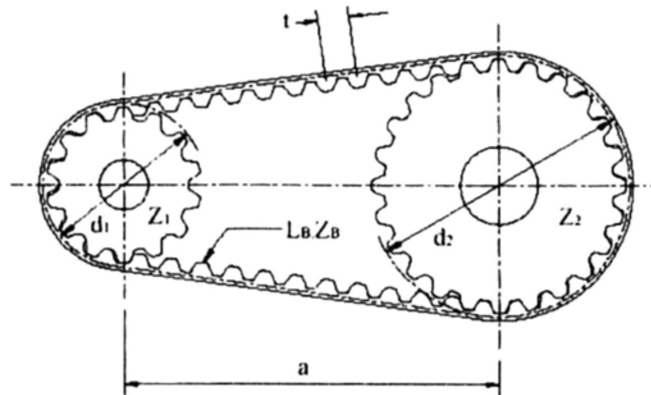


Fig. 3.3 Belt pulley system

In Fig. 3.3, $a$ is the centre distance, $L_B$ is the belt length, $t$ is the belt pitch, $d_1$ is the pitch diameter of the small pulley, $b_2$ is the pitch circle diameter of the large pulley, $Z_1$ is the number of teeth of the small pulley, $Z_2$ is the number of teeth of the large pulley, $Z_B$ is the number of teeth of the belt and $Z_e$ is the number of teeth in the mesh.

With the centre distance, the length of belt and chain can be calculated:

For $ratio = 1:1$

$$L_B = Z_1 \times t + 2a\,. \tag{3.1}$$

Otherwise,

$$L_B \approx \frac{t}{2}(Z_1 + Z_2) + 2a + \frac{1}{4a}\left[\frac{(Z_2 - Z_1)t}{\pi}\right]^2. \tag{3.2}$$

Knowing the belt of chain length, the center distance can be calculated:

For $ratio = 1:1$

$$a = \frac{(Z_B - Z_1)t}{2}. \tag{3.3}$$

Otherwise,

$$a \approx \frac{L_B - \frac{\pi}{2}(d_2 + d_1)}{4} + \left[\left(\frac{L_B - \frac{\pi}{2}(d_2 + d_1)}{4}\right)^2 - \frac{(d_2 - d_1)^2}{8}\right]^{1/2}, \text{ where} \tag{3.4}$$

$$d_1 = \frac{Z_1 \times t}{\pi} \text{ and } d_2 = \frac{Z_2 \times t}{\pi}. \tag{3.5}$$

## 3.2.2 Motion Tracking Mechanism

With the haptic device, the user is able to have 3-DOF motion control and the main objective of the motion tracking system is to translate the motion of the hand into the signal that could be recognized by the user interface. The motion tracking system is adopting the concept of a computer mouse.

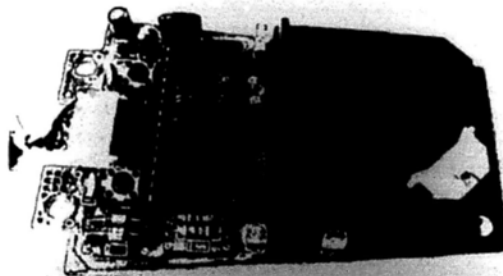

Fig. 3.4 Inner part of a computer mouse

Fig. 3.5 Motion detection in x and y directions

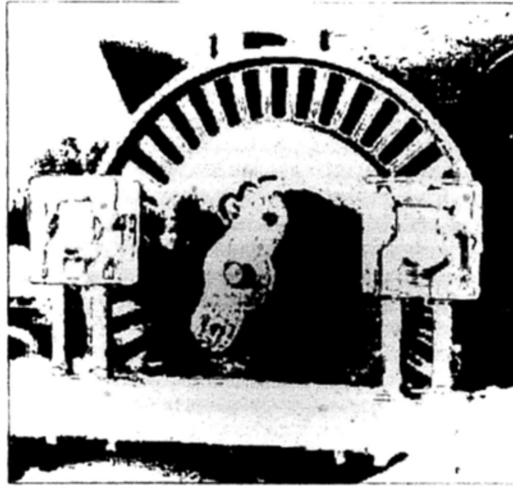

Fig. 3.6 Optical encoding dish with slits around the edge

Two rollers inside the mouse touch the ball as shown in Fig. 3.5. One of the rollers is oriented so that it can detect the motion in $x$ – direction, and the other is oriented in 90° to the first roller to detect the $y$ – direction motion. When the ball rotates, one or both of these rollers rotate as well.

The rollers are connected to a shaft, and the shaft spins a disk with holes in it (Fig. 3.6). When a roller rolls, its shaft and disk spin.

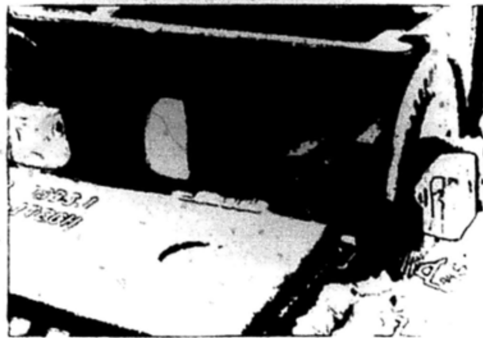

Fig. 3.7 LED source and infrared sensor

On either side of the disk, there is an infrared LED and an infrared sensor (Fig. 3.7). Slits in the disk break the light beam coming from the LED source such that the

infrared sensor detects pulses of light. The rate of the pulsing is directly related to the speed of the roller and the distance it travels.

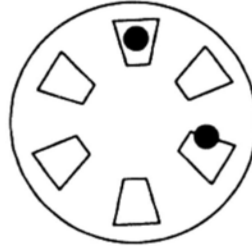

Fig. 3.8 Schematic drawing of the encoding system

The optical encoding disk is illustrated in Fig. 3.8, which is made of opaque material with multiple slots. Shinning through the slots are two LEDs represented by black dots. Each LED shines onto a corresponding sensor. The two LEDs are spaced such that only one LED could be detected and is therefore switching on and off.

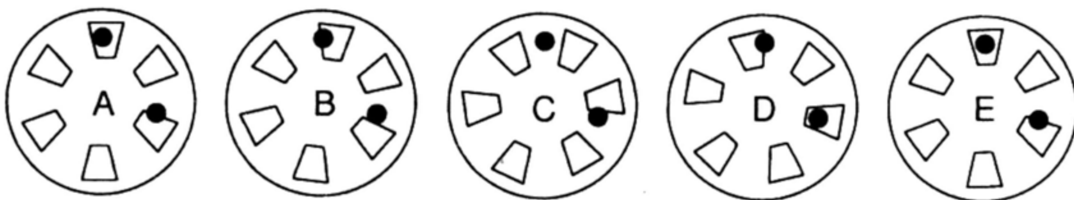


Fig. 3.9 Working principle of the encoding system

In Fig. 3.9, A is fully illuminated and B is switching. Note that B may switching from light to dark of from dark to light, it depends on the direction of rotation. During clockwise rotation, the states follow each other in the order A-B-C-D-E from left to right. It will correspond to an anti-clockwise rotation if in the opposite direction. LED

2 is changing state from light to dark in A for clockwise rotation and in C for anti-clockwise rotation. If LED 1 is being measured to be light when LED 2 goes from light to dark, then it is rotating in clockwise direction. The distance of travel is measured by the number of transitions. The two LEDs are interchangeable and both of them can be used as the step and direction. In the haptic device, there are three optical encoding systems; one rates for vertical movement, two rotate for horizontal movement. Signals received from the infrared sensors are sent to an on-board processor and being turned into binary data.

## 3.3 Integration of Manipulation System

The AFM employed for high-resolution imaging is based on a SPM control system (Being Nano-instruments, China), which processes the topographic data and generates the scanning image (Fig. 3.10).

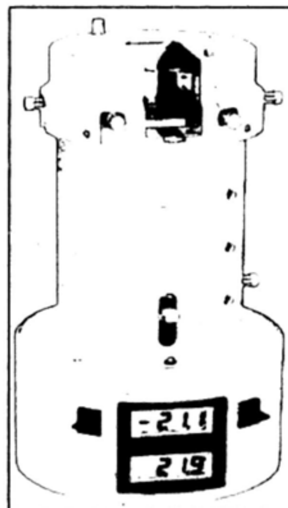

Fig. 3.10 Atomic Force Microscope

Motion of the sample holder is controlled by the piezoelectric actuators in three principle axes. Two piezoelectric actuators are in-plane with the sample, which generate the movements in the $x$ and $y$ directions. The last one is perpendicular to the sample based, which is responsible for adjusting the separation between the probe tip and sample surface. The AFM is capable for nano-scale positioning of the sample in $100\mu m$ range in the planar coordinates and $30\mu m$ in the vertical direction.

### 3.3.1 Vision Control System

The scanning stage is placed under an optical microscope, which is equipped with a high-resolution CCD camera for visual control (Fig. 3.11). Real-time image of the tip position is being captured and transferred to the system interface. It helps in determining the distance between the AFM tip and target position.

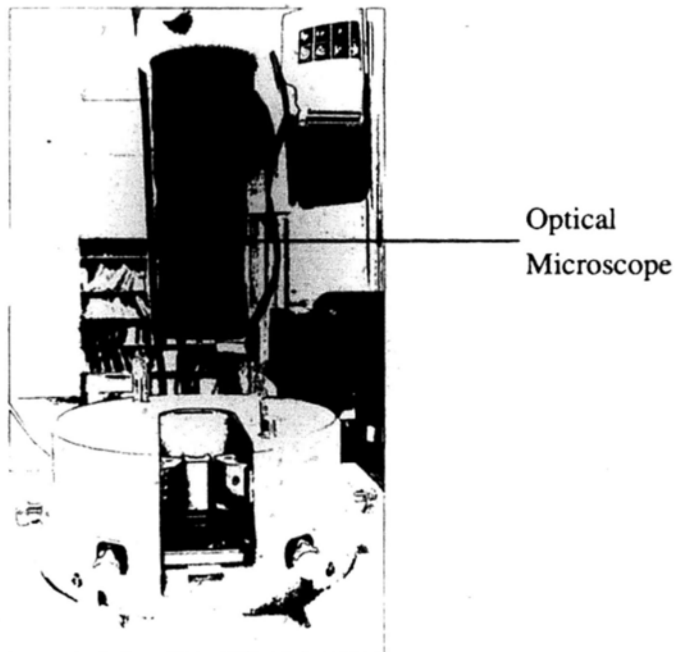


Fig. 3.11 Optical microscope for image capture

The vision system provides relative position feedback and there are some specifications when choosing a suitable one. First of all, the magnification of the microscope should be selected in such a way that the target objects can be visualized clearly. It is the measure of the difference in size between the target object and the image. Resolution is another important feature for the vision system, it must be able to distinguish, detect and record details of the target object and reproduce the image. The resolution of an optical microscope can be characterized by a modulation transfer function, which is the ability for the microscope to transfer contrast from the specimen to the intermediate image plane at a specific resolution. It also determines the lower limit of the object size to be manipulated. Besides, the working distance should be large enough for allowing the motion of the manipulator to be able to realize the manipulation task.

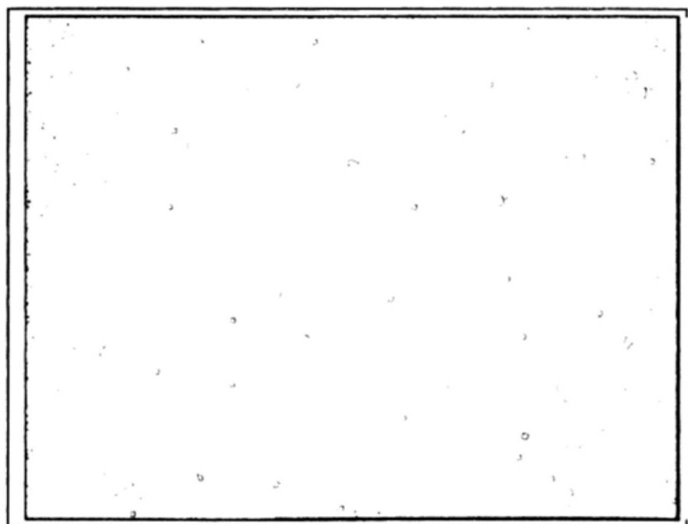

Fig. 3.12 Real-time image of the tip position

The amount of distance that allows the maintenance of acceptable image without refocusing, which is the depth of field, must be calculated. Although a narrow depth o field leads to precise focusing, it could be a problem if the focused image distance is not sufficient. In addition, the field of view, which is the visible area that can be seen, usually becomes smaller as the magnification increases. The limits of the visible area should be carefully considered according to the scale of the manipulation task. It brings the necessity of a variable zooming feature of the optical microscope in a wide range. However, higher magnifications bring narrower field of view and limit the workspace. A vision system, which is capable of having a coarse and fine imaging at the same time, can be the optimum solution. With variable zooming, the workspace information could be obtained from the coarse image, while detailed information can be retrieved from the fine image. Finally, illumination is a key issue for the vision system. Sufficient illumination should be provided and it should not cause the shadow problem while extracting the shape of the target object. The vision system is actually the sensor module of the whole configuration, which allows visually guiding of the manipulation task.

### 3.3.2 Coarse Positioning System

The manipulation system should allow the positioning of the end effectors with very high accuracy. Besides, it is necessary to scan a wide area as the target object may be

scattered over the substrate. The travel range must be adequate to provide a larger workspace area. Even for coarse positioning, the actuators should have sufficient accuracy in order to bring it into the range of motion of the fine positioning system. With the information feedback from the vision system, objects to be manipulated is moved into the visible area of the microscope. The final positioning is made by the find positioning stages with higher accuracy.

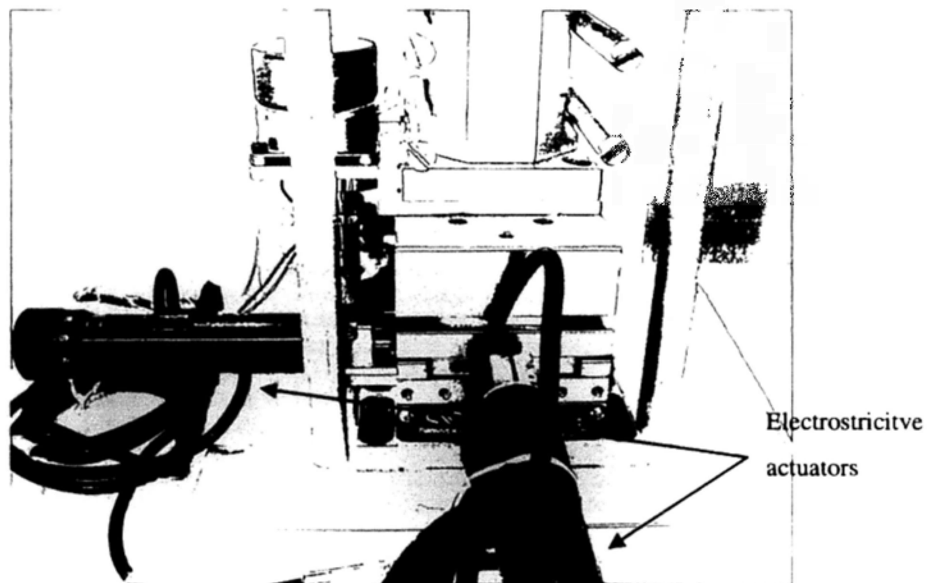


Fig. 3.13 Motion control System

The coarse positioning stages should provide enough travel distance to over the whole workspace area. A motion control system equipped with two ultra-precise electrostrictive actuators and high stability controller (Newport Cooperation, USA) is utilized for automatic localization. A high resolution encoder with resolution of $10nm$ per count is integrated to the DC motor. Minimum incremental motion of the translational stages is $50nm$ with speed up to $1mm/s$. The motion of the motion

control system is mainly depend on the calculated distance between the tip and the location under investigation.

### 3.3.3 System Interface

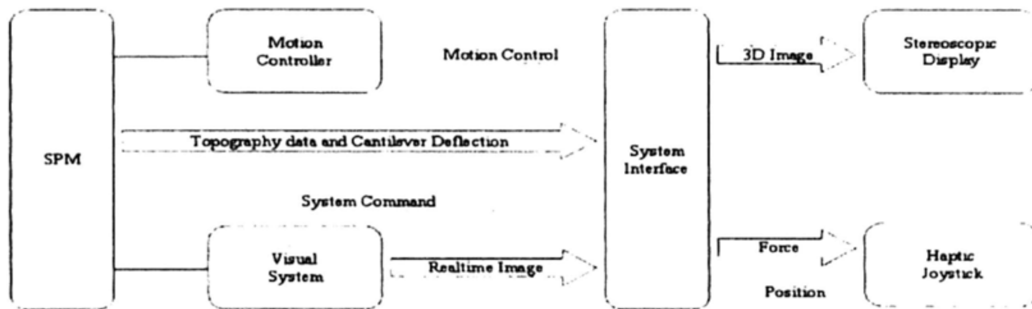


Fig. 3.14 Data transfer during manipulation

In the tele-operated system, signal received from the operator are transferred to the SPM system by means of a system interface, which is running under the Window operating system. It is client-server architecture, where the server is running in a PC that controls the AFM and the client is connected to the server by Ethernet. Clinet-server communication users standard interprocess communication primitives. During operation, different signals will pass through the system interface. User input from the haptic device is transmitted to the system interface and being converted into system commands for the SPM controller.

The topography data and cantilever deflection signals obtained by AFM scanning are sent through the system interface in real-time and the force feedback to the user could be calculated accordingly. The data is then transmitted to the haptic device and

stereoscopic display simultaneously for provision of force feedback and stereoscopic visualization. The user can therefore feel the scaled force between the interaction of the AFM tip and sample as well as visualize the operation. On the other hand, image captured by the CCD camera is sent through the system interface for localization of the sample, once the distance is being calculated, the tip will move to the target position defined by the user automatically.

## 3.4 Design of Graphical User Interface

The graphical interface was developed based on the topographic data obtained from the AFM. The 3D surface was generated according to the height data and operators are allowed to perform navigation in a virtual environment as shown in Fig. 3.15.

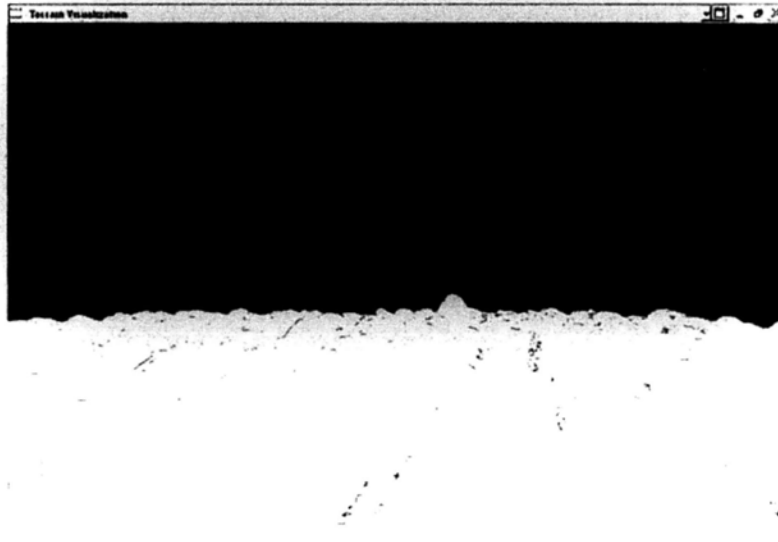

Fig. 3.15 User interface under navigation mode

Besides, users can execute other operation on the sample surface in manipulation mode as shown in Fig. 3.16.

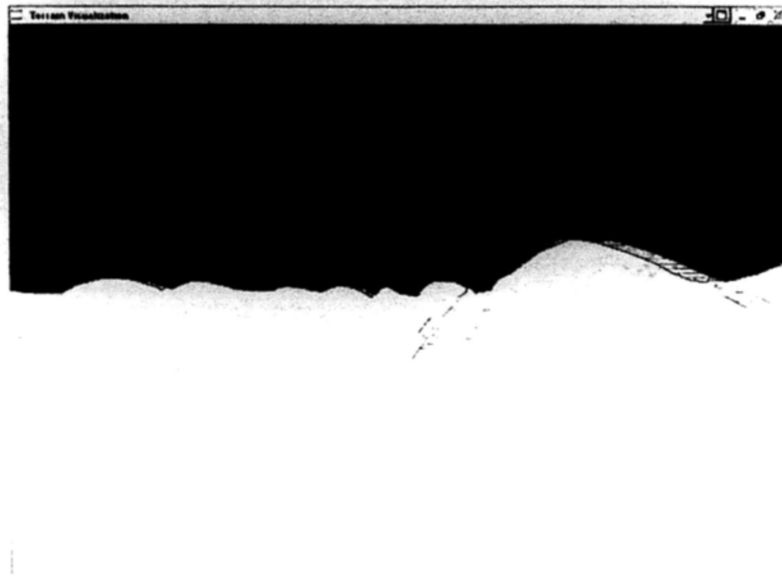

Fig. 3.16 User interface under manipulation mode

# Chapter 4

# Interatomic Force Modeling

## 4.1 Introduction

Forces acting between a cantilever and a surface are quite different and they are important for sample investigation. One or another force dominates at different tip-sample separations. During contact and the surface deformation by the cantilever, the elastic repulsion force dominates; this approximation is called the Hertz model. At tip-sample separations of the order of several tens of angstrom the major interaction is the intermolecular interaction called the Van der Waals force. At the same distance between the tip and the sample and in the presence of liquid films, the interaction is influenced much by capillary force and adhesion force, the range of capillary force is determined by the liquid film thickness. In this section, three models would be introduced for the simulation of the adhesion forces.

## 4.2 Interatomic Force Modeling

It was essential to determine the required applied force for obtaining an accurate result in nanomanipulation. The force could be simulated with the aid of contact mechanics, which describe the interatomic forces acting at the area of contact between the tip and the sample. It comprised the tip-sample interaction within the non-contact

regime and the adhesion force when tip and sample were being in contact.

## 4.2.1 Hertz Model

When the cantilever and the sample are in contact, elastic forces start to act and give rise to both the sample and tip deformations. The Hertz problem is deformations determination at local contact of bodies under load $F$ action. It assumes that both the cantilever and sample materials are isotropic, i.e. their elastic properties are described only by two pairs of parameters, Young's Moduli and Poission ratios. Also, in the vicinity of the contact point, the undeformed parts of body surface in perpendicular planes orthogonal to the plane are described by two curvature radii. Finally, deformations are small compared to curvature radii of surfaces

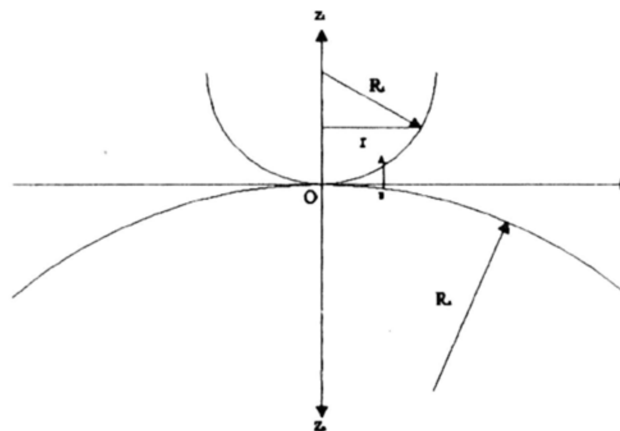


Fig. 4.1 Two spheres in contact at a point

The tip and sample were modeled as two spheres [44] as illustrated in Fig. 4.1. Consider the contact of a sphere of radius $R_t$ with elastic modulus of $E_t$ and Poison's ratio $\nu_t$ with the sample surface of radius $R_s$, elastic modulus of $E_s$, and

Poison's ratio of $\nu_s$. If there was no pressure applied between them, the contact occurs only at the point $O$ if in the absence of surface energy. If one sphere was forced down by a load $F$, the centers of the two spheres approached by a quantity $\delta$, and the contact was achieved on a circle of radius $r$. It was assumed that the ratio of $r/R_t$ and $r/R_s$ were both small, no friction occurred at the interface and no tensile stress exists in area of contact. The equations of the two circles were given by,

$$r^2 + (z_t - R_t)^2 = R_t^2 . \tag{4.2}$$

and

$$r^2 + (z_s - R_s)^2 = R_s^2 . \tag{4.3}$$

The distance between $A$ and $B$ near $O$ was expressed as a function of the radial distance $r$

$$AB = \frac{r^2}{2R} = h . \tag{4.4}$$

which $h$ was the distance between the probe tip and the sample surface as shown in Fig. 4.2 and $R$ was the effective tip-sample radius of curvature

$$\frac{1}{R} = \frac{1}{R_t} + \frac{1}{R_s} . \tag{4.5}$$

When a load was applied to the tip in contact with a surface such that the point at which load was applied moves a vertical distance $\delta$. If this distance was measured with respect to a distant point on the surface, this might be considered as the distance of mutual approach between the tip and the surface. In general, both the tip and

surface will undergo deformation. If the tip is rigid, there was no deformation.

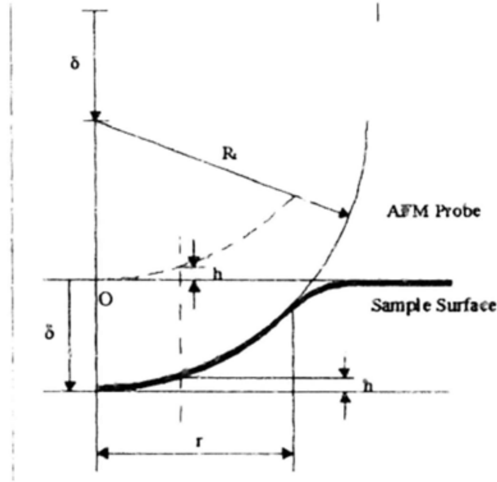


Fig. 4.2 Contact between two elastic spheres

In the presence of surface energy, the contact area sustained infinite stress on its periphery. It remained finite under negative loads until a critical traction force was reached at which the surfaces separate abruptly. The surface energy, $\gamma$ required to separate two flat surfaces from contact to infinity was defined as,

$$\gamma = \frac{H}{24\pi D_0^2} = \frac{W_{1,2}}{2}. \tag{4.6}$$

where $H$ was the Hamaker's constant. $D_0\ (= \sigma / 2.5)$, $\sigma = 0.4125nm$ was the typical interatomic distance, and $W_{1,2}$ was the work of adhesion.

The elastic modules of the two spheres were modeled as

$$\kappa_t = \frac{1 - \nu_t^2}{\pi E_t} \tag{4.7}$$

and

$$\kappa_s = \frac{1 - \nu_s^2}{\pi E_s}. \tag{4.8}$$

The effective elastic modulus, $\kappa$, was then expressed as

$$\kappa = (\kappa_t + \kappa_s). \tag{4.9}$$

In deformation status, the penetration depth is defined as

$$h = \frac{r^2}{R}. \tag{4.10}$$

The loading force ( $F$ ) and applied pressure ( $P$ ) can be defined as

$$F = \frac{Kr^3}{R} = K\sqrt{h^3 R}. \tag{4.11}$$

and

$$P = \frac{F}{\pi a^2} = \frac{1}{\pi}\sqrt[3]{\frac{FK^2}{R^2}}. \tag{4.12}$$

## 4.2.2 Work of Adhesion

Adhesion originates from the short-range molecular forces. The origin of adhesion forces between the probe and the solid is the molecular electrostatic interaction

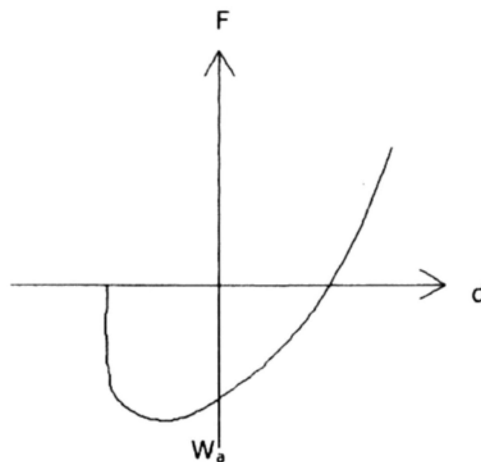


Fig. 4.3 The work of adhesion

Adhesion is a non-conservative process. Forces acting when the probe approaching the sample is differed from that during the probe retraction (Fig. 4.3). Such an operation requires some work to be done, which is known as the work of adhesion. The adhesion is caused by electrostatic forces at two bodies interface arising from the formation in a contact zone of the electric double layer. Its origin is different for materials of different type.

The adhesion is an irreversible process, when contact potential exists; electrons starts to drift resulting in the increase of entropy. This is why forces differ during the probe approach and retract, the process is thereby non-conservative. To describe the adhesion quantitatively some approximating models are used, such as the DMT model, JKR model and the Maugis mechanics.

### 4.2.3 Deriagain, Muller, Toropy (DMT) Model

In the DMT model, it is assumed that deformed surfaces geometries differ not much from that given by the Hertz Model. Taking into consideration of the Van der Waals forces acting along the contact area perimeter results in an additional probe-sample attraction, which weakens forces of elastic repulsion. This model is usually applied to probe tips with small curvature radius and high stiffness.

The loading force is defined as

$$F = \frac{Kr^3}{R} - 2\pi R\sigma . \tag{4.13}$$

The penetration depth is

$$h = \frac{r^2}{R} . \tag{4.14}$$

## 4.2.4 Johnson, Kendall and Roberts (JKR) Theory

The adherence force between two elastic spheres could also be measured by the Johnson, Kendall and Roberts (JKR) theory [45]. According to the JKR Theory, the contact force as a function of the contact radius was

$$F = \frac{Kr^3}{R} - \sqrt{\frac{3PKr^3}{R}} . \tag{4.15}$$

where $K = \frac{4}{3\kappa}$. The indentation, $h$, as a function of the applied force was

$$h = \frac{r^2}{R} - \sqrt{\frac{4\,\mathrm{Pr}}{3KR}} . \tag{4.16}$$

The JKR theory was applicable to systems where at least one solid has a high surface energy. It is usually applied to tips with large curvature radius and small stiffness.

## 4.2.5 Maugis Mechanics

The Maugis Mechanics is the most composite and accurate approach, which can be applied to any system and materials with both high and low adhesion. The amount of adhesion is determined by the parameter, $\lambda$

$$\lambda = \frac{2.06}{\xi_0} \sqrt[3]{\frac{R\sigma^2}{\pi K^2}} \tag{4.17}$$

where $\xi_0$ is the interatomic distance. DMT and JKR models can be regarded as

extreme cases of the Maugis Mechanics corresponding to different parameters. $\lambda \to 0$ for stiff materials (DMT) and $\lambda \to \infty$ for compliant materials (JKR). The Maugis Mechanics assumes that the molecular attraction force acts within a ring zone at the contact area border. The Maugis correction to the Hertz Model is expressed implicitly via a parameter $m$,

$$\begin{aligned} &\frac{\lambda r^2}{2}\left(\frac{K}{\pi R^2 \sigma}\right)^{2/3}\left[\sqrt{m^2-1}+\left(m^2-2\right)\tan^{-1}\sqrt{m^2-1}\right] \\ &+\frac{4\lambda r^2}{3}\left(\frac{K}{\pi R^2 \sigma}\right)^{1/3}\left[1-m+\sqrt{m^2-1}\tan^{-1}\sqrt{m^2-1}\right]=1 \end{aligned} \tag{4.18}$$

The loading force and penetration depth are

$$F=\frac{Kr^3}{R}-\lambda a^2\left(\frac{\pi\sigma K^2}{R}\right)^{2/3}\left[\sqrt{m^2-1}+m^2\tan^{-1}\sqrt{m^2-1}\right] \tag{4.19}$$

and

$$h=\frac{r^2}{R}-\frac{4\lambda r\sqrt{m^2-1}}{3}\sqrt[3]{\frac{\pi\sigma}{RK}} \tag{4.20}$$

respectively.

## 4.3 Lennard-Jones Potential

Denoted the initial position of the cantilever by $u$ and the displacement of the tip by $s$. The deflection of the cantilever, $d$, was described as $d = s - u$. The deflection of the cantilever was expressed as a function of the piezo displacement. The Lennard-Jones potential, $W$, was used for modeling of interactive forces in non-contact regime and was given by

$$W = \left[\frac{HR_t}{6\sigma}\right]\left[\frac{1}{210}\left(\frac{\sigma}{s}\right)^7 - \frac{\sigma}{s}\right]. \qquad (4.21)$$

The Lennard-Jones force, $F_L$, was obtained from the potential by taking the negative of its derivative with respect to $s$.

$$F_L = \frac{HR_t\left(-30s^6 + \sigma^6\right)}{180s^8}. \qquad (4.22)$$

The deflection of the cantilever as a function of the piezo displacement was expressed as

$$d(s) = \frac{F_L(s)}{k}, \qquad (4.23)$$

where $k$ was the spring constant of the cantilever. The tip jumps to contact with the surface or pulls out of the surface when the derivative of the force equaled to the spring constant. The values of snap-in and pull-out point were obtained by solving

$$\frac{dF_L}{ds} = k. \qquad (4.24)$$

## 4.4 Comparison of DMT, JKR and Maugis Models

The following table (Table 4.1) is a summary and comparison on the DMT, JKR and Maugis Models. With the selection of a suitable force model, the applied force and indentation depth can then be calculated accurately. Relationships between the contact radius and indentation depth is depicted in Fig. 4.4.

| Model | Assumptions | Restrictions |
|---|---|---|
| Hertz | No surface force | Not applied to small loads in the presence of surface forces |
| DMT | Long-range surface forces act outside the contact area | Contact area can be decreased due to the limited geometry. Applied to small λ |
| JKR | Short-range surface forces act within the contact area | Force magnitude can be decreased due to surface forces. Applied to large λ |
| Maugis | Tip-sample interface is modeled as a ring | The solution is analytical but equations are parametric. Applied to all λ values. |

Table 4.1 Comparison of quantitative adhesion models

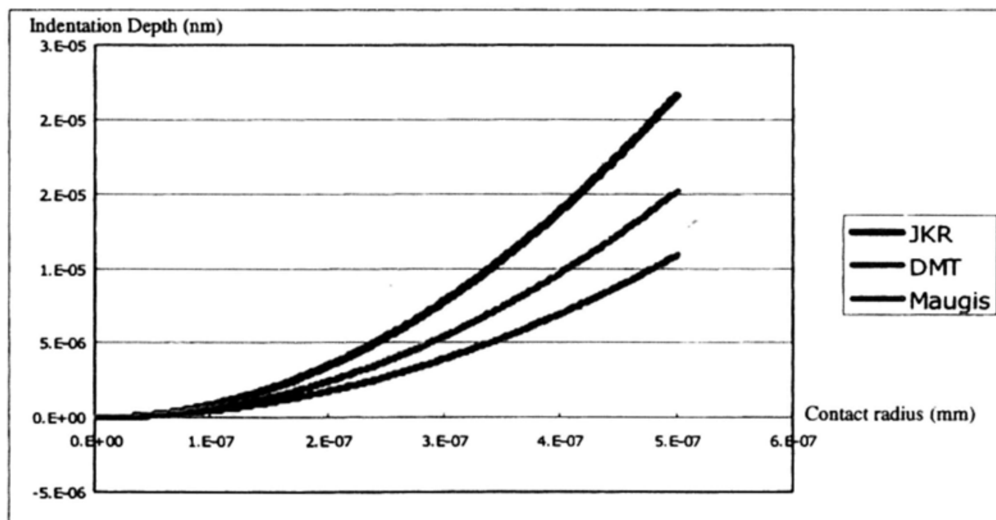


Fig. 4.4 Relationship between contact radius and indentation depth

# Chapter 5

# Validation of the Nanomanipulation System

In order to validate the performance of the integrated nanomanipulation system, it was being using to perform several testing including raster scanning, nanoindentation and nanomanipulation.

## 5.1 Raster Scanning

The study was performed under ambient conditions and a silicon nitride tip was employed in contact mode have a radius of curvature ≈ 10 nm and cone angle < 6°. For tapping mode, etched silicon probes with a nominal radius of curvature of ≈ 10 nm, and cone angle 36°, located on an I-shaped cantilever were used. In this mode, the tips were oscillated by the cantilever with amplitude < 100 nm at a frequency close of its resonance frequency (≈ 300 kHz). Images are analyzed with the developed software

AFM provides a unique means for direct observation of the sample surfaces. AFM images revealed the formation of particles during the deposition process. Additionally, the influence of some of the scanning parameters on the appearance of the particles could also be investigated.

AFM measurements explicitly showed that the deposition of polymer thin film provides formation of statistically homogenous self-assembled irregular structure on

the silicon substrate (Fig. 5.1 and Fig. 5.2). The results demonstrated uniform thickness and good adhesion to the substrate as the films were not destroyed during scanning. The measurements allowed to observe large-scale and small scale images of the thin films and provide real 3D data for successive analysis of the polymer material distribution with the film (Fig. 5.3).

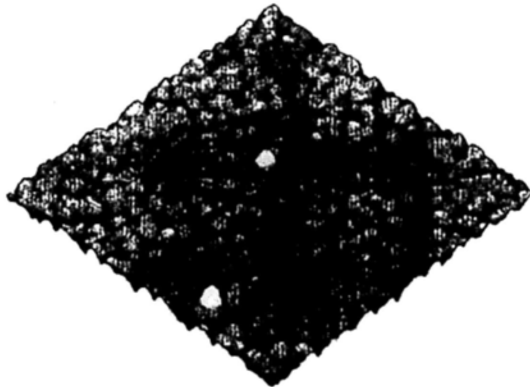

Fig. 5.1 Topography of a polymer layer in large scale

Fig. 5.2 Topography of a polymer layer in small scale

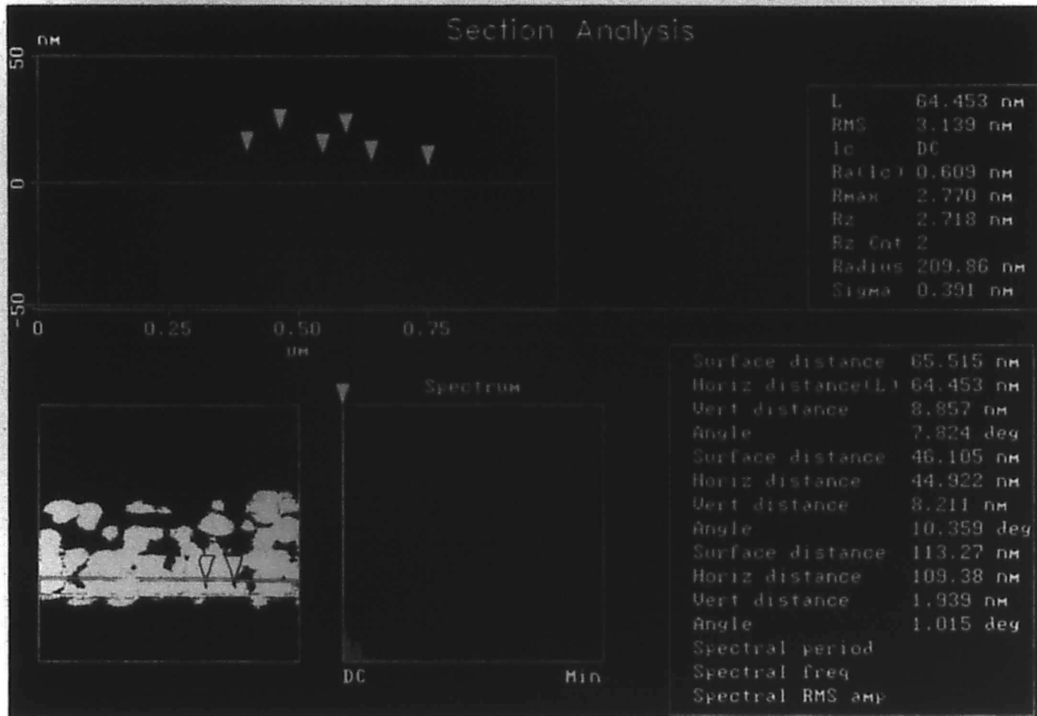


Fig 5.3 Section analysis of a polymer surface

## 5.2 Nanoindentation

Besides imaging, an AFM probe was also applied for nanoindentation at the same time. This eliminates the need to move the sample or relocation of the indenting area. Although cantilevers utilized for indentation are having higher spring constants than typical imaging cantilevers, it is still possible to scan soft samples with relatively low forces. It is possible using tapping mode AFM, which requires less force to image a sample than does contact mode AFM. The diamond tips are sufficiently sharp to provide good image resolution.

During the indentation process, a cantilever is first engage on the surface in tapping mode. While scanning, the sample surface may be imaged to find the desired location

for the indentation. Once the area of interested is identified, indentation starts. This halts the lateral scanning of the cantilever and lifts the tip slightly off the surface. Then, select the desired indentation parameters and execute the indentation. The cantilever oscillation is now turned off, and the scanner lowers the diamond tip towards the surface where the tip is forced into the sample surface until the cantilever deflects a specified amount. The tip is then retracted until it reaches the initial position above the surface. While indenting, a force displacement curve is recorded utilizing the DC displacement of the cantilever vs. the extension of the scanner. Many indentations may be made using various, forces, rates, etc.

Nanoindentation with an AFM cantilever is useful for investigating the hardness of films as thin as 5 nm. Since the macroscopic properties of thin films of a material may be different from the microscopic properties, the ability to perform tests at the nanometer level is of great importance in many processes. Fig. 5.4 shows indents on a polymer surface with a force of 15 μN and 25 μN. In the cross-section image (Fig. 5.5), the depth of the 15 μN indentation is only about 3 nm and the depth of the 25 μN indentation is about 7 nm. Using indentation, it is possible to indent various samples with the same force in order to compare their hardness.

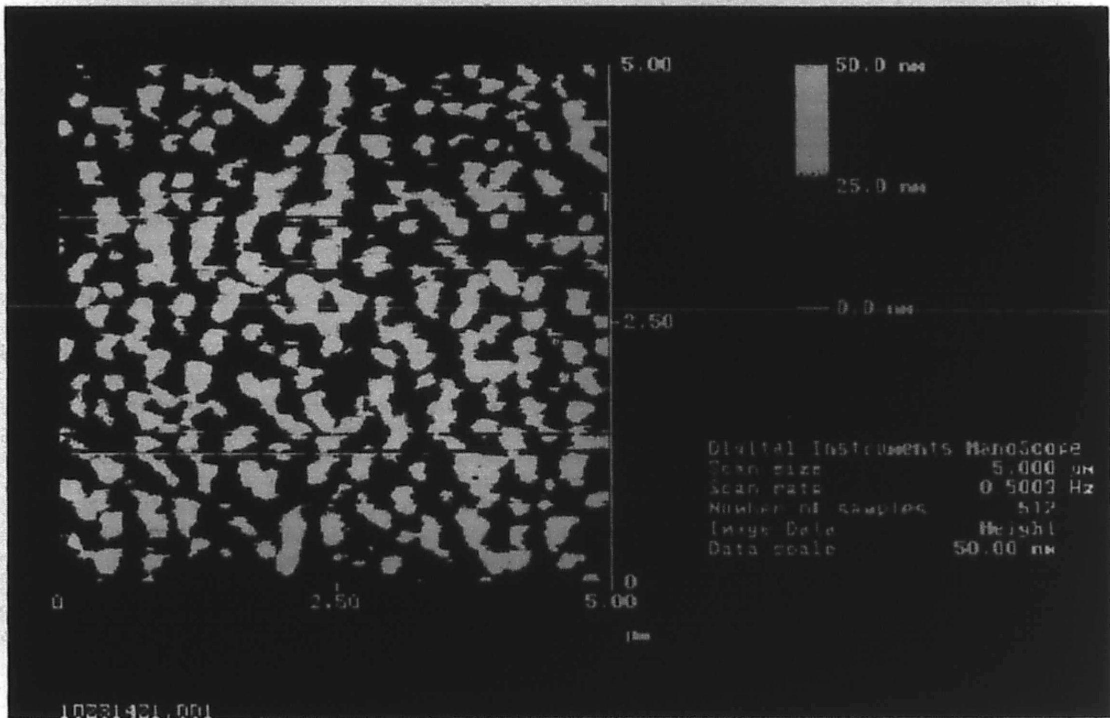


Fig 5.4 Indentations on a polymer surface

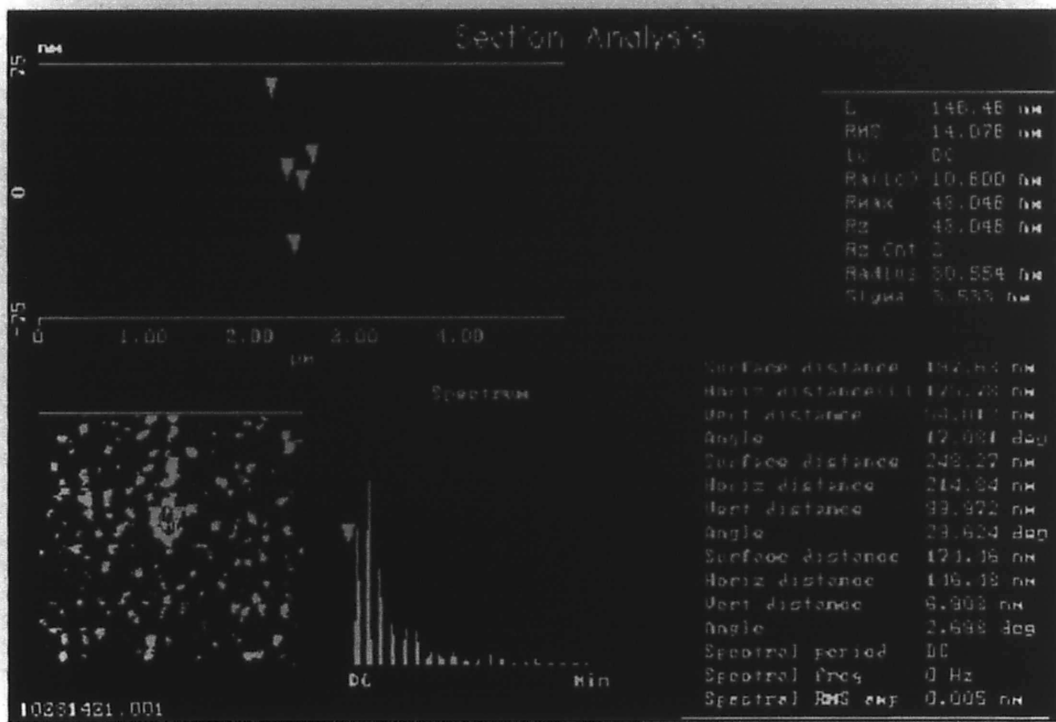


Fig 5.5 Section analysis of a polymer surface under nanoindentation

## 5.3 Nanomanipulation

The same cantilever also allows scratching and wears tests. This allows characterization of mechanical properties of thin films, using indentation to investigate hardness, and scratching and wear tests to investigate film adhesion and durability.

Scratching is done in a similar manner as nanoindentation by first engages on the surface and image the surface to locate the desired location for the scratch. Then, the lateral scanning halts and the tip is lifted slightly off the surface. Scratch is executed after setting the force, rate and direction. During scratching, the cantilever oscillation is turned off, the tip is forced into the surface until the specified cantilever deflection is reached, and the tip is then moved laterally according preset parameters. Multiple scratches may be made using various forces, rates, and directions.

Properties such as film adhesion and durability can also be studies using this technique. Fig. 5.6 and 5.7 shows a serious of scratches which were made at a force of 25 μN. The average depth of scratches is 78 nm. The material deposits, which have piled up near the scratches are likely peels of the film, which were scratched away from the surface. The films may also delaminate from the substrates causing taller features in the images.

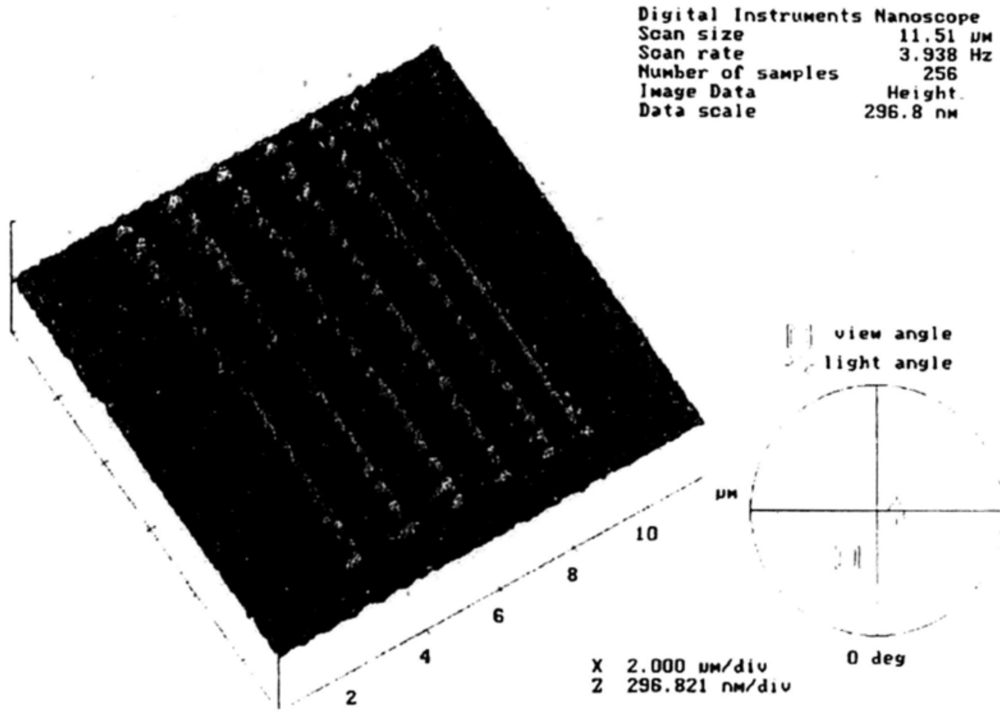


Fig. 5.6 Array of scratches performed on polymer a polymer thin film

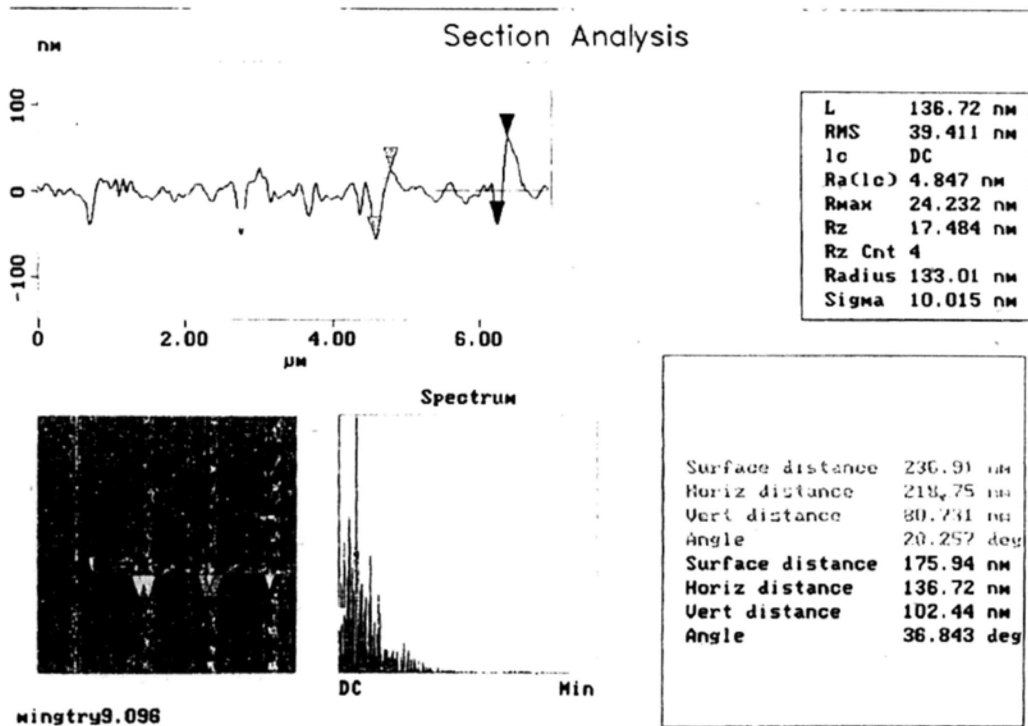


Fig 5.7 Cross section analysis of scratches

# Chapter 6

# Nano-mechanical Test of Nanowires

## 6.1 Introduction

Since the first observation of carbon nanotubes by Iijima in 1991 [17], physical and mechanical properties of carbon nanotubes are undergoing subsequent intensive investigations because of their extreme minute scale and surprisingly high reported mechanical strengths. Nanotubes are long, carbon fibres consist of graphite, closed at each end with caps which contain precisely six pentagonal rings. Two major types of carbon nanotubes are: single walled carbon nanotubes (SWNT) and multi-walled carbon nanotubes (MWNT). The nanotubes range in length from a few tens of nanometers to several micrometers, and in outer diameter from about 2.5 nm to 30 nm.

Several tests for the mechanical properties of SWNT have been carried out by several research groups [18] – [20]. On account of their outstanding properties, carbon nanotubes could be used, for example, in nanometer-sized electronics or to strengthen the tensile strength and elastic modulus of composite polymer materials. Several experiments verified that embedded carbon nanotubes lead to effective stress transfer [21] – [24]. Researchers have reported elastic properties for nanotubes that exceed 1 TPa and strengths that are many times higher than the strongest steel at a fraction of

the weight. Compared to carbon fibers, which typically have Young's modulus of 0.1 – 0.8 TPa [25], the elastic modulus of carbon nanotubes are in the range of 1 – 5 TPa [26].

The study of the nano-scale mechanical properties of surface to forces has become possible with the atomic force microscope [27] - [29]. The atomic force microscope has the ability to measure differences in response directly. Many techniques have been developed which take full advantage of the nanometer three-dimensional resolution offered by the ultra sharp AFM tip. Traditionally, the AFM has been used to measure the topography of surfaces through direct contact between the surface and a probe tip mounted on the end of a cantilever. AFM images are produced by the scanning of a probe across the surface of a sample using piezoelectric actuators. The high resolution imaging capability of AFM allows accurate localization of indentation sites and measurement of indentation depth. The AFM can also be operated under a force mode in order to perform indentation test. During AFM force mode, the probe tip is first lowered into contact with the sample, then indented into the surface, and finally lifted off the sample surface. Concurrently, a detection system measures the probe tip deflection. A force curve is produced, which is a plot of tip deflection as a function of the vertical motion of the piezoelectric actuator. This curve can be analyzed to provide information on the local mechanical response [30] – [32].

In this section, we will show that CNT-embedded micro bridges can be bent repeatedly by using the tip of an AFM. The evaluation of mechanical properties of carbon nanotubes is essential for the design of potential nanometer-scale piezoresistive sensors.

# 6.2 Calculation of Tip-Sample Adhesion

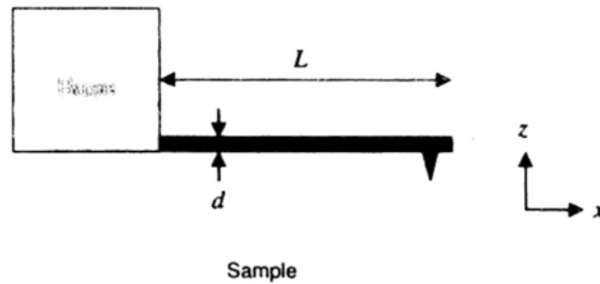


Fig 6.1 Schematic diagram of a cantilever and a sample

Fig. 6.1 illustrates the schematic diagram of the setup during scanning. The sample surface is in the $x-y$ plane while the cantilever is along the $x-$direction. The thickness of cantilever is $d$, and the height of the tip and its center position, away from the edge of the cantilever, are $h_t$ and $\delta$, respectively. During the scanning process, the surface of the sample exerts forces on the tip that will bend due to forces in $x-$ and $z-$directions.

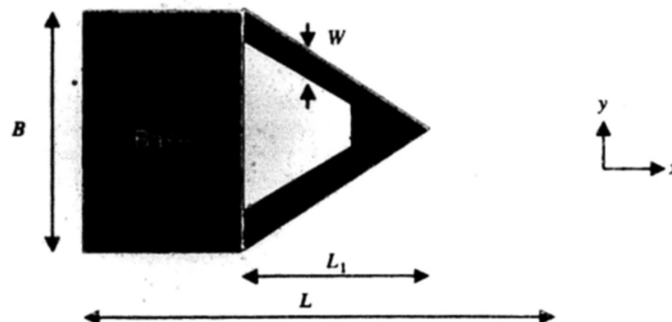

Fig 6.2 Illustration of V-shaped cantilever

Fig. 6.2 shows a typical V-shaped cantilever whose width and length are denoted by $B$ and $L$, respectively. $L_1$ is the height of the trapezoidal recess, $w$ is the width of each of the two arms. For $L_1 = 0$, one obtains a cantilever without a recess, while for $L_1 = L(1-2w/B)$, the recess becomes trapezoidal.

## 6.2.1 Spring Constant in z-direction

The local curvature of a cantilever $\rho$ is given in terms of Young's Modulus $E$ and the area of moment of inertia $I$

$$\frac{1}{\rho} = \frac{M_z}{EI} \tag{6.1}$$

The local curvature of a function $Z(x)$ is given by

$$\frac{1}{\rho} = \frac{d^2Z/dx^2}{\left[1+\left(dZ/dx\right)^2\right]^{3/2}} \tag{6.2}$$

Combining Eq. 6.1 and Eq. 6.2, and assuming a small curvature, leads to the equation of motion

$$\frac{d^2Z}{dx^2} = \frac{M_z}{EI} \tag{6.3}$$

For a V-shaped cantilever, the bending moment, $M_z(x)$ is given by

$$M_z(x) = (L-x)F_z \tag{6.4}$$

where $F_z$ is the force in the $z$-direction. The area of moment of inertia $I_1(x)$ is

$$I_1 = \frac{1}{12} w d^3 \tag{6.5}$$

While for $L_1 < x < L$, $I_2(x)$ is

$$I_2 = \frac{1}{12}\left(1 - \frac{x}{L}\right) B d^3 \tag{6.6}$$

The equations of motion are

$$\frac{d^2 Z_1}{dx^2} = \frac{M_z}{E I_1(x)} \tag{6.7}$$

and

$$\frac{d^2 Z_2}{dx^2} = \frac{M_z}{E I_2(x)} \tag{6.8}$$

respectively.

The deflection of the cantilever, $Z_2(x)$, can be obtained by integrating Eq. 6.7 and Eq. 5.8. The bending spring constant $k_z$, the maximum displacement $Z_{max}$ and angular spring constant $k_\theta$ can be calculated from

$$k_z = \frac{F_z}{V_2(x)(L - del)}, \tag{6.9}$$

$$Z_{max} = \frac{1}{k_z} \tag{6.10}$$

and

$$k_\theta = \frac{d_1 V_2(x)(L - del)}{F_z}. \tag{6.11}$$

Consider a V-shaped cantilever with a trapezoidal recess as shown in Fig. 6.2, define

its material and geometry as followed:

$\rho_{Xi} =$ 2330 $kg/m^3$
$E_m =$ $0.179\times10^{12}\ N/m^2$
$L =$ $190\mu m$
$L_1 =$ $87.5\mu m$
$B =$ $165\mu m$
$w =$ $33.3\mu m$
$d =$ $0.6\mu m$
$del =$ $7.1\mu m$
$h_{tip} =$ $3.5\mu m$
$F_x =$ $1nN$
$F_z =$ $1nN$

The numerical values are $k_z = 0.0982N/m$, $Z_{max} = 10.1848nm/nN$ and $k_\theta = 0.09373mrad/nN$.

## 6.2.2 Spring Constant in x-direction

The equation of motion for a force $F_x$ in the $x-$direction, is

$$\frac{d^2Z}{dx^2} = \frac{M_x}{EI}. \tag{6.12}$$

The bending moment, $M_x(x)$, is given by

$$M_x = h_{tip}F_x. \tag{6.13}$$

where $h_{tip}$ is the tip height.

Note that the area moments of inertia are also given by Eq. 6.12 and Eq. 6.13. The equations of motions for $x < L_1$ and $L_1 < x < L$ are

$$\frac{d^2Z_1}{dx^2} = \frac{M_x}{EI_1(x)} \tag{6.14}$$

and

$$\frac{d^2 Z_2}{dx^2} = \frac{M_x}{EI_2(x)}, \tag{6.15}$$

respectively. Integration Eq. 6.14 and Eq. 6.15 twice, the deflection of the cantilever, $Z_2(x)$, can be obtained. The bending spring constant $k_x$, the maximum displacement $Z_{max}$, and the angular spring constant $k_\theta$ can be calculated from

$$k_x = \frac{F_x}{V_2(x)(L - del)}, \tag{6.16}$$

$$Z_{max} = \frac{1}{k_x}, \tag{6.17}$$

and

$$k_\theta = \frac{d_1 V_2(x)(L - del)}{F_x}. \tag{6.18}$$

Consider a V-shaped cantilever with a trapezoidal recess as shown in Fig. 6.2, defining its material and geometry as followed:

$\rho_{Xi} =$ $2330 \quad kg/m^3$
$E_m =$ $0.179 \times 10^{12} N/m^2$
$L =$ $190 \mu m$
$L_1 =$ $87.5 \mu m$
$B =$ $165 \mu m$
$w =$ $33.3 \mu m$
$d =$ $0.6 \mu m$
$del =$ $7.1 \mu m$
$h_{tip} =$ $3.5 \mu m$
$F_x =$ $1 nN$
$F_z =$ $1 nN$

The numerical values are $k_z = 3.39889 \quad N/m$, $Z_{max} = 0.294213 \quad nm/nN$ and $k_\theta = 0.0047667 \quad mrad/nN$.

## 6.3 Bending Experiment

### 6.3.1 Fabrication of CNT-embedded Structures

The CNT-embedded MEMS structure was fabricated by a standard surface micromachining technology. As reported in [35], bundled CNTs were successfully manipulated across a pair of gold microelectrodes by using AC dielectrophoretic manipulation, there is a small gap distance (~ 3 μm) between the gold electrodes. In order to protect CNTs from contamination, a parylene C polymer thin film was used to embed the CNTs to provide a robust protection of the CNTs for a reliable measurement. Parylene C was deposited through an automatic parylene deposition machine and the deposition thickness is depended on the weight of the source parylene C powder. For the CNT-embedded structure used in this experiment, the thickness of the parylene C layer is around 0.3 μm. As mentioned before, the structure will be potentially used as micro piezoresistive sensors, which have the property of changing their resistance under physical pressure or mechanical work, an air gap under the CNT-embedded structure is fabricated for AFM bending experiments. To provide an air gap under the CNT sensor, a sacrificial layer (Al) was deposited on the substrate and then released in the final stage of the fabrication process. The thickness of the air gap is depending on the deposition thickness of Al and it is the maximum allowable bending distance. In this experiment, the height of the air gap is about 0.5

μm and the final structure of the CNT-embedded sensor is shown in Fig. 6.3.

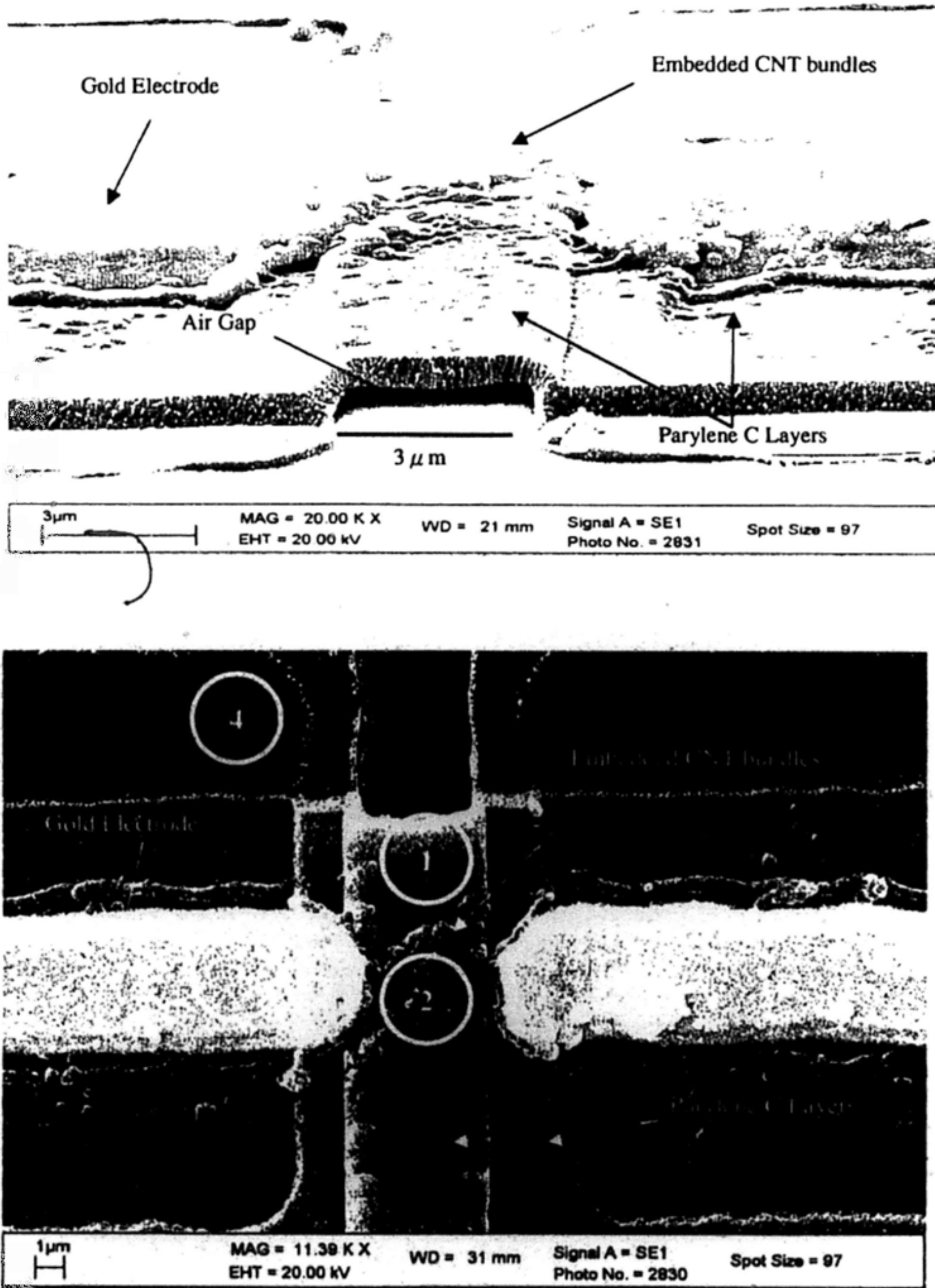


Fig.6.3 Scanning electron microscopic (SEM) image showing (a) the top view of CNT-embedded MEMS polymer bridge structure and (b) tilted at 70°

### 6.3.2 AFM Bending

The experiment is performed with the integrated nanomanipulation system described in Section III. A silicon nitride AFM tip is used to apply a nominal force and to measure the resulting deflection of the CNT structure. For a given material, the appropriate spring contact has to be chosen. Cantilevers made of soft material is insensitive to difference among hard materials, the piezo-scanner displacement is similar to the cantilever deflection, as a consequence, a large uncertainty in the surface deformation. On the other hand, if the cantilever is too hard, the plastic onset is reached for small values of cantilever deflection, implying insufficient statistics in the elastic region.

The nanoindentation technique was applied to the bending test of the MEMS structure embedded with bulk carbon nanotubes as shown in Fig. 6.3. The applied force, $F_a$, is given by:

$$F_a = k \cdot d \qquad (6.18)$$

where $k$ is the spring constant of the cantilever and $d$ is the cantilever deflection. The surface deformation, $\delta$, is calculated form $\delta = z - d$, where $z$ is the displacement of the piezoelectric actuator.

Before the bending test, the sample was scanned in a direction orthogonal to the axis of the CNT beam using tapping mode AFM, typically at a rate of 1.9 Hz, so that the

CNT-embedded micro bridge was located. The sensitivity of the cantilever was calibrated by acquiring curves of the cantilever deflection versus the displacement of the piezoelectric actuator.

Fig. 6.4 shows an example of the force-distance curve. The force plot is obtained under the force calibration mode. The horizontal axis shows the travel distance of the piezoelectric actuator and the vertical axis represents the deflection of the tip. As the piezoelectric actuator extends towards the sample surface, the tip deflection voltage remains constant until the probe tip makes contact with the surface due to attractive forces at point A. Just before tip-sample contact is made, the probe tip can be pulled down to the surface by attractive forces, causing a small decrease in the tip deflection voltage. After that, the tip is in contact with the surface and the tip further deflects as the piezoelectric actuator retracts, the tip goes beyond the setpoint and falls into the adhesive regime. Finally, the tip snaps free of the adhesive forces at point B. The horizontal distance between point A and point B along the retrace line indicates the distance moved by the tip in the adhesive regime. The adhesive force is obtained by multiplying the distance by the stiffness of the cantilever.

After scanning, the AFM tip was then positioned above the center of the micro bridge. The bridge was pushed towards the bottom of the "micro channel" by moving the AFM tip downward as depicted in Fig. 6.5. There are five load levels used to indent

on each particular area of the sample, using the same probe and operating conditions.

Each step of AFM tip-movement iteration was 0.139 μm.

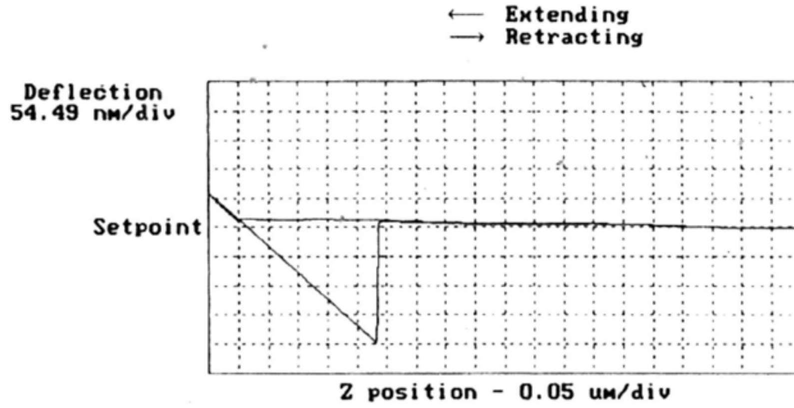


Fig. 6.4 AFM force-distance curve

The applied force and the maximum vertical displacement of the bridge were calculated from the following equations,

$$F_a = \left( \frac{(V_0 + V)}{s} \cdot k \right), \tag{6.19}$$

and

$$\delta = z - \frac{V}{s} \tag{6.20}$$

where $V_0$ is the initial differential voltage produced by the deflection of the cantilever before the bending test, $V$ is the differential voltage during the test and $s$ is the ratio of the differential voltage obtained from the cantilever's deflection to the displacement of the piezoelectric actuator in the z direction.

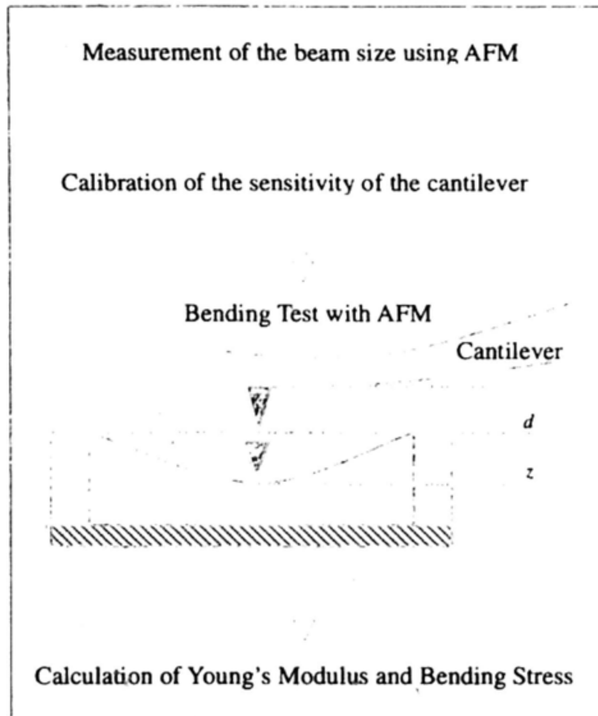


Fig. 6.5 Schematic diagram of the bending testing

In addition, based on AFM surface imaging, the force plots characterize that different material regions on the devices can be identified.

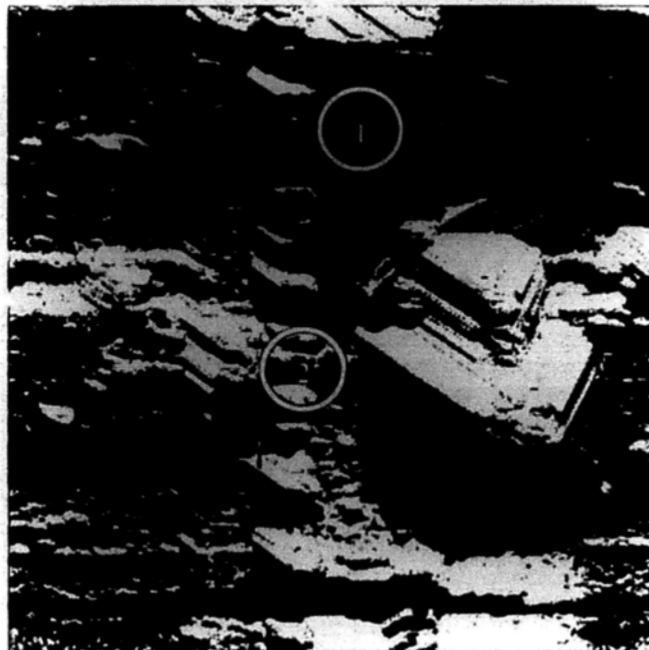

Fig. 6.6 Specific regions under the nanoindentation test

## 6.3.3 Discussion on Experimental Results

In this experiment, four different regions in the device were being investigated as shown in Fig. 6.3 and 6.6. The first region is the two parylene layers, and the second region is two parylene layers with CNTs embedded. Both regions have an air gap underneath. For the third region, it is the parylene layer with gold electrodes on silicon substrate. For the last region, it is only parylene thin film on silicon substrate.

To test the bending characteristics of the CNT-embedded structure, the micro bridge was push towards the bottom of the trench and then retracted. This experiment was repeated with different downward distance of the AFM tip. Once the bridge contact the bottom of the trench, the contact force increased, which allowed us to determine the actual depth of the micro channel. During the experiment, the AFM cantilever deflection was recorded. The mechanical properties of the micro bridge were calculated by the recorded contact force and the deflection of the micro bridge.

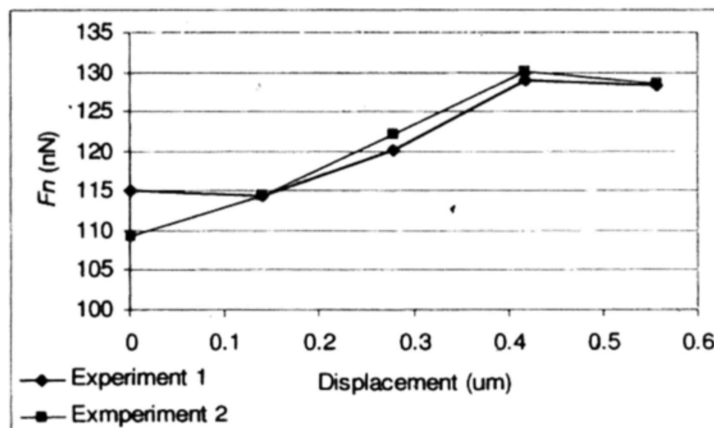


(a)

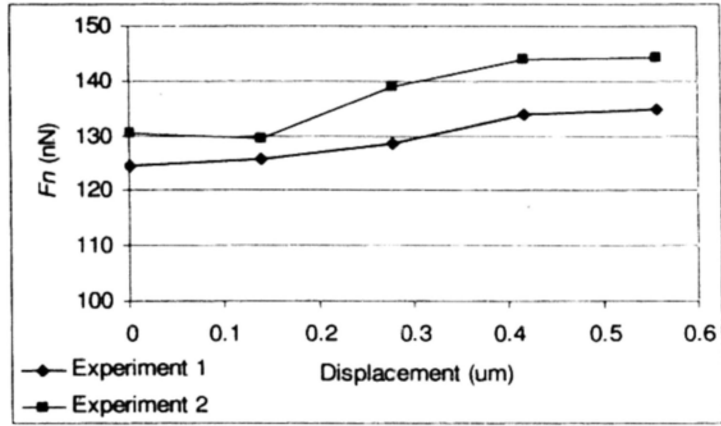


(b)

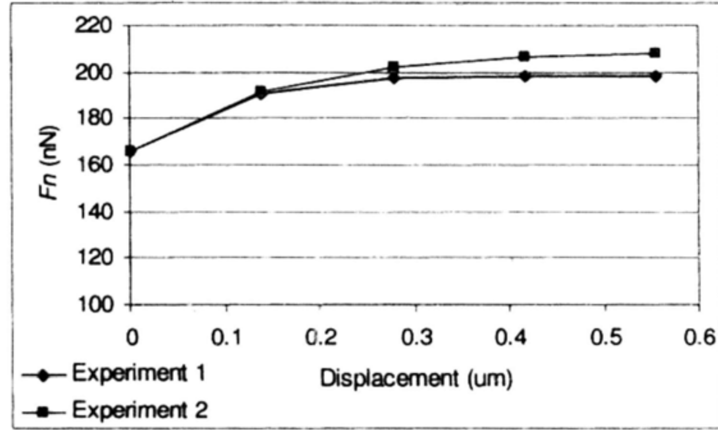


(c)

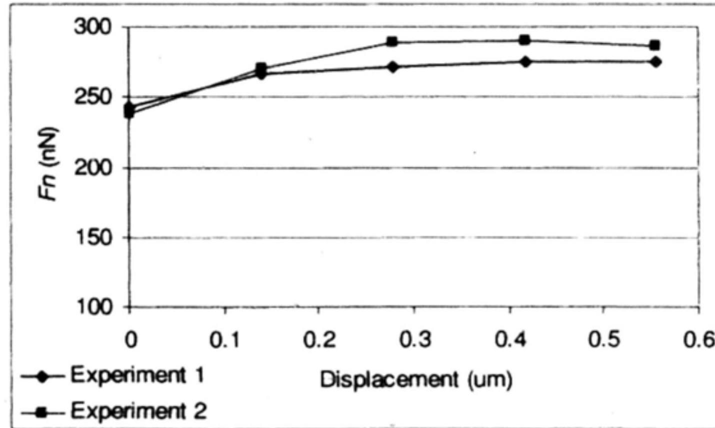


(d)

Fig. 6.7 AFM contact force data on bending the CNT-embedded structure with continuous pushing

The deflection of the bridge at its center region was evaluated from the cantilever deflection signal. As the initial tip-surface and the travel range of the AFM tip were under controlled, the micro bridge was deflected to various degrees and allowed us to study the effect of mechanical deformation on the electrical properties of the bundled CNT sensing elements.

The nominal contact force of the tip and sample was calculated and the results showed that forces applied to various materials such as gold, silicon and parylene polymer, varied with the displacement of the piezoelectric actuator during continuous pushing, The contact forces were found to be different for the same material on different substrates.

The contact forces are about 110 nN and 125 nN at the end point and the center point of the CNT bridge, where the forces on the surface of parylene on silicon substrate and on gold layer are 165 nN and 240 nN, respectively. This clearly showed that the contact forces vary with the structural composition of the structure that the AFM tip intends to "push".

With the continuous pushing on the sample by the AFM tip towards the surface of the sample, the forces increase with different gradients at different regions. Fig. 6.7a shows that the force increases from 110 nN to 130 nN at the end point of the CNT-embedded bridge. Fig 6.7b shows that the force increases from 125 nN to 135

nN at the center point of the bridge. Fig. 6.7c illustrates that the force increases from 165 nN to 200 nN at the region of parylene on gold surface. Fig. 6.7d shows that the contact force increases from 240 nN to 280 nN. The difference between the initial and final contact force is 13.4 nN to 10.4 nN, 31.9 nN and 33.2 nN, respectively. The variation of the contact force is due to the micro-hardness of the substrate underneath the top layer of parylene. The contact force increases more significantly on hard surface.

# Chapter 7

# Application of AFM Nanomanipulation in Photonics

## 7.1 Introduction

Diffractive optical elements (DOEs) are optical means which could manage the wavefront by diffraction. They are the basis of the majority of spectroscopic analysis, which is the study of electromagnetic spectra due to atomic and molecular interactions, on modern science and technology. With DOE, a specific light wave can be converted to a diffracted pattern with a desired distribution of its polarization by manipulating light and photons. The great advances in fabrication technologies, especially computer modeling and micro-fabrication [46] techniques have led to an explosion of applications of diffractive optical elements. Owing to the miniaturization of optical and electronic products, such kinds of micro optical elements are becoming more important. The gratings are found to be useful in optical photolithography [47], optical communications [48], and various industrial applications [49]. They are fulfilling their promise by replacing conventional optics in a variety of products.

A grating consists of a series of parallel grooves formed on a substrate, each grating groove is a very small, slit-shaped source of diffracted light. When monochromatic light is incident on a grating surface, the light diffracted by each groove is diffracted into discrete directions and combines to form a diffracted wavefront. The distance

between adjacent grooves and the angle of the grooves manipulate both the dispersion and efficiency of gratings. The grating efficiency is primarily a function of groove shape, angle of incidence and the refractive index of the substrate material. The absolute efficiency of a grating is the percentage of incident monochromatic light that is diffracted into the desired direction.

The extremely high precision required of a diffraction grating entails that the fabrication method must be controlled intimately. These elements are often associated with the use of nanotechnology for fabrication. The challenge of producing precision diffraction gratings has attracted the attention of many scientists. Gratings with microstructure arrays made of polymer have been studied for some time and several fabrication techniques have been proposed. Reactive ion etching can reduce surface damage and to achieve deep-side profiles, but it is difficult to manage the accuracy of the depth of etching. Laser-beam writing is a rapid, cost-effective technique for continuous and binary relief structures with feature dimensions down to about 1 μm and profile depths in excess of 40μm. But this process is rather complex if it is aim at revealing a precise surface structure. Hot embossing is suitable for foil application but not for high-performance diffraction gratings or any production with microstucture fidelity requirements. Photolithography, microcontact printing, and scanning electrochemical microlithography techniques can be employed for fabrication of

microstructures, but these techniques possess significant limitations for patterning structures of nanometer scale. Since the potential to direct pattern polymeric materials at nano-scale generates a number of opportunities, nanomanipulation has been demonstrated in several systems such as electron beam exposure system and scanning probe microscopes. Polymer and thin film have been patterned using Scanning Tunneling Microscope (STM) operated in vacuum, as well as using Atomic Force Microscope (AFM) under room conditions. For lithography, the AFM has a distinct advantage over the STM because AFM can be used for insulating as well as conducting materials.

The capability to design and manufacture products in a timely and cost-effective is the key to global competitiveness. The design process often makes several iterations through design and prototyping before completion. In this section, we demonstrate a mechanical method of prototyping diffractive grating optics for laser beam splitters and a light guide, which aim at improve productivity through greater design flexibility, rapid fabrication and cost reduction. AFM lithography has been utilized for fabricating high quality microstructure optics. By using this technique, it is possible to machine a sample surface in nanometer scale by direct machining without tooling fabrication. Patterning by the AFM tip is a non-damaging process with high precision of alignment and narrower width of lithography than those obtained by the use of

photon, electron and scanning probe lithography. In order to ensure the reliability of the design tool and fabrication process, experimental verifications have been conducted by comparing the predicted and actual performance of the laser beam splitter.

## 7.2 AFM Techniques and Cutting Tool Selection

For transmission grating, the diffraction angle is usually determined by the geometry of the triangular groove, which is also the geometry of the AFM probe tip in this experiment. In the design of the diffraction grating, the properties of the AFM probe tip should also be taken into consideration. Direct machining by using AFM can greatly reduce the fabrication time and cost comparing to some existing prototyping techniques. It is actually using the scanning probe with a fine tip to perform the nanomanipulation, which can create nanostructures on a substrate surface.

During the lithography process, the scanning probe is in contact with the substrate surface and scanned across it in a controlled manner. The pitch and depth of grooves are controlled by the applied force and the number of operating cycle. The applied force is governed by a feedback loop that produces voltage difference proportional to the movement of the piezoelectric actuators. Besides, the van der Waals force and adhesions forces exist between the atoms on the substrate and those on the tip of the scanning probe will cause the cantilever to deflect. These forces are considered as factors affecting the results and it is being recorded by the controller.

Owing to the properties of grooves, choosing an appropriate probe becomes critical. The selection criteria include substrate material, degree of resolution, shape of grooves and its aspect ratio. The probe is actually regarded as a cutting tool, combined with a suitable cantilever, it can probably provide sufficient applied force to remove

the material on a substrate surface. Usually, a high hardness probe with diamond coating is adopted and there is a layer of polycrystalline diamond coating of 100 nm presents on the tip sides. The tip radius is in the range to 100 – 200 nm with a nano-roughness of 10 nm.

## 7.3 Principle of CAE Optical Design

Computers are routinely used to design illumination systems. Automating the design process is enhanced through the use of optimization procedures. The computer-aided engineering (CAE) simulation tools allow us to virtually evaluate alternative designs without substantial models. The design process is more efficient and cost-effective through computational evaluation, time required for trail and error analysis is being eliminated. With the aid of CAE optical design, it becomes feasible to construct comprehensive physical models, define feature size and material properties precisely in a virtual environment.

The ray-tracing program is able to provide accurate simulation results and show the diffraction of each incident light ray on the grating. In addition, automating the design process is enhanced through the use of optimization procedures. Monte Carlo ray tracing provides accurate predictions of the output from an illumination system. The source is typically modeled as a collection of rays with position, angle, and magnitude that reproduce the 4D luminance distribution of the source. Such source models can be created as apodized emitting surfaces placed inside the traceable optical elements.

The rays from the source are traced through a model of the system's optical elements and are then collected on receivers. At the receiver, the rays are 'binned' in a number of ways to provide different output results such as the total flux, intensity, luminance, and chromaticity. The Monte Carlo binned performance predictions converge with a $1/\sqrt{N}$ relationship, where $N$ is the number of rays in a bin. For example, to get a prediction of $\pm 1\%$, then 10,000 rays are needed in a given bin.

## 7.3.1 Design Optimization

For the optimization procedure, it mainly includes parameterization, defining the merit function and application of the optimization algorithm. Optimization modifies a system based upon user specified performance criteria.

### 7.3.1.1 Model Parameterization

Parameterization is the selection of system variables, we need to know which parameters in the model can be varied in order to improve the system performance. All the parameters should be considered carefully in order to enhance the speed of convergence, and minimize the chance of becoming stalled at a local minima. The more variables, the longer it takes for optimization. Parameterization can be used to minimize the number of variables. Consider the groove pattern for a backlight system. Rather than making the size and position of each groove a variable, a parameterization scheme can be used to define how the groove size and position varies across the

surface. The parameters used to control the parameterization scheme are then varied by the optimizer.

### 7.3.1.2 Merit Function

The second step in optimization is to define the merit function, which is an indication for the efficiency of the optimization algorithm. There are several possible ways to construct a merit function; it could be the sum of the squares of the differences between a set of figures of merit function items and their associated target values. The basic relation is:

$$MF = \Sigma W_g \Sigma W_i^2 (V_i - T_i)^2 \tag{7.1}$$

where $W_g$ is the weight of the $g^{th}$ merit function group, $W_i$ is the weight of $i^{th}$ merit function item in group $g$, $V_i$ is the current value of the $i^{th}$ merit function item, and $T_i$ is the target value for the $i^{th}$ merit function item. For the merit function constructed as Eq. 7.1, the system is at its optimum when the gradient of the merit function is equal to zero. But for the system to optimize, it is not necessary for the system to attain a value of $MF = 0$. For the use of square in Eq. 7.1, it is the form required by the Damped Least Squares algorithm, which prevents the term in the sum from being negative and improve the stability of the optimization process.

The merit function can often progress through several orders of magnitude during the optimization process as illustrated in the logarithmically scale merit function plot in

Fig. 7.1. In the figure, the merit function is plotted as a function of iteration number, iteration includes the series of steps the algorithm takes while making it "best guess" at the optimal value. The value plotted is the merit function at the end of each series of steps.

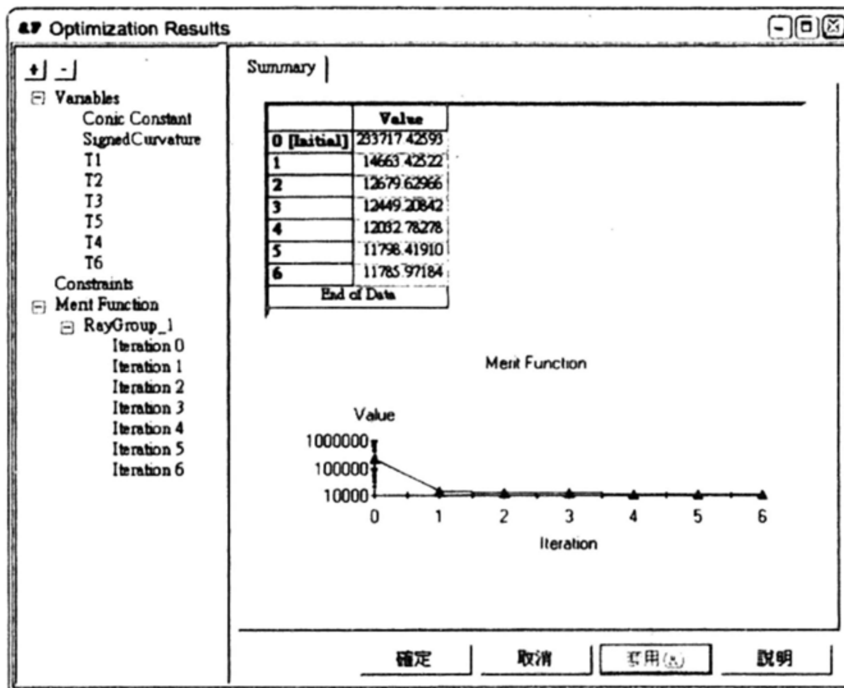


Fig. 7.1 Merit function value as a function of iteration number

The merit function is constructed from Monte Carlo ray tracing, which traces randomly selected rays and predicts performance measures by binning rays that fall within specified areas. The accuracy of the Monte Carlo predictions depends upon the number of rays traced.

For an illumination system, the merit function for a bundle of light rays can be specified using a sum of the squares approach. The ray aiming merit function is

$$MF_{group} = \sum_{i}^{Nrays}\sum_{j}^{Nitems} w_{i,j}^2 (V_{i,j} - T_{i,j})^2 + w_{loss} \frac{\sum_{i}^{Nrays}\sum_{j}^{Nitems} w_{i,j}^2 (V_{i,j} - T_{i,j})^2}{1 + N_{ReceivedRays}^2} \quad (7.2)$$

where $V_{i,j}$ is the value of the $j^{th}$ parameter of the $i^{th}$ ray, $T_{i,j}$ is the target for the $j^{th}$ parameter of the $i^{th}$ ray, $w_{i,j}$ is the weight of the $j^{th}$ parameter of the $i^{th}$ ray, $w_{loss}$ is the weight of the efficiency penalty term, $N_{ReceivedRays}$ is the number of rays that hit the receiver, $N_{rays}$ is the total number of rays traced, and $N_{items}$ is the number of different parameters for each ray that is used in the merit function.

The first term in Eq. 7.6 is the spot size term and the second term is the efficiency penalty. The efficiency penalty term includes the $1/N_{ReceivedRays}$ factor. This factor increase the value of $MF$ when rays miss the receiver and reduces the $MF$ when more rays hit the receiver. The efficiency penalty term allows the optimizer to distinguish when distinguish between a low and high efficiency system, especially the case where almost no rays hit the receiver. The weights in the merit function can be tailored to specific problems and the weights can be adjusted to provide physical meaning to the merit function.

### 7.3.1.3 Constraints

Constraints are the boundaries specified for an allowable optimization solution. A constraint can be defined as a mathematical relationship between the value of a parameter and a target value.

### 7.3.1.4 Optimization Algorithm

For an optimizer, the most important component would be the optimization algorithm. The optimization algorithm considers which parameters to change to obtain a better solution. There are any different types of optimization algorithms, the Damped Least Squares (DLS) and Noise Tolerant Optimization (NTO) are two common types.

DLS increments each variable by a small amount, then uses this information to compute derivatives, and ultimately a change vector for the system. It then applies this vector, and re-evaluates the merit function. The computations are performed during each iteration. Since derivatives are being used, DLS often converges quickly. However, the use of derivatives also makes it more sensitive to discontinuities or noise in the merit function.

The NTO algorithm does not use derivative information when it perturbs the variables. Its primary advantage is that it is far less sensitive to a discontinuous merit function as compared to DLS. This is particularly useful when the merit function is constructed using Monte Carlo ray tracing, a method which is intrinsically statistically noisy.

The parameterization, merit function and optimization algorithm can be described using the flowchart as shown in Fig. 7.2. The nominal flow starts by defining the problem and then evaluating the merit function. The merit function is compared with the target value for the merit function. If the desired criteria are not satisfied, then the

algorithm computes new values for the variables. The values for the variables are updated and the process will continue until the desired criteria are satisfied.

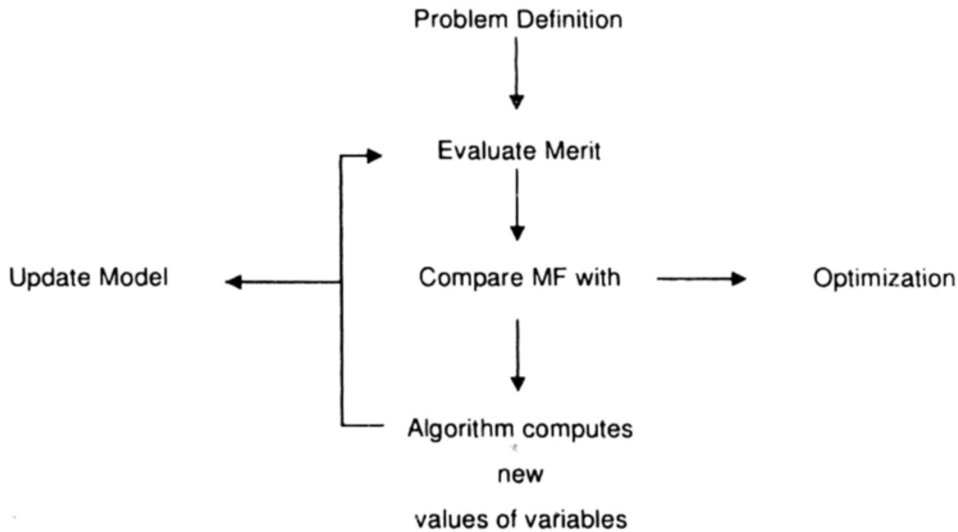


Fig. 7.2 Optimization flowchart

## 7.3.2 Design Modeling

In the CAE simulation, ray tracing is usually used to predict the performance of an illumination system. A crucial issue is to generate the model, including the light source and illumination optics, accurately. In the past, light sources were simplistically modeled as some basic geometrical shapes such as points, spheres, or cylinders. Nowadays, the design software will allow us to create a more complex theoretical model of the light source that could include multiple geometrical shapes to more closely approach the actual properties. Below is a discussion of the source modeling techniques.

Point source models are limited in application as they only provide reasonable accuracy when the size of light source is very small relative to the distance of the optical elements. In addition, the source must be radiate uniformly in all directions. A spatial map of the source radiance will take into account of the physical dimensions of the source and improves the model accuracy. This is quite accurate for predicting system uniformity when the optics only collects light emanating from the source over a relatively small solid angle. But it is not possible to accurately predict the overall system efficiency if the true radiance of the source is over $4\pi$ steradians.

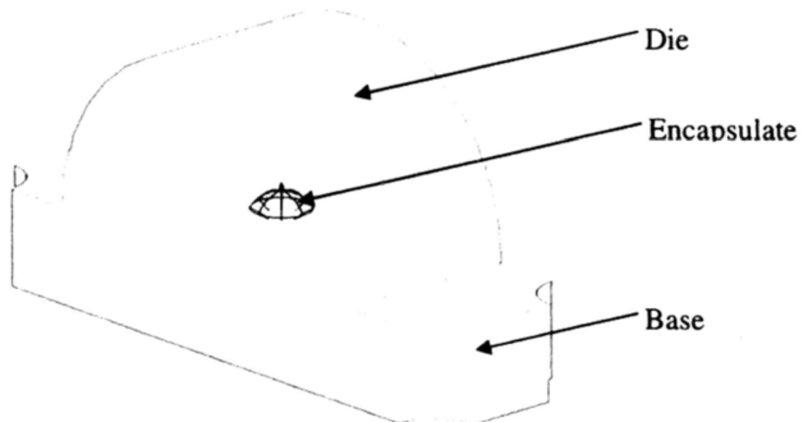


Fig. 7.3 A complex geometrical LED model

For complex geometrical source models, they can be described from a combination of basic geometrical shapes such as cubes, cylinders and spheres. A detailed model can approximate the variable source radiance as a function of view angle. In order to create an accurate model, careful measurements of all the geometry and optical properties are necessary. For a LED, there are some critical components such as the

die, encapsulate and base. The size of these components must be measured under an optical microscope so as to create an accurate model as shown in Fig. 7.3.

The power (total flux) of light source is usually measured by an integrating sphere (Fig. 7.4), which is a highly reflective enclosure placed in close proximity to the source, such that the reflected light enters the sphere, bounces around the highly reflective diffuse surface of the wall and finally impinges upon the detector. The surface of the wall should approach the ideal Lambertian scatter surface, which means that the light falling on the surface is evenly scattered in all directions and the scattered light intensity is proportional to the cosine of the angle of observation.

Fig. 7.4 An integrating sphere

On the other hand, the spatial distribution is usually measured by a goniophotometer (Fig. 7.5). It measures the intensity of the light source at a range of angles from -90° to +90°, where there is a built-in motor that allows the system to rotate and measure

the source under this range. The spatial distributed is expressed in luminous intensity (mcd) vs degree (Fig. 7.6).

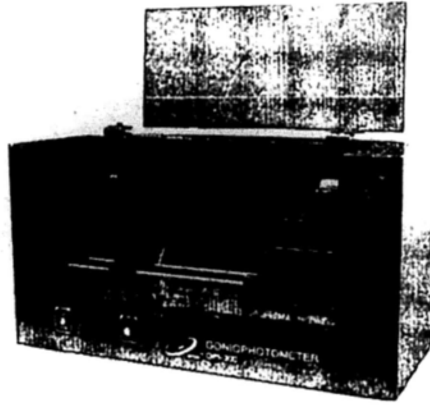


Fig. 7.5 Goniophotometer

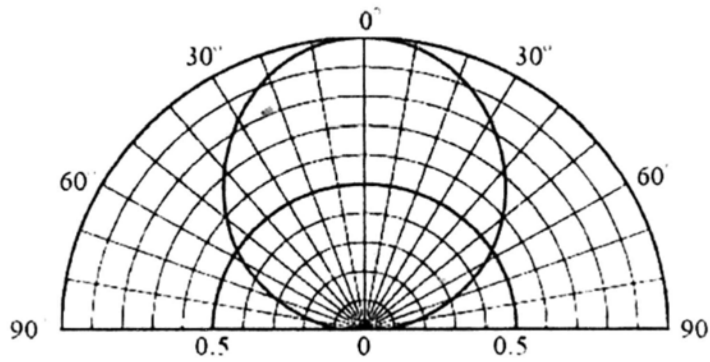


Fig. 7.6 Spatial distribution pattern

# Chapter 8

# Diffractive Optics Elements

## 8.1 Introduction

Beam dividers allow the identical replication of any type of monochromatic beam, diffracted beams travel in predefined directions. Diffraction grating ruled with linear array of triangular grooves can be used as beam dividers for spectroscopic purposes. Some of them vary the grating heights along their length in order to obtain a desired beam shaping pattern. Light produced by a monochromatic source can be manipulated, so as to diffract a single light beam to several beamlets. An advantage of diffraction grating is that a single optical element can replace compound optical components to customize the beam profile to the desired shape and intensity distribution at high diffraction efficiency. A subsequent collimation results in parallel beams with a precise distance between each other.

The optical design of the diffraction grating should reference to its application. There are a several properties, which govern the characteristics. In order to justify tradeoffs between performance and fabrication requirements, effects of these parameters are better to be determined in advance. For a given pitch ($d$) between grooves, the diffracted light from each facet is in phase with the light diffracted from any other facet and combine constructively. A light ray of wavelength $\lambda$ incident at an angle

$\alpha$ and diffracted by a grating along angles $\beta$ as shown in Fig. 8.1.

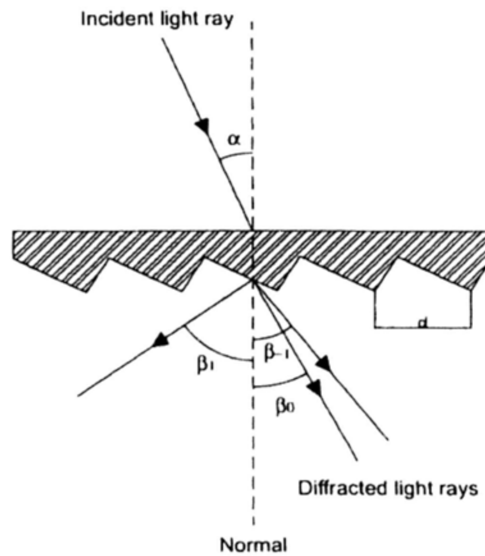


Fig. 8.1 Diffracted light rays through a transmission grating

These angles are measured from the normal of the grating, which is perpendicular to the center of the grating surface. The path difference between diffracted light from adjacent grooves is expressed as

$$m\lambda = d(\sin\alpha + \sin\beta). \tag{8.1}$$

where $m$ is an integer, which is the diffraction order. When the path difference equals to the wavelength of the incident light or its integral multiple, the diffracted light from adjacent grooves will be in phase. For a particular wavelength, any diffraction order will exist only if

$$\left|\frac{m\lambda}{d}\right| < 2. \tag{8.2}$$

When $m = 0$, the grating becomes a mirror and light is being reflected, it is called

specular reflection. There is another situation when $\alpha = \beta$, the light is being diffract back toward the incident direction and it is called Littrow configuration, the grating equation becomes

$$m\lambda = 2d \sin \alpha . \tag{8.3}$$

In addition, based on the periodic nature of the electromagnetic wave, there is no difference between a $2\pi$ and $m \cdot 2\pi$ phase delay. The maximum thickness ($t_{\max}$) of grooves can be expressed as

$$t_{\max} = \frac{\lambda}{n-1} . \tag{8.5}$$

where $n$ is the refractive index of the substrate. These fundamental grating equations are commonly used to design an optical system.

## 8.2 Design Considerations

### 8.2.1 Grating Efficiency

For a diffraction grating, both efficiency and its variation with wavelength and spectral order are important characteristics. The absolute efficiency is defined as the power of monochromatic light being diffracted into the order being measured, relative to the incident light. A high-efficiency grating is more useful in measuring weak transition line in optical spectra. Also, it may imply lower instrumental stray light due to other diffracted orders, as the total power for a given wavelength leaving the grating is conserved.

The grating efficiency varies for different diffraction order, $m$. The peak efficiency decreases in magnitude and shifts towards lower magnitude of wavelength as $|m|$ increases. For gratings with coarse pitch ($d \approx 2\lambda$), the efficiency is about half its peak wavelength when $m = 1$.

The efficiencies are typically 20 % less in the second order as compared with the first order. On the other hand, gratings with fine pitch ($d \approx \lambda$) usually have lower peak efficiency but the effective range of wavelength is greater. Moreover, it also depends on the angles of incidence and diffraction, the groove spacing and the substrate material. The peak wavelength generally occurs when the direction of refraction equals the direction dictated by the grating equation. In order to design a high-efficiency grating, groove spacing and diffraction angle have to be defined carefully.

### 8.2.2 Stray Light Characteristics

For an optical system, there always exists some undesirable light, which is referred to stray radiant energy (SRE). The SRE contributes to the noise of the system and thereby reduces the signal-to-noise (SNR) ratio. The radiation incident on the surface of the grating, some will be diffracted and some will be absorbed by the grating itself. The remainder is scattered light, which may arise from several factors, including defects in shape, spacing of the grooves and roughness of the surface. A

comprehensive analysis of grating scatter can be found in [50].

A grating surface that is rough on the scale of the incident wavelength will cause a small portion of the incident light to be scattered into all directions with intensity that varies approximately with inverse 4th power of the wavelength [50]. The presence of spatial frequencies in the groove pattern other than that of the groove spacing $d$ will give raise to constructive interference of the diffracted light at angles that do not follow the grating equation for the nominal groove spacing, $d'$, but for difference spacing $d' \neq d$. On the other hand, a distribution of groove depths about the nominal groove depth is a natural consequence of the developing conditions. These variations have been shown to generate a continuous distribution of scattered light that varies with the inverse cube of the wavelength.

In order to reduce the stray light, a grating is better designed with a groove spacing which is only the first and zero orders propagate. Also, it is more preferable for a system to contact only a few optical components. It is because each optic is a source of scatter, and it will reduce the SNR ratio. If possible, optical components with ultra smooth surfaces are more preferable.

## 8.3 Optical Design of a Beam Splitter

Once the source and diffraction angle is defined according to the application, those parameters for the microstructure can be optimized by using the CAE simulation. In

this design, we have designed a diffraction grating for beam shaping.).

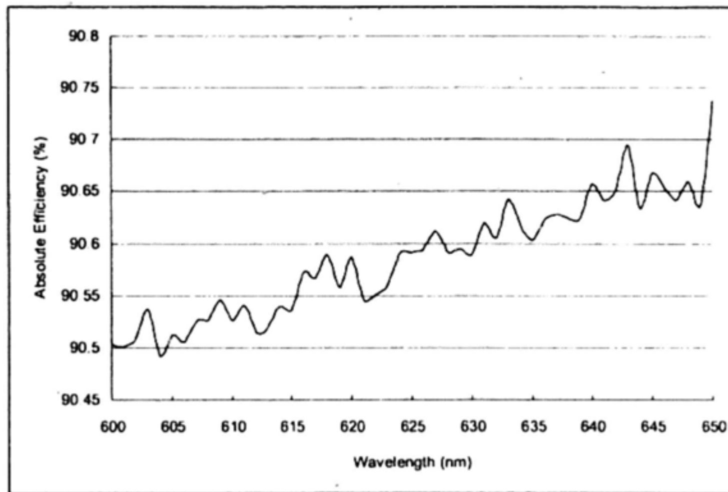


Fig. 8.2 Transmission rate measured by a Photospectrometer

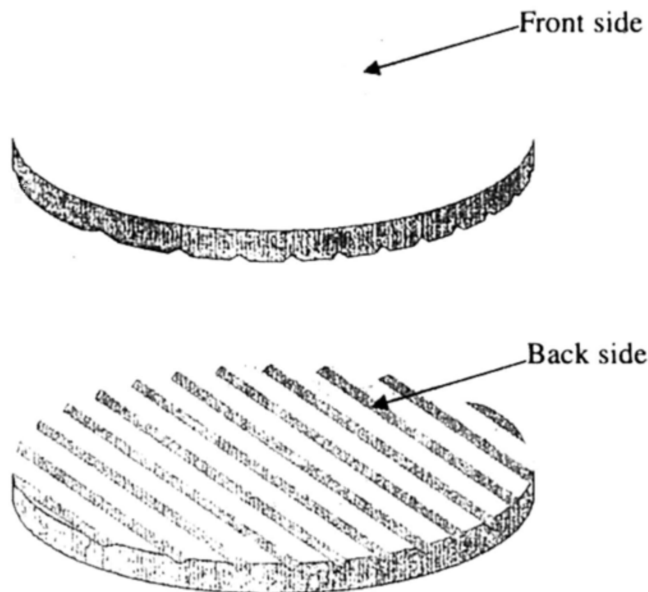


Fig. 8.3 DOE with V-shaped gratings

The light source was a laser diode with size of 100 $\mu m$ and the peak wavelength is 635 $nm$. The substrate material was chosen to be PMMA with a refractive index of 1.491. PMMA is a transparent material with a high transmission rate, which is 90.6 %

at 635 $nm$ as measured by the photospectrometer (Fig. 8.2). At the backside surface, there was a plurality of V-shaped grooves, where the emission surface was a plano surface as shown in Fig. 8.3.

The grooves were parallel to each other and with variable pitch and depth. Light beams emitted from the light source were being diffracted in different directions through the optical component. Depending on the diffraction order, some light beams reaching the grooves were refracted at an angle, others reaching the plano surface were refracted and emitted from the front side surface as illustrated in Fig. 8.4.

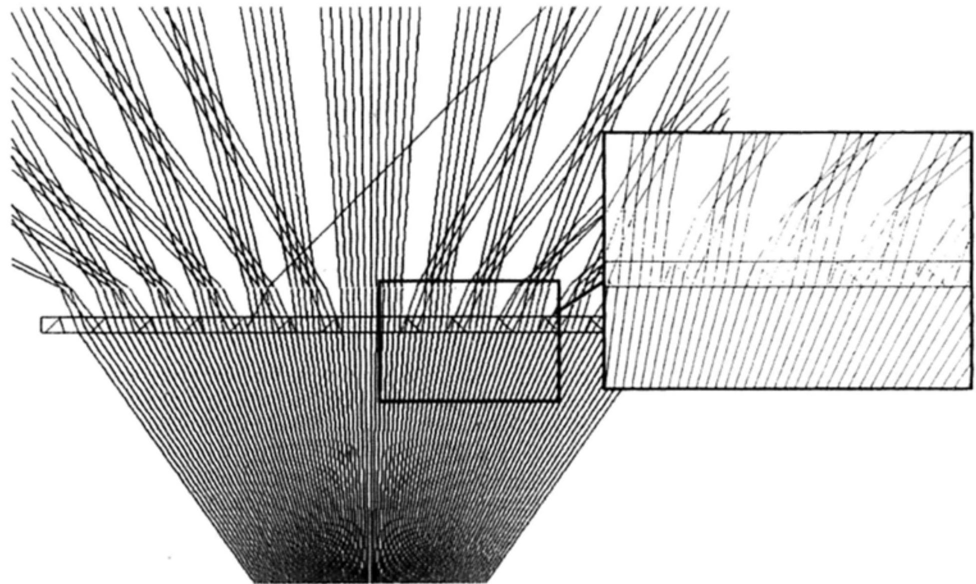

Fig. 8.4 Light rays diffracted by the gratings

As shown in Fig. 8.5 and Fig. 8.6, the incident light is being separated by the V-shaped grooves on the back side of the diffractive grating, and recombines to form a completely new pattern. Since diffractive grating is sensitive to a narrow range of

wavelength, it is ideal for laser applications. The gratings could spread light uniformly and extracting light precisely at each point across the panel. By defining the separation of diffracted light beams, optical properties of substrate material, and characteristics of the light source, the CAE simulation tool can optimize the depth and width of grooves according to the merit function and constraints. The constraints of the design are mostly defined by the properties of the AFM probe tip, such as the angle of the shape and the effective cutting area.

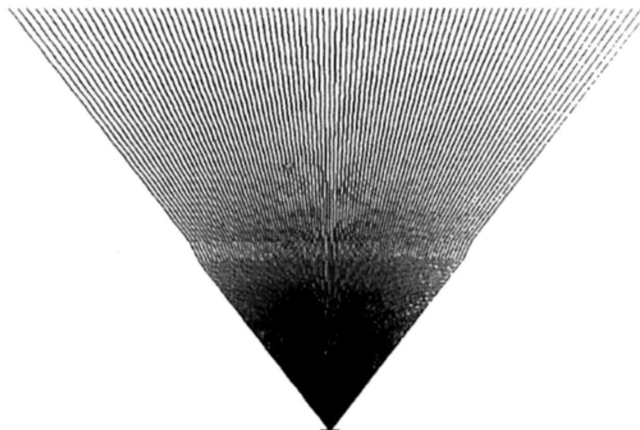

Fig. 8.5 Light propagation through optics without gratings

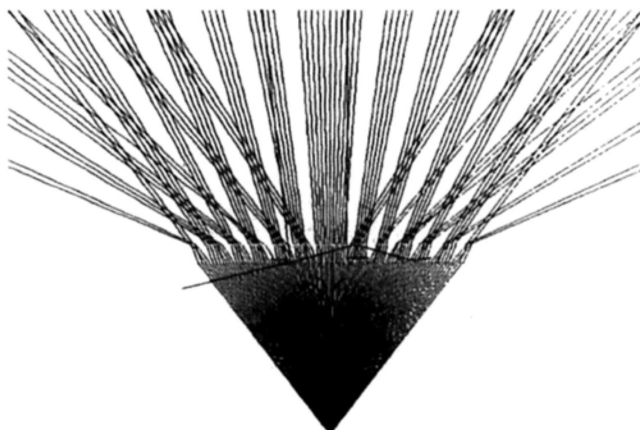

Fig. 8.6 Light propagation through optics with gratings

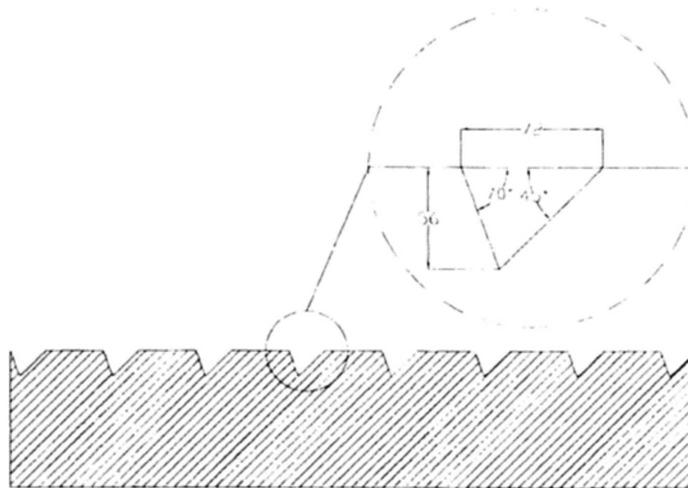

Fig. 8.7 Dimensions of V-shape grating

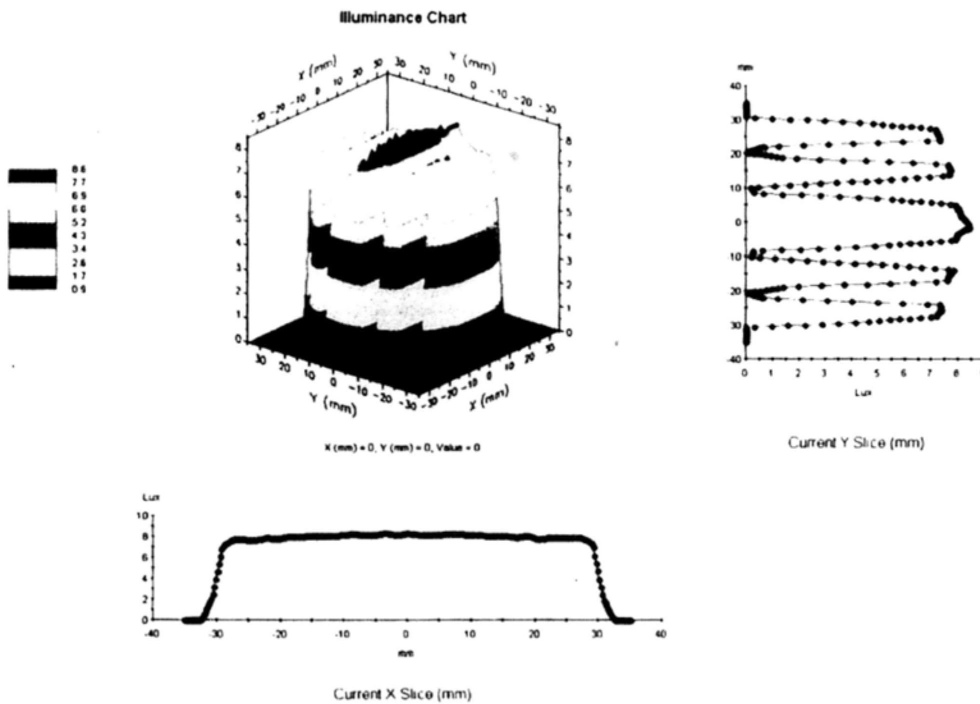


Fig. 8.8 Luminous intensity distribution

In this design, the optimal width and depth of grooves is $72\,nm$ and $56\,nm$, respectively (Fig. 8.7). By vary the pitch and depth of gratings, different beam patterns can be generated. Fig. 8.8 and Fig. 8.9 exemplified the simulation results of

the luminous intensity distribution when the incident beam is passing through the diffraction grating.

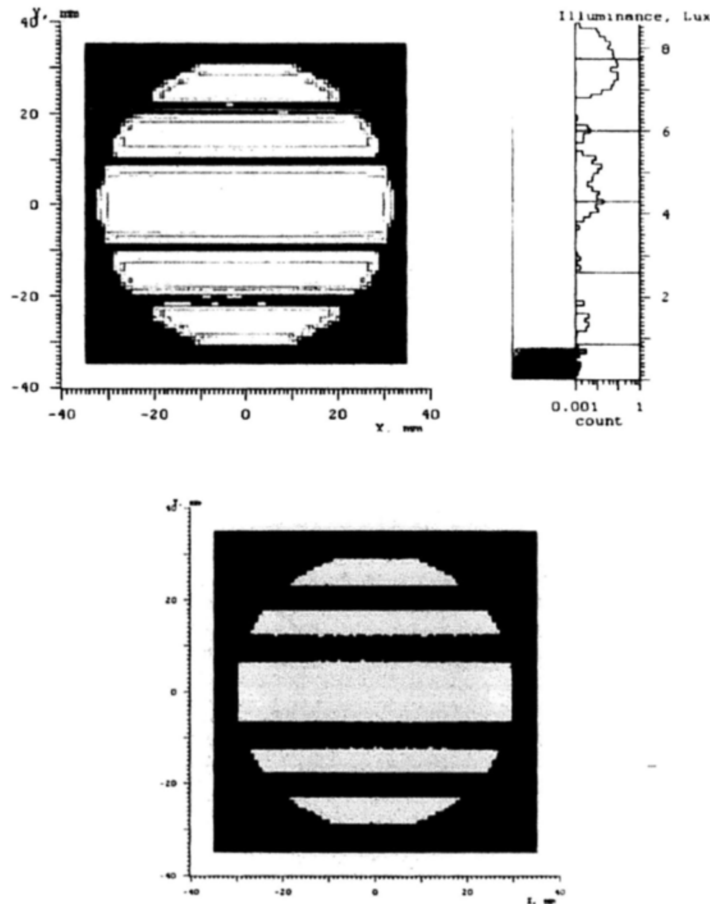


Fig. 8.9 Illuminous raster chart

For a DOE to achieve its theoretical resolution, the relative position and dimensions of each groove or microstructure must be maintained with extremely high precision. An advantage of using AFM for nanomanipulation over other instruments is that precise localization could be performed based on the high-resolution image obtained. Besides, the efficiency is also a primary performance criterion, it is effected by shape and size of microstructures, arrangement and fabrication accuracy. During the

lithography process, the depth and width of the grooves can be controlled by varying the applied force of the scanning probe.

For different kinds of optical surfaces, we have to apply different manufacturing process. For a plano surface, Single Point Diamond Turning (SPDT) would be most suitable. For the microstructures or V-shaped grooves, the developed integrated AFM nanomanipulation has been used. The indentation force and penetration depth were estimated by the force modeling as introduced in Section 4.

## 8.4 Plano Surface Machining by Single Point Diamond Turning

SPDT is an ultra-precision machining technique with a single point diamond cutting tool, which can achieve a high accuracy and repeatability (Fig. 8.10). The position accuracy is $\pm 1\, arc-\sec$ for the rotary axis and $\pm 2\, arc-\sec$ for the translation axis. The position feedback resolution is 0.016 $nm$. In order to maintain a transmission rate at a high level, both sides of the polymer substrate were finished by SPDT.

It is possible to ensure uniform surface roughness over the whole plano surface. The surface roughness can be determined by the spindle speed ($S$), feedrate ($F$), and the step size in different directions. The feedrate is a measure of wing radius ($R$), tool radius ($r$), and the cutting speed ($V$). The cutting speed is the removal rate of the substrate material by the cutting tool. With the desired surface roughness ($R_q$), the

feedrate can be calculated by

$$F = 2S\sqrt{\frac{5R_q rR}{r^2 + R^2}}. \tag{8.7}$$

where

$$S = \frac{1000V}{\pi D}. \tag{8.8}$$

where $D$ is the diameter of workpiece.

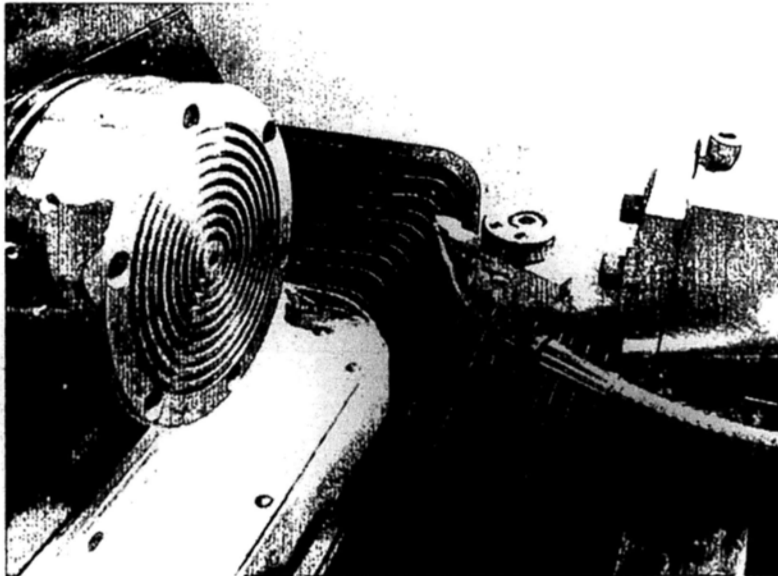

Fig. 8.10 Single Point Diamond Turning Machine

## 8.4 Results and Discussions

For the feasibility study of AFM nanomanipulation, a diffraction grating with an effective working area of an overall diameter of $5\,mm$ and thickness of $1.5\,mm$ had been fabricated. The PMMA substrate was machined by using the SPDT machine for obtaining the required surface finished. With a desired surface roughness of $0.015\,\mu m$, the machining parameters were determined by Eq. 8.7 and Eq. 8.8. For PMMA, the

cutting speed was $16.5\,m/\min$, the spindle speed was $5260\,rpm$. The swing radius and tip radius for the cutting tool was $2.527\,mm$ and $21.977\,mm$, respectively. Finally, the feedrate was calculated to be $14.825\,mm/\min$.

In order to evaluate the surface finish, the substrate was being measured under the Form Talysurf system after machining. Fig. 8.11 illustrated that the surface finished obtained is 0.0141 $\mu m$.

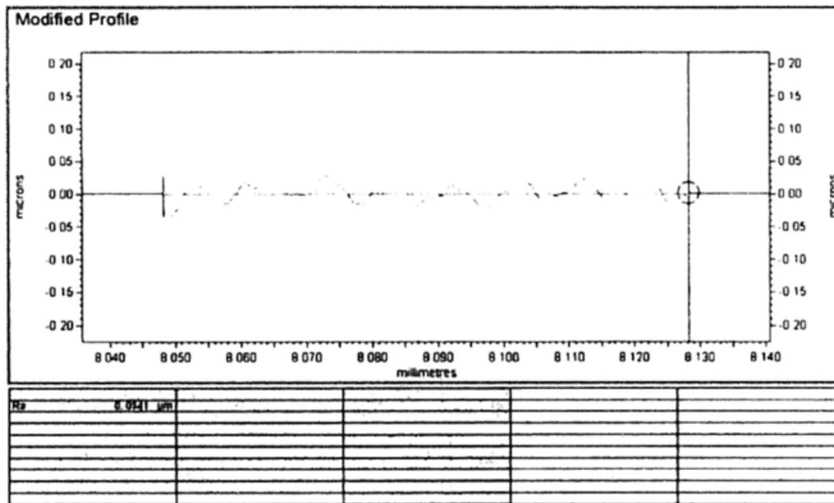


Fig. 8.11 Surface finish data obtained from Talysurf® measurement

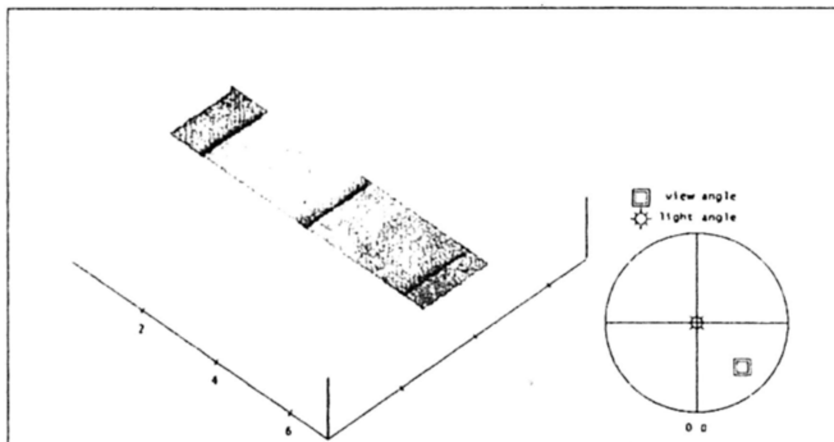


Fig. 8.12 Scanning data obtained from AFM

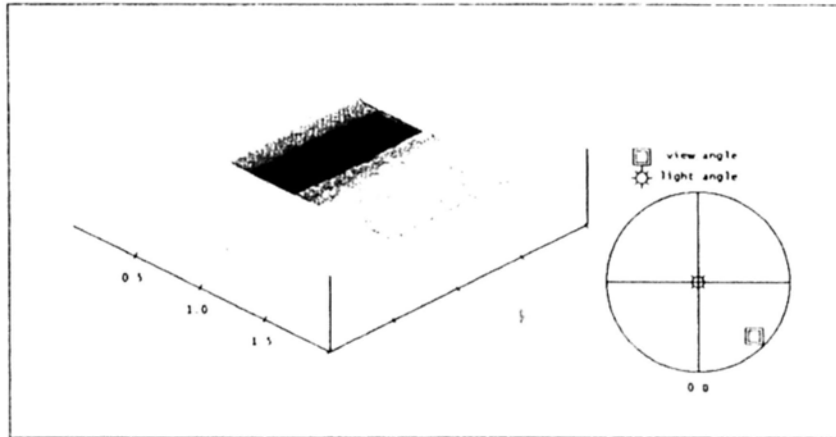

Fig. 8.13 Grating fabrication by AFM nanomanipulation

The grating pattern was fabricated on the PMMA substrate by nanomanipulation after the surface finishing process. The tip radius of the AFM probes was $100nm$ and the stiffness was 2.8 $N/m$. From the optimization results, the V-shaped pattern was having a depth of $56nm$, width of $72nm$, and pitch of $250nm$. The depth and width of grooves were controlled by the applied force of the AFM probe and the number of cycles for the lithography process. On the other hand, the pitch was precisely controlled by the piezoelectric actuators of the manipulation system, which guarantees for high precision in localization. Fig. 8.12 and Fig. 8.13 illustrated the gratings being fabrication on PMMA by the nanomanipulation technique.

In this experiment, each groove was fabricated by a 3-cycle operation. According to the contact mechanics model, the number of cycle was calculated along with the applied force. Fig. 8.14 characterized the 2D cross-section of a grating, where the average depth and width is $52.8nm$ and $68.5nm$, respectively. Compared to the

design parameters, there was a variance of 4 % - 6 %. It was mainly caused by the friction and adhesion during nanomanipulation.

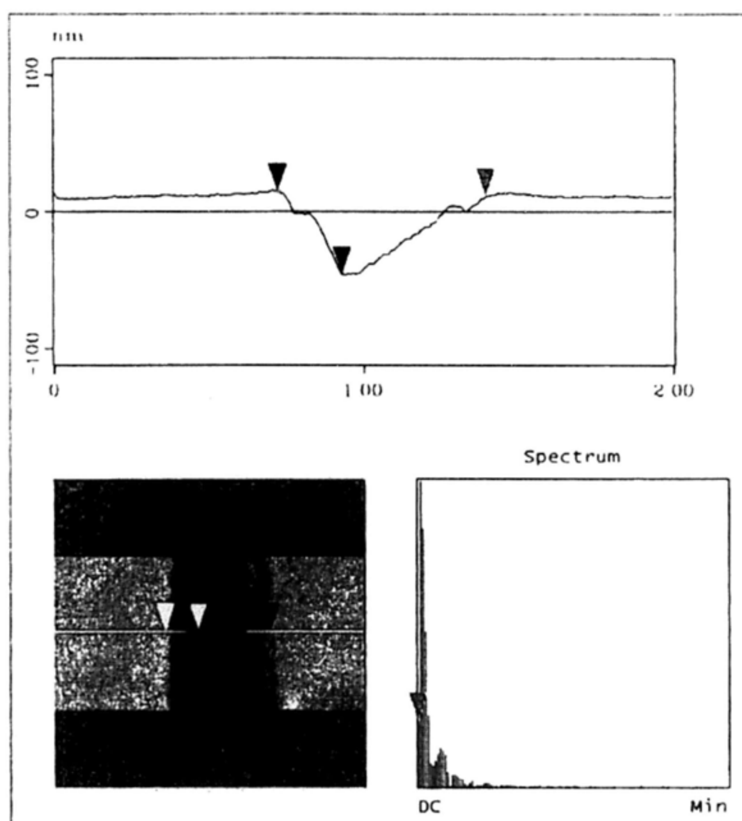


Fig. 8.14 2D cross-section analysis of a grating

The prototype device consisted of a laser source and the polymer diffractive element was being setup for design verification. The typical wavelength of the laser source utilized for this study was $635\,nm$. The spectral width was $1\,nm$ and the beam divergence was 40°. As shown in Fig. 8.15 and Fig. 8.16, good contrast interference fringes were attained after the laser beam passed through the diffraction grating. The absolute efficiency of a grating was obtained from comparing the intensity of the incident light and the diffracted light, finally it was measured to be 79 %.

Fig. 8.15 Laser spot without diffraction grating

Fig. 8.16 Beam shaping effect by the diffraction grating

# Chapter 9

# An Optical Lightguide for the Backlight Unit

## 9.1 Basics of a Backlight System

Display devices have been designed through an iterative process by trail and error, but this process is limited by the time and cost on making these prototypes. For a backlight module, uniform spatial luminance over a specified region is always required. With the aid of CAE techniques, virtual modeling tools can replace many of the physical prototypes. In addition, optimization tool provides the ability to explore a wider range of design options with improved performance.

The most common backlights are composed of a source coupled into the edge of a light guide where a spatially varying micro pattern couples flux out of the light guide to produce a spatially uniform luminance distribution. The micro pattern and the power within the light guide are balanced to provide the desired luminance distribution. Determining the micro pattern for a given backlight geometry is greatly facilitated through the use of optimization. Luminous intensity output is a primary performance criterion for the backlight unit. There are many factors affecting the efficiency of the system, including shape and size of microstructures, arrangement and fabrication accuracy.

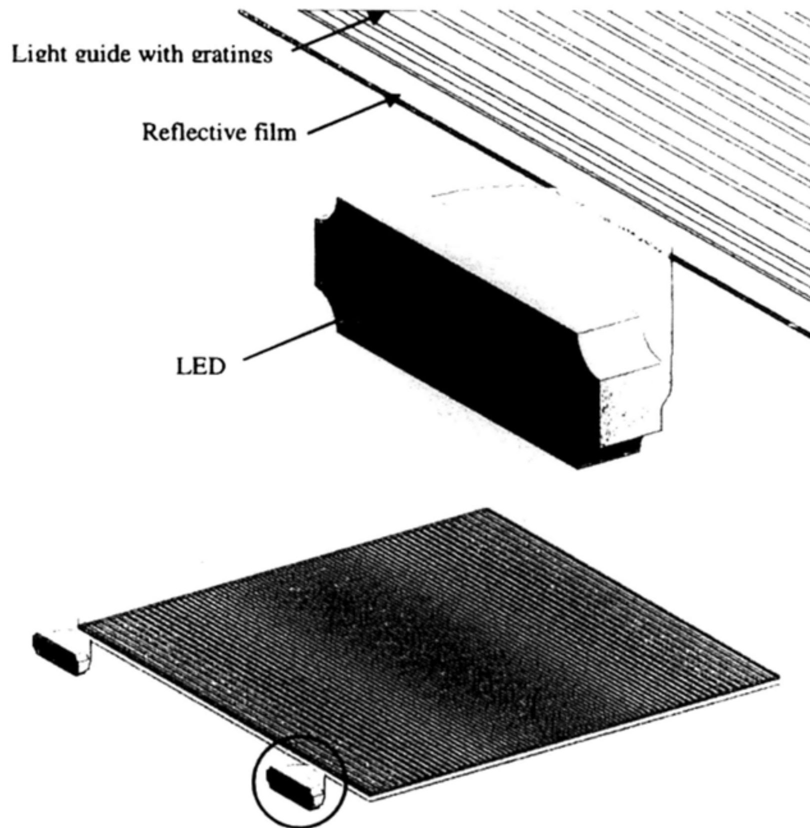


Fig. 9.1 LED backlight unit

In the backlight system, we have adopted the edge-lighting approach, which offered a thinner solution that could minimize the number of LEDs required as depicted in Fig. 9.1. The typical elements include a light guide with micro patterns and a reflective film. The sources used in the backlight system are LEDs with view angle of 120° and output power of 100 mcd. In addition, there was a reflective film placed underneath the light guide for redistribution of light and to maximize the out-coupled efficiency.

There are many different methods to spatially vary the extraction efficiency. The classic approach is to vary the density of the micro pattern. Many backlights

incorporate a 3D microstructure onto the light guide surface, and these structures can include many different shapes. Some common 3D microstructures are prisms, pyramids, and hemispheres. The extraction efficiency is achieved by varying the size or the placement of the 3D microstructures. Placement variations could also simplify the tooling required for fabrication.

## 9.2 Design Optimization

In the backlight system, the variables used are often quantities where there is a limited range for which they make physical sense. To minimize the time it takes for optimization, it is useful to use parameterizations that use some limited ranges. These parameterizations are also useful when setting up the initial system. For the density of scatter sites along the length of a light guide,

$$D(x) = D_S + (D_E - D_S)\left(\frac{x - x_S}{L}\right)^G . \quad (9.1)$$

where $D_S$ is the density at $x = x_S$, $D_E$ is the density at $x = L + x_S$, $L$ is the length of the light guide, and $G$ is a positive number that controls the curve shape. This function could be used to optimize a backlight where the microstructures are used to extract the light. The extraction efficiency is directly related to the pattern density. The start and end density are directly controlled, which is also necessary for adjusting the first order design. The density at the end is set to 1 to maximize the system efficiency. The start and end density are then being bounding and the density

varies between the two ends is controlled by a single variable. The merit function is defined as

$$\sum W_i^2 (V_i - T_i)^2 . \tag{9.2}$$

where $W_i$ is the weight of $i^{th}$ merit function item, $V_i$ is the current value of the $i^{th}$ merit function item, and $T_i$ is the target value for the $i^{th}$ merit function item. When Monte Carlo simulations are used, the results include errors that depend upon the number of traced rays. Tracing more rays reduces the statistical noise. The merit function items are the efficiency and relative luminance of the output at numerous points across the display.

The optimization algorithm will choose how to change the system to obtain a better solution. The algorithm used in this design is the Damped Least Squares (DLS). DLS increments each variable by a small amount, computes derivatives, and then computes a change vector using a damping factor. The change vector is then applied to the nominal variable values and the merit function is re-evaluated. The process will continue until a desired solution is obtained. Because derivatives are used, DLS converges quickly when the noise in the merit function is small. When Monte Carlo simulations are used to predict performance, it will add noise to the merit function. Noise tolerant optimization algorithms must consider this noise. The presence of noise has to be considered when comparing two systems to determine if a change to the

system has actually improved the system. The noise must also be considered when deciding whether the optimization is completed. When the noise in the merit function is large, there is a risk that the optimization algorithm may be compensating for errors due to statistical noise, rather than errors due to a noiseless $V_i - T_i$.

Most backlights is a 1:1 spatial correlation between the extraction pattern position and the spatial luminance distribution. Increasing the extraction efficiency in a given region of the light guide can alter the distribution over the whole display area, but there tends to be a direct correlation for the luminance directly above the extraction pattern. This special correspondence can enhance the converging speed of the optimization algorithm. The mesh feedback optimization uses an iterative approach based upon changing the extraction pattern using the simulated output distribution. The exact relationship between extraction efficiency and luminance does not need to be known, only the spatial correspondence between the spatial luminance distribution and the extraction pattern. The iterative relationship is described as

$$T_i(x, y) = K_{i-1} \times T_{i-1}(x, y) \times \left[ \frac{L_t(x, y)}{L_{i-1}(x, y)} \right]^{\alpha} . \tag{9.3}$$

where $T_i(x, y)$ is the pattern at the $i^{th}$ iteration, $K_i$ is a scale factor, $L_i(x, y)$ is the spatial luminance distribution at the $i^{th}$ iteration, $L_t(x, y)$ is the target luminance distribution and $\alpha$ is a damping factor.

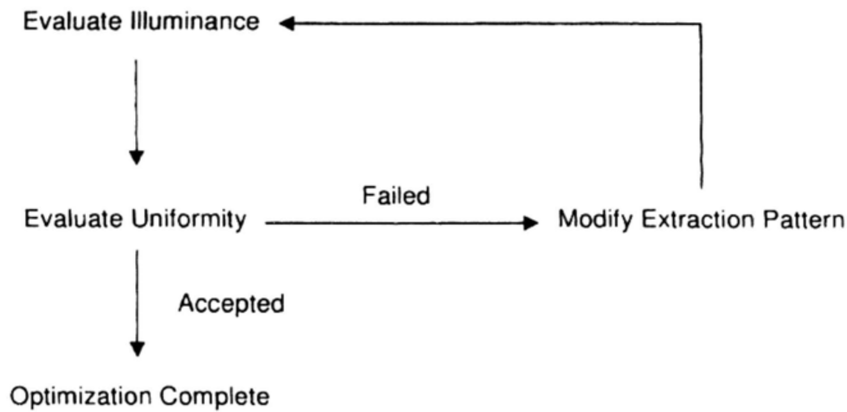


Fig. 9.2 Mesh feedback optimization

The current extraction pattern and its resulting output distribution are used to compute a new extraction pattern. The output distribution can be characterized in many ways. The illuminance and spatial luminance are common characteristics. This feedback approach simply relies on a mesh of data point that has a 1:1 correlation with positions of extraction patterns. The iterative nature of the mesh feedback optimization is depicted in Fig. 9.2.

The iterative approach works robustly even if the starting extraction pattern produces an extremely non-uniform luminance distribution Since the extraction efficiency is what concerns, it applies to density, size, and spacing changes. In this design, there are 2 LEDs placed along the left edge of the display. The spacing, pitch and height of the extraction pattern are varied to adjust the extraction efficiency.

At the backside surface of the light guide, there was a plurality of V-shaped gratings as the extraction pattern, where the emission surface was a plano surface. The gratings

were parallel to each other and with varying pitch and height. Light beams emitted from the light sources entered the light guide through the incident surface in different directions. Thus, some light beams reaching the gratings were incident at the interface at angles greater than a critical angle, and were reflected and then emitted from the light emission surface. Other light beams reaching the gratings at angles less than the critical angle were refracted and emitted from the backside surface, and were then reflected by the reflective film back into the light guide as illustrated in Fig. 9.3.

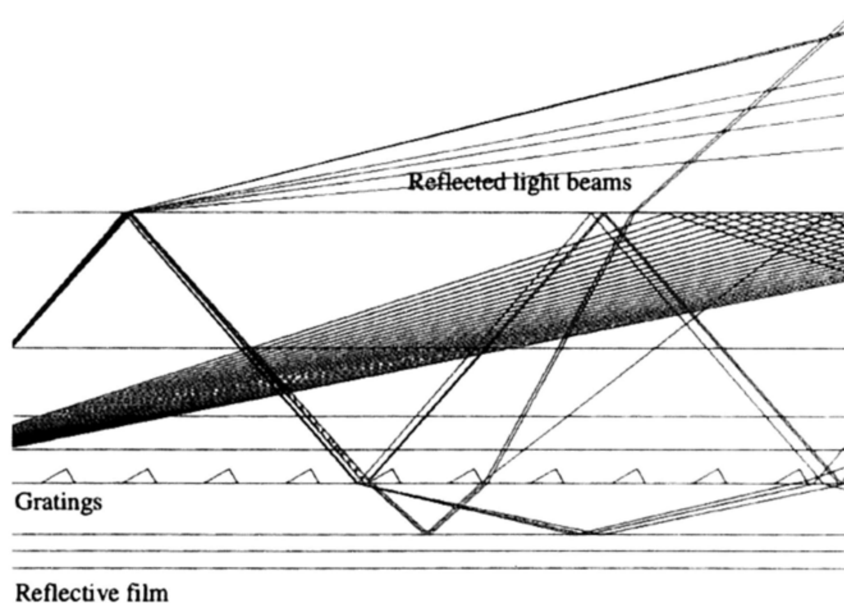


Fig. 9.3 Light scattering pattern

The micro-grating light guide could spread light uniformly and extracting light precisely at each point across the panel. It controlled incident light rays by redirecting their emission angles from the light guide while minimizing scattering. By varying the pitch and depth of gratings, uniformity was improved. Away from the light source,

there should be an increasing pitch and depth in order to extract more light at that region. Fig. 9.4 exemplified the luminous intensity distribution at the emitting surface of a light guide.

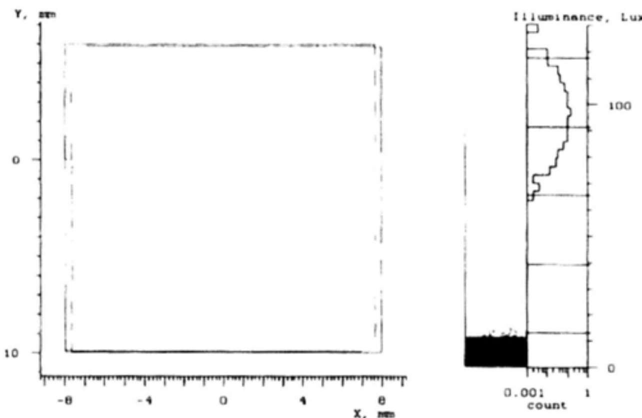


Fig. 9.4 Luminance distribution after optimizatin

## 9.3 Results and Discussions

For the feasibility study of AFM nanomanipulation, a light guide of $10mm \times 10mm \times 1mm$ has been fabricated. The pattern used was V-shaped gratings with depth of $15nm$ $-25nm$, pitch of $150nm$ $-250nm$. The nanomanipulation technique was applied to gratings fabrication on PMMA as shown in Fig. 9.5.

In order to evaluate the surface finish and form accuracy of the light guide, it was being measured under the Form Talysurf system after machining. As shown in Fig. 9.6, the pitch was in the range of $150nm$ to $250nm$, which is precisely controlled by the piezoelectric actuator of the AFM system. The AFM based nanomanipulation guarantees for precision in localization. Fig. 9.7 illustrated that the surface finished

obtained is $0.01\mu m$.

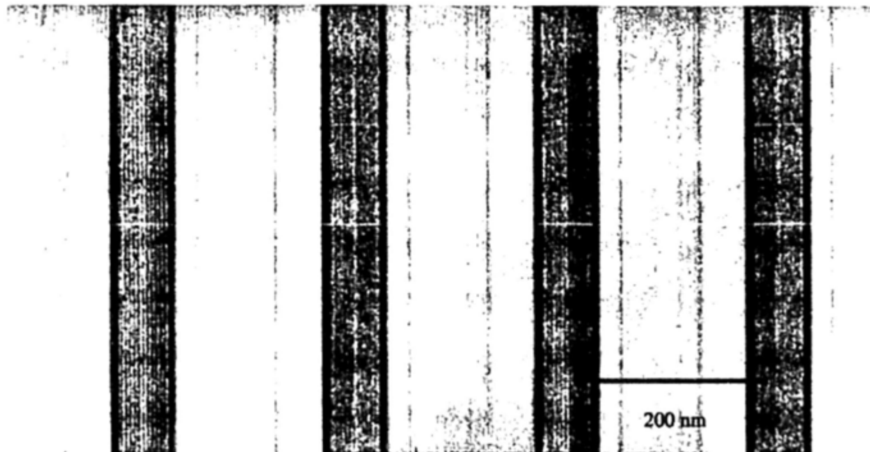


Fig. 9.5 V-grooves fabricated by AFM nanomanipulation

For the depth and width of gratings, they were controlled by the applied force of the AFM probe and the number of scratches. Fig. 9.8 characterized the 2D cross-section of a grating, where the width and depth is $150nm$ and $25nm$, respectively. The depth of the grating varied with the number of cycles of scratch.

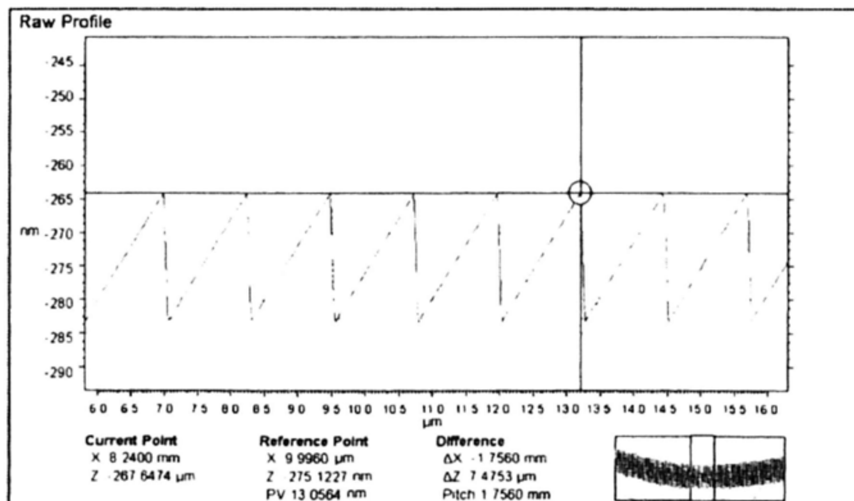


Fig. 9.6 Topography data obtained from Talysurf® measurementt

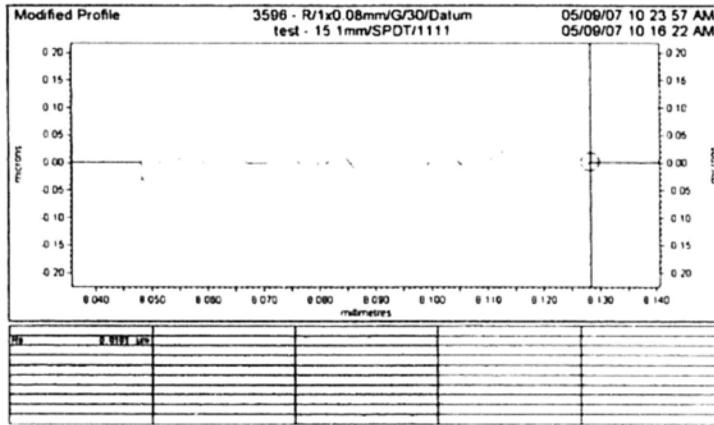


Fig. 9.7 Surface finish data obtained from Talysurf® measurement

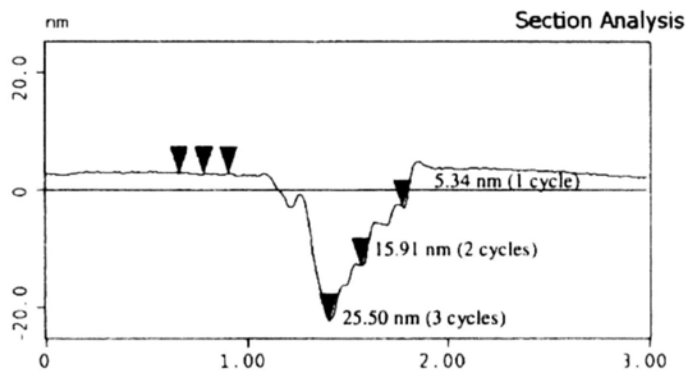


Fig. 9.8 Cross-seciton analysis of a light guide

As shown in Fig. 9.9, the luminance micro-uniformity for the designed light guide with the grating patterns was being improved. The enhanced uniformity enabled fully utilization of the active area of the light guide.

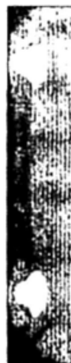

Fig. 9.9 Functional protoype with LEDs and light guide

# Chapter 10

# Conclusion

## 10.1 Summary of Research Work

In this project, design and realization of an AFM based nanomanipulation system for efficient and reliable fabrication of microscale structures was presented. This project had been a preliminary attempt at generating nano/microscale structures using AFM nanofabrication techniques. Based on this experience, it was apparent what improvements should be made to both the fabrication process and the design to further satisfy the requirements of miniaturized components.

At the initial stage of this project, study of prior art provided us the basic concept of nanomanipulation. For the Atomic Force Microscope, it could be utilized for both scanning and manipulation. Throughout the experience obtained from different experiments, it was found that selection of appropriate probe tip and scanning mode was crucial as it helped in eliminating artifacts of the scanned image. Probe selection was also important for the performance and force estimation of the nanomanipulation. In order to increase the utility and versatility of the nanomanipulation system, it was highly desirable if the position and force of the probe tip was measurable. These capabilities would allow more refined manipulation and used for mechanical testing of micro / nano objects.

The integrated nanomanipulation was equipped with an optical control system so as to automate the target searching process, which made the manipulation process became more effective. With the aid of haptic feedback, the user could feel the force applied to the nano structure. The manipulation and navigation processes then became more flexible and realistic. Besides, the manipulation process could be programmable and a sequence of motions could be made. Besides, by analyzing the characteristics of different force mechanics models, force estimation became more accurate. Based on the properties of the probe tips and sample surfaces, an appropriate force model could be selected accordingly.

Although the AFM manipulation techniques had been developed for some time, the applications were mainly focused on a few areas. In this research, it was found that the manipulation techniques could be further developed in the photonics application. The characteristics of the AFM probe tip was an advantage for the optics design, such as the beam shaping optical element and the lightguide for backlight unit demonstrated. With the defined geometry of the AFM probe tip, the optical design could be generate through optimization. Indeed, prototyping is always important for validation of an optical design, but the fabrication process is time-consuming and expensive. There are several methods in microfabrication but the process parameters are difficult to control precisely. Variations in process can cause variations in device

characteristics and consequent variation in device performance. For example, variations in the isotropy of etching, exposure time during photolithography, or spin rate during development can all results in dimensional variations of the microstrucutres. For an optical design, such dimensional variations will definitely change the photometric performance of the device. AFM nanomanipulation was proven to be an effective and cost-effective way for prototype fabrication. It eliminated the need for tooling fabrication and the process could be accurately controlled by the applied force of the AFM cantilever and motion of the piezoelectric actuators.

## 10.2 Future Work and Considerations

Since nanomanipulation is an emerging technology with identifiable scientific value, it is expected that the application of nanofabrication to the optics field would be a commendable contribution. It would improve the efficiency of design and prototyping process, also to enable a more rapid progress relating to new development. An issue to be addressed for the applications is the nanofabrication of lightguide with micro-pyramid pattern. Since most of the AFM tip is of is having a probe tip of pyramid shape, it is possible to generate the design in a highly-effective way.

Fig. 10.1 demonstrates a lightguide with pyramids pattern of different separation and depth. The depth of the microstructure can be accurately controlled by the applied

force of the AFM tip. With the precise localization feature, AFM nanoindentation can be used for patterning accurately. The microstructure pattern is designed for improving the uniformity as light from one end could be propagated to another side of the light guide. Fig. 10.2 and 10.3 demonstrate a light guide without microstructure and a light guide with microstructure. It is obvious that the uniformity could be highly improved. Taking into consideration of the AFM tip shape, the design can be optimized with two variables, which are the separation and depth of the micro-pyramid.

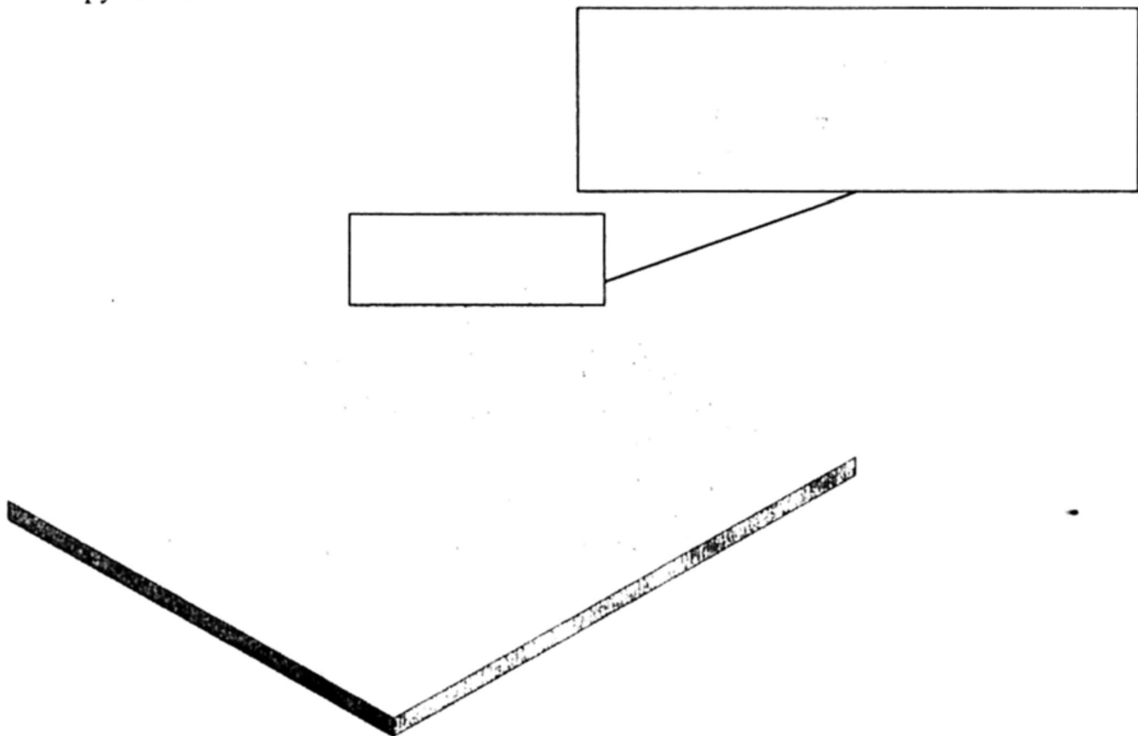

Fig. 10.1 Lightguide with micro-pyramid structures

For a lightguide, material with higher transmission rate would be more desirable. Polymer such as acrylic and polycarbonate are commonly used. From the experiment

results, it was found that AFM tip with diamond coating can be used for nanofabrication on polymer surfaces.

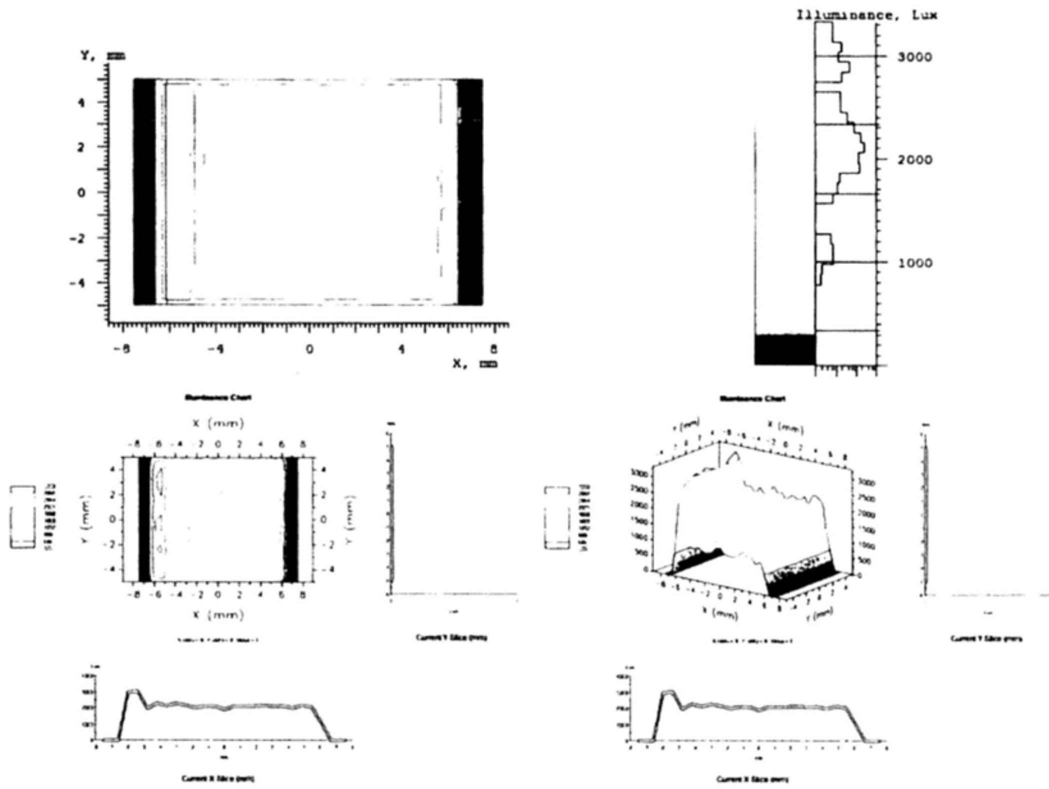


Fig. 10.2 Light distribution for lightguide without microstructures

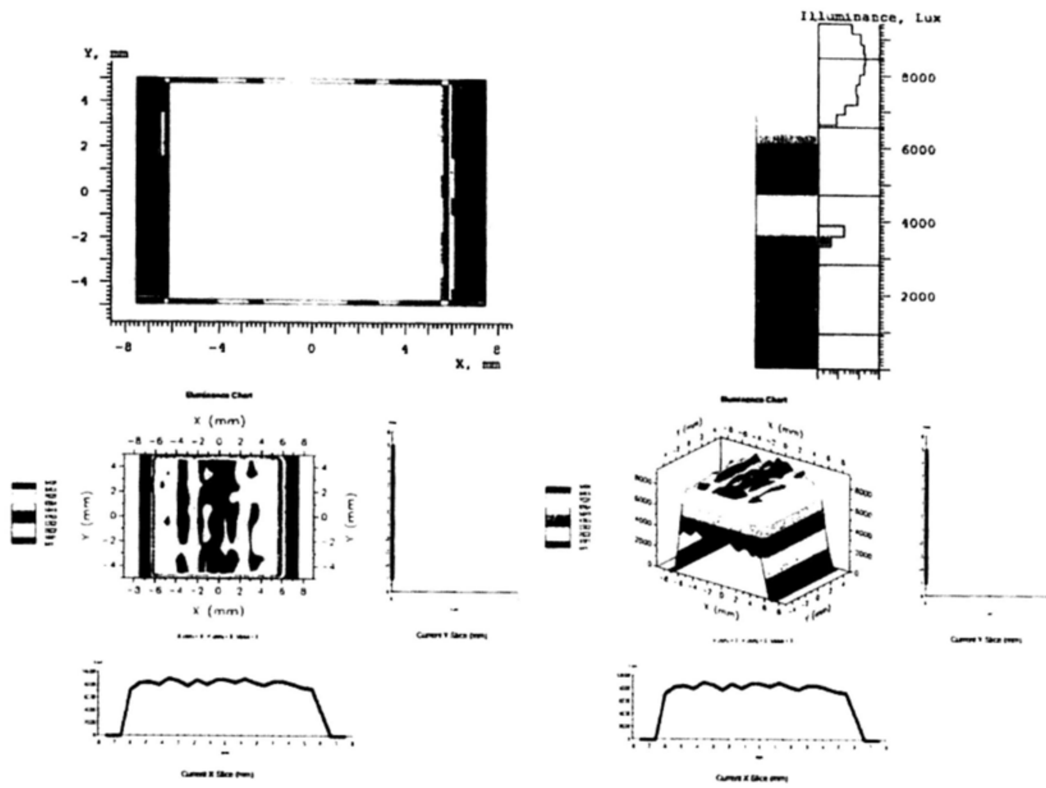


Fig. 10.3 Light distribution for lightguide with microstructures

# References

[1] G. Binnig, H. Rohrer, Ch. Gerber and E. Weibel, "Surface studies by scanning tunneling microscopy," *Physical Review Letters*, vol. 49, no. 1, pp. 57 – 61, 1982.

[2] J. A. Stroscio and D. M. Eigler, "Atomic and molecular manipulation with the scanning tunneling microscope," *Science*, vol. 254, pp. 1319-1326, 1991.

[3] I. W. Lyo and P. Avouris, "Field-induced nanometer0scale to atomic scale manipulation of silicon surfaces with the STM," *Science*, vol. 253, pp. 173-176, 1991.

[4] J. Mou, D. M. Czajkowsky, S. J. Sheng, R. Ho, and Z. Shao, "High resolution surface structure of E. coli GroeS Oligomer by Atomic Force Microscopy," *FEBS Letters*, vol. 381, pp.161 – 164, 1996.

[5] Y. E. Strausser, M. Schroth, and J. J. Sweeney, "Characterization of the low-pressure chemical vapor deposition grown rugged polysilicon surface using atomic force microscopy," *J. Vas. Sci. Technol. A*, vol. 15, pp. 1007, 1997.

[6] T. Junno, K. Deppert, L. Montelius, and L. Samuelson, "Controlled manipulations of nanoparticles with an atomic force microscope," *Appl. Phys. Lett.*, vol. 66, pp. 3627-3629, 1995.

[7] D. M. Schaefer, R. Reifenverger, A. Patil, and R. Pl Andres, "Fabrication of two-dimensional arrays of nanometer-size clusters with the atomic force microscope," *Appl. Phys. Lett.*, vol. 66, pp. 1012-1014, 1995.

[8] A. A. G. Requicha, C. Baur, A. Bugacov, B. C. Gazen, B. Koel, A. Madhukar, T. R. Ramachandran, R. Resch, and P. Will, "Nanorobotic assembly of two-dimensional structures," in *Proc. IEEE Int. Conf. Robotics and Automation*, Leuven, Belgiumj, 1998, pp. 3368-3374.

[9] L. T. Hansen, A. Kuhle, A. H. Sorensen, J. Bohr, and P. E. Lindelof, "A technique for positioning nanoparticles using an atomic force microscope," *Nanotechnol.*, vol.9, pp. 337-342, 1998.

[10] P. E. Sheehan and C. M. Lieber, "Nanotribology and nanofabrication of $MoO_3$ structures by atomic force microscopy," *Science*, vol. 272, pp. 1158-1161, 1996.

[11] G. Binnig, C. F. Quate, C. Gerber, *Phys. Rev. Lett.*, vol. 56, pp. 930 – 933, 1986.

[12] B. Bhushan, *Handbook of Micro/Nanotribology*, Second edition, CRC Press, Boca Raton, Florida, 1999.

[13] J. Israelachvili, *Intermolecular & Surface Forces*, Academic Press Inc., San Diego, 1991.

[14] D. Bonnell, *Scanning Probe Microscopy and Spectroscopy: Theory, Techniques and Applications*, John Wiley & Sons Inc., New York, 2001.

[15] NA Burnham and AJ K., *Surface Forces and Adhesion*, CRC Press, Boca Raton, 1997.

[16] C.F. Quate, "The AFM as a tool for surface imaging," *Surf. Sci.*, vol. 980, pp. 299 – 300, 1994.

[17] S. Iijima, "Helical microtubules of graphitic carbon," *Nature*, vol. 354, pp. 56, 1991.

[18] P. J. F. Harris, "Carbon nanotubes and related structures: new materials for the twenty-first century," *Cambridge University Press*, Cambridge, 1999.

[19] D. Srivastava, M. Menon, and K. Cho, "Computational nanotechnology with carbon nanotubes and fullerenes," *Computing in Science and Engineering*, vol. 2, pp. 42, 2001.

[20] D. H. Robertson, D. W. Brenner, and J. W. Mintmire, "Energetics of nanoscale graphitic tubules," *Phys. Rev. B*, vol. 45, pp. 12592 – 12595, 1992.
[21] S. Sawada, N. Hamada, "Energetics of carbon nano-tubes," *Solid State Commun.*, vol. 83, pp. 678 – 680, 1996.
[22] M. R. Falvo, G. Clary, A. Helser, S. Paulson, R. M. Taylor II, V. Chi, F. P. Brooks, Jr. S. Washburn, and R. Superfine, "Nanomanipulation experiments exploring frictional and mechanical properties of carbon nanotubes," *Microscopy and Microanalysis*, vol. 4, pp. 504 – 512, 1999.
[23] A. Rochefort, Ph. Avouris, F. Lesage and D. R. Salahub, "Electrical and mechanical properties of distorted carbon nanotubes," *Phys. Rev. B*, vol. 60, no. 18, pp. 13824 – 13850, 1999.
[24] B. I. Yakobson and P. Avouris, "Mechanical properties of carbon nanotubes," *Appl. Phys.*, vol. 80, pp. 287 – 327, 2001.
[25] E. T. Thostenson, W. Z. Li, D. Z. Wang, Z. F. Ren, and T. W. Chou, "Carbon nanotubes / carbon fiber hybrid multi-scale composites," *J. of Appl. Phys.*, vol. 91, pp. 6034 – 6037, 2002.
[26] D. Hull, *An introduction to composite materials*, 2nd ed. Cambridge University Press, Cambridge, 1996.
[27] C. Bower, R. Rosen, L. Jin, J. Han and O. Zhou, "Deformation of carbon nanotubes in nanotubes-polymer composites," *Appl. Phys. Lett.*, vol. 74, no. 22, pp. 3317 – 3319, 1999.
[28] M. Cdek, B. Le Foulgoc, J. N. Coleman, V. Barron, and W. J. Blau, "Mechanical and thermal properties of multiwalled carbon nanotubes reinforced polymer composities," *Conf. Proc. of Compositie Eng.*, San Diego/CA, USA, 2002.
[29] L .H. Peebles, *Carbon fibers: formation, structure, and properties*, CRC Press, Boca Raton, 1995.
[30] Q. Ma, and D. R. Clarke, "Size dependence of the hardness of silver single crystals," *J. of Material Research*, vol. 10, pp. 853 – 863, 1995.
[31] G. M. Pharr, W. C. Oliver, and F. R. Brotzen, "On the generality of the relationship among contact stiffness, contact area, and elastic modulus during indentation," *J. of Material Research*, vol. 7, pp. 613 – 617, 1992.
[32] G. M. Pharr, "Measurement of mechanical properties by ultra-low load indentation," *Materials Science and Engineering A*, vol. 253, pp. 159, 1998.
[33] N. A. Burnham, S. P. Baker, H. M. Pollock, "Model for mechanical properties nanoprobes," *J. of Materials Research*, vol. 15, no. 9, pp. 2006 – 2014, 2000.
[34] T. W. Tombler, C. Zhou, L. Alexseyev, J. Kong, H. Dai, L. Liu, C. S. Jayanthi, M. Tang, and S. Y. Wu, "Reversible electromechanical characteristics of carbon nanotubes under local-probe manipulation," *Nature*, vol. 405, pp. 769 – 772, 2000.
[35] Victor T. S. Wong, and Wen J. Li, "Bulk carbon nanotubes as sensing element for temperature and anemometry micro sensing," *IEEE MEMS 2003*, pp. 41 – 44, 2003.
[36] I. Yoshitada, N. Takahiro, and T. Takeshi, "AFM bending test of nanometric single crystal silicon wire at intermediate temperature for MEMS," *IEEE Int. Conf. on Micro Electro Mech. Sys.*, pp. 135 – 138, 2001.
[37] S. Roth, L. Dellmann, G. A. Racine, and N. F. de Rooij, "High aspect ratio UV photolithography for electroplated structures," *J. Micromech. Mecroeng.*, vol. 9, pp. 105 – 108, 1999.
[38] E. Kim, G. M. Whitesides, M. B. Freiler, M. Levy, J. L. Lin, and R. M. Osgood Jr., "Fabrication of micrometer-scale structures on GaAs and GaAs/AlGaAs

quantum well material using microcontact printing," *Nanotechnology*, vol. 7, pp. 266 – 269, 1996.

[39] H. Ohji, P. T. J. Gennissen, P. J. French, and K. Tsutsumi, "Fabrication of a beam-mass structure using single-step electrochemical etching for micro structures (SEEMS)," *J. Micromech. Microeng.*, vol. 10, pp. 440 – 444, 2000.

[40] R. A. Said, "Microfabrication by localized electrochemical deposition: experimental investigation and theoretical modeling," *Nanotechnology*, vol. 15, pp. 867, 2004.

[41] H. Iwasaki, T. Yoshinobu, and K. Sudoh, "Nanolithography on $SiO_2/Si$ with a scanning tunneling microscope," *Nanotechnology*, vol. 14, pp. 55 - 62, 2003.

[42] C. K. Hyon, S. C. Choi, S. H. Song, S. W. Hwang, M. H. Son, D. Ahn, Y. J. Park, and E. K. Kim, "Application of atomic-force-microscope direct patterning to selective positioning of InAs quantum dots on GaAs," *Applied Physics Letters*, vol. 77, pp. 2607 – 2609, 2000.

[43] M. Falvo, R. Superfine, S. Washburn, M. Finch, R. M. Taylor, V. L. Chi, and F. P. Brooks Jr.., "The nanomanipulator: A teleoperator for manipulating materials at the nanomerter scale," *Proc. of Int. Symp. On Science and Technology of Atomically Engineered Materials*, pp. 579 – 586, 1996.

[44] P. L. Huyskens, W. A. P. Luck, and T. Z. Huyskens, *Intermolecular Force, An Introduction to Modern Methods and Results*, Spring-Verlag, Berlin, Heidelbery, 1991.

[45] J. Israelachvili, *Intermolecular and Surface Force*, Academic Press, 2$^{nd}$ edition, 1991.

[46] W. Veldkamp and T. J. Mchugh, *Binary Optics*, Scientific American, New York, 1992.

[47] H. I. Smith, "A proposal for maskless, zone-plate-array nanolithography," *J. Vac. Sci. Technol.*, B 14, pp. 4318 – 4322, 1996.

[48] R. Kashyap, *Fiber Bragg grating*, Academic Press, London, 1999.

[49] G. Nordin, J. T. Meier, P. C. Deguzman, and M. Jones, "Diffractive optical element for Stokes vector measurement with a focal plane array," in *Polarization: Measurement, Analysis, and Remote Sensing II*, SPIE 3754, pp. 169 – 177, 1999.

[50] M. R. Sharpe and D. Irish, "Stray light in diffraction grating monochromators," *Opt. Acta*, vol. 25, pp. 861 – 893, 1978.

# List of Publications

Journal Papers

[1] L. M. Fok, Y. H. Liu, and W. J. Li, Prototyping of Diffrative Grating Optics for Sensor Application by an Integrated Probe-based System, to appear in *International Journal of Information Acquistion.*

[2] L. M. Fok, Y. H. Liu, and W. J. Li, Prototyping of Beam Shaping Diffraction Gratings by AFM Nanoscale Patterning, to appear in *IEEE Transactions on Automation Science and Engineering.*

[3]

Conference Papers

[1] L. M. Fok, Carmen K. M. Fung, Y. H. Liu and Wen J. Li, "Nano-mechanical Test of CNT-Embedded MEMS Structures by AFM," *International Conference on Nanoscale Devices and System Integration*, February 15, 2004

[2] L. M. Fok, Y. H. Liu, Carmen K. M. Fung and Wen J. Li, "Nano-scale Mechanical Test of MEMS Structures by Atomic Force Microscope," *IEEE 5th World Congress on Intelligent Control and Automation*, June 15, 2004.

[3] L. M. Fok, Y. H. Liu, and W. J. Li, Modeling of haptic sensing of nanomanipulation with an atomic force microscopy, *Proc. of International Conference on Robotics and Automation*, pp. 2457-2462, 2005.

[4] L. M Fok, Y. H. Liu and Wen J. Li, "Modeling of Nanomanipulation with an Integrated Teleoperated System," *IEEE International Conference on Robotics and Biomimetics*, June 29, 2005.

[5] L. M Fok, Y. H. Liu and Wen J. Li, "Fabrication and Characterization of nanowires by Atomic Force Microscope Lithography," *IEEE/RSJ International Conference on Intelligent Robots and Systems, October 9*, 2006.

[6] L. M Fok, Y. H. Liu and Wen J. Li, "Assembly of Nano Optics by an Integrated August 2, 2007.